

# **Towards artificial skin: micromachined capacitive force sensors and flexible polymeric substrates**

THÈSE N° 5595 (2013)

PRÉSENTÉE LE 4 MARS 2013

À LA FACULTÉ DES SCIENCES ET TECHNIQUES DE L'INGÉNIEUR

LABORATOIRE DE MICROSYSTÈMES 2

PROGRAMME DOCTORAL EN MICROSYSTÈMES ET MICROÉLECTRONIQUE

ÉCOLE POLYTECHNIQUE FÉDÉRALE DE LAUSANNE

POUR L'OBTENTION DU GRADE DE DOCTEUR ÈS SCIENCES

PAR

**Jagoda Anna DOBRZYNSKA**

acceptée sur proposition du jury:

Prof. A. Kis, président du jury

Prof. M. Gijs, directeur de thèse

Prof. S. Lacour, rapporteur

Prof. Ph. Passeraub, rapporteur

Prof. O. Paul, rapporteur



ÉCOLE POLYTECHNIQUE  
FÉDÉRALE DE LAUSANNE

Suisse  
2013



# Acknowledgements

It is my great pleasure to express my gratitude to the people who have contributed to this thesis with their advice, encouragement and cooperation.

I am deeply thankful to Professor Martin Gijs, for hiring me in his laboratory as a student, and for the guidance, he supported me with throughout these years, towards a doctorate degree. Professor Gijs provided me with a great opportunity to work in a microtechnology project, although my background came from a macro-engineering science, and, when starting the studies, microfabrication processes were completely new topics for me. Nevertheless, he has always trusted in my abilities, and, there were even moments, when he had more faith in my skills, than I did myself! He entrusted me with a funding-supported freedom, to explore my ideas, to direct and to lead the course of this doctorate in the fascinating world of a clean room. It was a great honour and pleasure working with you, and I am also grateful for the support you have shown me in my family life.

I wish to express my gratitude to the jury members: Professor Stéphanie Lacour, Professor Philippe Passeraub and Professor Oliver Paul, who have honored me by accepting to review this thesis. Thank you, for taking the time and effort to evaluate my work, and for your constructive feedback. I am grateful to Professor Andras Kis for having accepted to be the president of the jury.

I would like to acknowledge the financial support of the Swiss National Science Foundation (project 32003B-12042) which has founded the first three years of my doctorate. I also thank my collaborators, Professor Kamiar Aminian, Dr Hossein Rouhani and Dr Xavier Crevoiser, for useful suggestions and discussions regarding the sensor's design and application. Thank you, Pierre Joris, Professor Philippe Renaud, and Dr Sébastien Jiguet, for your collaboration which resulted in the successful development of polyimide microfoams. Pierre, you have always been my second pair of eyes, second pair of hands, and a second brain in the clean room, full of ideas, enthusiasm, and beliefs in success.

I express my thanks to the whole staff of the EPFL Center of MicroNanoTechnology CMI, for your precious help in the elaboration of the microfabrication process, useful

## Acknowledgements

---

discussions, for your confidence with the expensive and easy-to-break equipment, and for the freedom you gave me. In particular, special thanks to Dr Cyrille Hibert, Guy-François Clerc, Dr George-André Racine, Dr Philippe Langlet, Dr Jean-Baptiste Bureau and Boris Lunardi.

This research would not have been possible without EPFL Interdisciplinary Centre for Electron Microscopy CIME: Colette Vallotton and Daniele Laub, who helped me with SEM sample preparation methods, and Dr Vincent Laporte who did the XPS analysis. Many thanks to Dr Csilla Miko from the EPFL Mechanical Metallurgy Laboratory for your kindness and supply with the microcompressor setup, and to my student, Michael Dommer, for running the tests on the machine. I thank Dr Ayat Karimi for nanoindentation measurements and useful discussions. I acknowledge Peter Ferraro and Empower Materials for their feedback, and Dr Oscar Vazquez-Mena for the preparation of the nanostencil. It was a pleasure to discuss with Dr Nathan Fritz from Georgia Institute of Technology, and Dr Stefan Metz, receiving their useful comments and suggestions. Special thanks to Dr Bryan Schubert from EPFL Laboratory of Intelligent Systems for the development of the microstage-force measurement setup.

I am sincerely indebted to Dr Farnaz Moser and EPFL Equal Opportunities Office. Their kindness and financial support for the daycare of my daughter, has allowed me to finish these studies and progress further in my career, being a mother at the same time.

Thanks, Josias, for reading thoroughly my thesis and for all the corrections that have greatly contributed to the improvement of the manuscript. Also, thank you for translating my abstract into German. Thank you, Rima and Pierre, for the Italian and French translations of my abstract. Jules, thanks for the improvement of my introduction. I am very thankful to the EPFL secretaries: Sylvie, Melis, Kathlyn, and Marie, for their friendliness and assistance with administrative issues, and to my office-mates: Yves, Hui, Marc, Damien, Tanja, and Deniz, for sharing the space and moments with me. A very big thank you goes to my fellows and colleagues from LMIS2 and LMIS4. Sophie, Pierre, Emile, Yves, Rana, Diego, Fab, Matteo, Rima, Josias, Rob, Bilge, and Jules, you have welcomed me warmly at EPFL, have always cheered me up and supported as real friends, and encouraged for continuation of my research.

Last but not least, I truly thank my family for their support and belief in my abilities, which they have always expressed. Thank you, Michal, for being the fantastic companion – as a loving husband, and an ingenious scientist-engineer. You have constructively improved my thesis, articles and presentations, providing me with a great scientific feedback; you helped me to solve my research problems, giving me an extraordinary engineering feedback. Furthermore, you have always encouraged me

## **Acknowledgements**

---

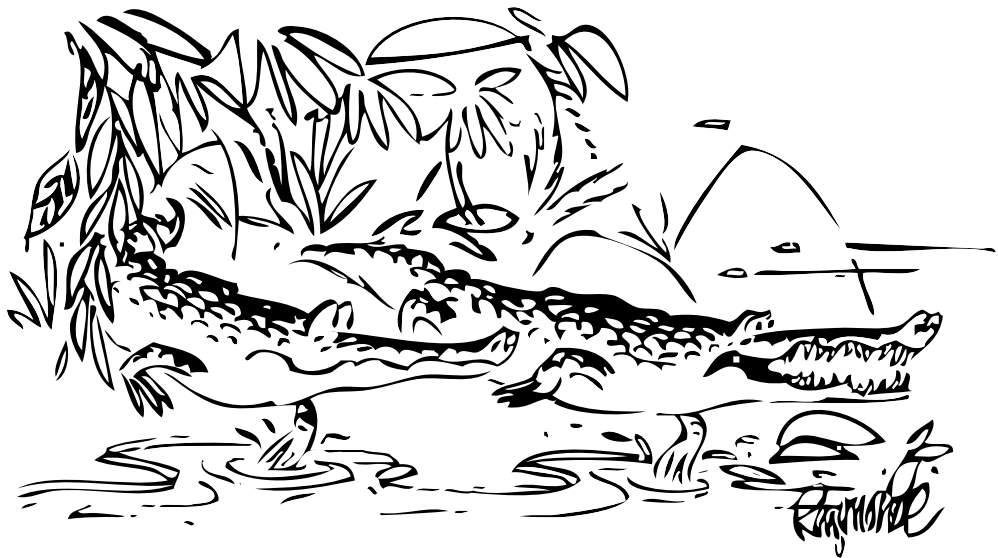
and trusted in me, so I have always had from you an essential and endless emotional feedback. Thank you, petite Sophie, moja duszko, your existence has been for me the most tremendous motivation of my life.

*Lausanne, 28 November 2012*

Jagoda Dobrzynska



*"Artificial or not - there's always some damned perfectionist wants the real thing!"*







# Abstract

Today many robotic and prosthetic applications involve secure gripping, handling, and dexterous manipulation of objects. Such operations require an adequate tactile and force sensing mechanism – ideally a large-area flexible sensory organ to adapt to an arbitrary shape of a body of a robot or prosthetic limb. In recent years, micro-machined force sensors in elastic packagings have gained interest, and exhibited vast potential for application in artificial skins.

This thesis work presents new approaches for a flexible force sensing scheme, namely focusing on *micromachined capacitive force sensors* and *flexible polymeric substrates*. First, novel designs of capacitive sensors for uni-axial/one-dimensional (1D) and three-axial/three-dimensional (3D) force measurements are presented. Further, clean room batch-type microfabrication processes are described, which have been developed to obtain the sensor prototypes. These processes involved an integration of the sensor into flexible polymeric films, and the development of innovative material concepts for the latter.

An original *flexible capacitive sensor for 1D large force measurements* was designed, modelled and manufactured. Polyimide fabrication technologies and a robust bonding scheme allowed obtaining flexible-substrate-based sensors with an excellent durability and resistance to forces when operated in the 0-1 kN range. The experiments confirmed that the sensor can perform measurements of uni-axial load also on surfaces with curvatures.

Moreover, a novel *flexible capacitive sensor for 3D force measurements* was developed, to measure the three-axial loads in the range of those perceived by human skin. Flexible sensors were manufactured by a robust integration of metallization processes with polymer technologies of polyimide, Parylene-C, and polydimethylsiloxane. The sensors permitted the measurement of a three-axial force, with a high shear force sensitivity  $S_x = 2.8 \cdot 10^{-4} \text{ kPa}^{-1}$ . It was proven in the experiments that the 3-axial sensitivities of the sensors place the latter exactly in the region of interest for human hand- and foot-artificial skin applications.

## Abstract

---

Finally, an innovative concept of a flexible polymeric substrate was introduced, namely thin *flexible films with custom-designed microporosity*. Polypropylene carbonate-based processes allowed for the realization of foam-like polyimide films with 20-200  $\mu\text{m}$  wide air chambers at precisely predetermined positions. While maintaining the desired mechanical and chemical properties of polyimide, the reduction of the material's elastic modulus and stiffness was achieved, as shown by nanoindentation and microcompression experiments.

**Keywords:** *artificial skin, tactile sensing, skin-like sensor, capacitive sensor, flexible sensor, polymer sensor, force sensor, three-axial force, 3D force, porous polyimide, polyimide foam, microporosity*

## Résumé

De nos jours, de nombreuses applications robotiques et prothétiques nécessitent une prise sûre et une manipulation adroite d'objets. De telles opérations requièrent un mécanisme de mesure de force et de toucher adéquat— idéalement un organe sensitif flexible de large surface qui puisse s'adapter à un robot ou à une prothèse de forme quelconque. Durant les dernières années, les capteurs de force microfabriqués et emballés dans des emballages élastiques ont gagné de l'intérêt et montré un vaste potentiel d'applications pour les peaux artificielles.

Dans ce travail de thèse, de nouvelles approches pour un système flexible de capteur de force sont présentées en se focalisant sur des capteurs de force capacitifs microfabriqués ainsi que sur des substrats polymères flexibles. Dans un premier temps, de nouveaux concepts de capteurs capacitifs pour mesures uniaxiales/unidimensionnelles (1D) et triaxiales/tridimensionnelles (3D) sont présentés. Les procédés de microfabrication par lots développés en salle blanche pour l'obtention de prototypes de capteurs sont ensuite décrits. Ces procédés impliquent l'intégration d'un capteur dans des fines couches de polymères flexibles et le développement de concepts novateurs dans l'utilisation des matériaux.

Un capteur capacitif flexible original pour des mesures de grande force en une dimension a été conçu, modélisé et manufacturé. Les technologies de microfabrication du polyimide ainsi qu'un système robuste de connectique ont permis d'obtenir des capteurs sur substrats flexibles de durabilité et de résistance aux forces excellentes lors de leur utilisation dans la gamme de 0 à 1 kN. Les expériences ont confirmé que le capteur peut effectuer des mesures uniaxiales également sur des surfaces courbées.

Par ailleurs, un capteur capacitif flexible novateur pour des mesures en 3D a été développé afin de mesurer des charges de l'ordre de celles qui sont perçues par la peau humaine. Des capteurs flexibles ont été manufacturés par l'intégration fiable de procédés de métallisation aux technologies polymères du polyimide, du Parylène-C et du polydiméthylsiloxane. Les capteurs ont permis de mesurer une force triaxiale avec une sensibilité aux forces de cisaillement  $S_x = 2.8 \cdot 10^{-4} \text{ kPa}^{-1}$ . Il a été prouvé durant les expériences que les sensibilités triaxiales du capteur placent celui-ci exactement dans la région d'intérêt pour des applications dans le domaine des peaux artificielles

## Résumé

---

pour mains et pieds humains.

Finale­ment, un concept innovant de substrats polymères flexibles a été intro­duit, à savoir des films flexibles avec une microporosité contrôlée. Un procédé fondé sur le polypropylène carbonate a permis la réalisation de films de polyimide ressemblant à une éponge avec des chambres d'air larges de 20 à 200  $\mu\text{m}$  à des positions préci­sement prédéterminées. Une réduction du module élastique a été réalisée tout en maintenant les propriétés mécaniques et chimiques désirées du polyimide, ainsi que des expériences de nanoindentation et de microcompression l'ont montré.

**Mots-clés :** *peau artificielle, capteurs tactiles, capteurs capacitifs, capteurs flexibles, capteurs polymères, capteurs de force, force triaxiale, force 3D, polyimide poreux, éponge de polyimide, microporosité.*

# Zusammenfassung

Viele Arbeiten, die von Robotern und Prothesen verrichtet werden, sind auf das zuverlässige Greifen und einen geschickten Umgang mit Objekten aller Art angewiesen. Solche Arbeitsvorgänge benötigen einen zweckdienlichen Tast- und Kraft-Messmechanismus – idealerweise einen grossflächigen flexiblen Sensor, welcher sich an beliebige Körperformen eines Roboters oder einer Prothese anpasst. In den letzten Jahren haben mikrotechnologisch hergestellte Kraftsensoren, die in elastischen Materialien beträchtliche Aufmerksamkeit erhalten und ein grosses Potential als künstliche Haut gezeigt.

Diese Doktorarbeit zeigt neue Herangehensweisen auf, wie ein flexibler Kraftsensor hergestellt werden kann, und behandelt namentlich *mikrotechnologisch produzierte kapazitative Kraftsensoren* sowie *biegbare Trägermaterialien aus Kunststoff*. Zuerst werden neuartige Designs für kapazitative Sensoren zur einachsigen/eindimensionalen (1D) und dreiachsigen/dreidimensionalen Kraftmessung vorgestellt. Ferner werden verschiedene mikrotechnologische Losfertigungsprozesse beschrieben, die zur Herstellung der Sensorprototypen entwickelt worden sind. Diese Prozesse beinhalteten das Einbetten des Sensors in flexiblen Polymerfilmen und die Entwicklung innovativer Materialkonzepte hierfür.

Ein grundlegend neuer *biegbarer kapazitiver Sensor zur Messung grosser eindimensionaler Kräfte* ist entworfen, modelliert, hergestellt und getestet worden. Polyimidbasierte Produktiostechnologien und ein robustes Bondieren ermöglichten die Herstellung von Sensoren, die auf einem flexiblen Substrat beruhen und eine hervorragende Beständigkeit und Festigkeit gegenüber Kräften aufweisen, wenn sie im Bereich von 0 bis 1 kN betrieben werden. Die Experimente bestätigten, dass der Sensor Messungen einachsiger Lasten auch auf gebogenen Oberflächen durchführen kann.

Ausserdem wurde ein neuartiger *biegbarer kapazitiver Sensor zur Messung dreidimensionaler Kräfte* entworfen, um dreiachsige Kräfte zu messen, die im Lastbereich liegen, der auch von der menschlichen Haut abgedeckt wird. Biegbare Sensoren sind mittels einer robusten Kopplung von Metallisierungsprozessen mit Polymertechnologie (Polyimid, Parylen-C und Polydimethylsiloxan) hergestellt worden. Die Sensoren erlaubten es, dreiachsige Kräfte mit einer hohen Empfindlichkeit gegenüber Schub-

## Zusammenfassung

---

kräften ( $S_x = 2.8 \cdot 10^{-4} \text{kPa}^{-1}$ ) zu messen. Es wurde experimentell gezeigt, dass die Empfindlichkeit auf dreiachsige Kräfte den Sensor genau in dem Bereich verorten, der für eine künstliche Fuss- und Handhaut von Interesse ist.

Schliesslich wurde ein innovatives Konzept eines biegbaren Kunststoffsubstrates eingeführt, namentlich dünner *biegbarer Schichten mit einer massgeschneiderten Mikroporosität*. Prozesse, die Polypropylencarbonat verwenden, ermöglichten es, schwammähnliche Polyimid-Filme mit 20-200  $\mu\text{m}$  breiten Luftkammern an genau vordefinierten Stellen anzufertigen. Während die erwünschten mechanischen und chemischen Eigenschaften von Polyimid beibehalten wurden, wurde eine Verminderung des Elastizitätsmoduls erzielt, wie es Nanoindentierungs- und Mikrokompressionsexperimente zeigen.

**Schlagnorte:** *künstliche Haut, Berührungssensorik, hautähnlicher Sensor, kapazitiver Sensor, flexibler Sensor, biegbarer Sensor, Kraftsensor, dreiachsige Kraft, 3D-Kraft, poröses Polyimid, Polyimidschaum, Mikroporosität*

## Sommario

Attualmente molte applicazioni robotiche e protesiche richiedono una presa sicura e un'abile manipolazione degli oggetti. Tali operazioni richiedono un adeguato meccanismo di rilevamento sia tattile che di forza - idealmente un organo sensoriale flessibile che ricopra una vasta area, in grado di adattarsi a una forma arbitraria del corpo di un robot o di un arto protesico. Negli ultimi anni, sensori di forza microfabbricati in packaging elastici hanno guadagnato interesse, ed hanno dimostrato un grande potenziale per la loro applicazione nel campo della pelle artificiale.

Questo lavoro di tesi presenta un nuovo approccio per lo sviluppo di un sistema di rilevamento flessibile di forza, focalizzandosi su sensori di forza capacitivi microlaborati e su supporti polimerici flessibili. In primo luogo, vengono presentati design innovativi di sensori capacitivi per misure di forza sia uniassiali/unidimensionali (1D), sia triassiali/tridimensionali (3D). Inoltre, vengono descritti i processi di microfabbricazione in batch che sono stati realizzati in camera pulita per ottenere i prototipi di sensore. Questi processi hanno incluso l'integrazione del sensore in film flessibili polimerici, e lo sviluppo di concetti innovativi sui materiali necessari per questi ultimi.

Un originale sensore capacitivo flessibile per misure unidimensionali di forze elevate è stato progettato, modellizzato e realizzato. Tecnologie di fabbricazione in poliimmide e uno schema di bonding robusto hanno permesso di ottenere sensori su supporto flessibile con un'eccellente durata e resistenza alle forze, quando utilizzato nel range 0-1 kN. Gli esperimenti hanno confermato che il sensore può effettuare misure di carico uniassiale anche su superfici curve.

Inoltre, è stato sviluppato un nuovo sensore capacitivo flessibile per misure di forza 3D, in grado di misurare carichi lungo i tre assi nello stesso range di forze percepite dalla pelle umana. Sono stati realizzati sensori flessibili grazie ad una robusta integrazione dei processi di metallizzazione con le tecnologie polimeriche in poliimmide, Parilene-C, e polidimetilsilossano. I sensori hanno consentito la misurazione di forza lungo i tre assi, con un'elevata sensibilità dello sforzo di taglio pari a  $S_x = 2.8 \cdot 10^{-4} \text{ kPa}^{-1}$ . Tramite diversi esperimenti è stato dimostrato che la sensibilità dei sensori lungo i tre assi è tale da rientrare esattamente nel range di applicazione per pelli artificiali di mani e piedi.

## Sommario

---

Infine, è stato introdotto un concetto innovativo di substrato polimerico flessibile, ovvero quello di film flessibili sottili con microporosità scelta su misura. Processi basati sul carbonato di polipropilene hanno consentito la realizzazione di film in poliimmide con struttura simile alla schiuma, con camere d'aria di dimensione di 20-200  $\mu\text{m}$ . in posizioni definite con accuratezza. Pur mantenendo le proprietà meccaniche e chimiche desiderate della poliimmide, è stato possibile ottenere una riduzione del modulo elastico del materiale come dimostrato da esperimenti di nanoindentazione e microcompressione.

**Parole chiavi :** *pelle artificiale, rilevamento tattile, sensore simile alla pelle, sensore capacitivo, sensore flessibile, sensore polimerico, sensore di forza, forza tri-assiale, forza 3D, poliimmide porosa, schiuma di poliimmide, microporosità.*



# Contents

<b>Acknowledgements</b>	<b>iii</b>
<b>Abstract (English/Français/Deutsch/Italiano)</b>	<b>ix</b>
<b>Contents</b>	<b>xix</b>
<b>Nomenclature</b>	<b>xxi</b>
<b>List of figures</b>	<b>xxvi</b>
<b>List of tables</b>	<b>xxvii</b>
<b>1 Introduction</b>	<b>1</b>
<b>2 Tactile sensing: from human skin to artificial receptors</b>	<b>5</b>
2.1 Cutaneous receptors in human skin . . . . .	5
2.2 Human skin tactile perception . . . . .	6
2.3 Requirements to artificial mimicking of human tactile sensing . . . . .	8
2.4 Tactile sensing implemented . . . . .	9
2.4.1 Actuator effort sensors . . . . .	9
2.4.2 Force/torque sensors . . . . .	10
2.4.3 Tactile sensors . . . . .	11
2.4.4 Commercial sensors summary . . . . .	12
2.5 Microfabricated force sensors . . . . .	12
2.5.1 Micromachined piezoresistive sensors . . . . .	13
2.5.2 Micromachined strain gauge-based sensors . . . . .	15
2.5.3 Micromachined piezoelectric sensors . . . . .	16
2.5.4 Micromachined conductive polymer sensors . . . . .	17
2.5.5 Transistor-based sensors . . . . .	19
2.5.6 Micromachined optical sensors . . . . .	21
2.5.7 Micromachined magnetic and inductive sensors . . . . .	22
2.5.8 Micromachined capacitive sensors . . . . .	23

## Contents

---

2.5.9	A comparison of micromachined sensor solutions and sensing techniques . . . . .	28
<b>3</b>	<b>Flexible capacitive sensor for uni-axial large force measurements</b>	<b>35</b>
3.1	Introduction . . . . .	36
3.2	Materials and methods . . . . .	37
3.2.1	Design of the capacitive sensor . . . . .	37
3.2.2	Microfabrication process of the PI-based sensor . . . . .	38
3.2.3	Optical inspection of the fabrication process results . . . . .	40
3.2.4	Sensor packaging . . . . .	41
3.3	Modelling and electrical characterization . . . . .	42
3.3.1	Modelling of the finger-like capacitive sensor . . . . .	42
3.3.2	Electro-mechanical characterization of the uni-axial force sensor	46
3.4	Summary and discussion . . . . .	49
<b>4</b>	<b>Flexible capacitive sensor for three-axial force measurements</b>	<b>51</b>
4.1	Introduction . . . . .	52
4.2	Materials and methods . . . . .	53
4.2.1	Design of the three-axial capacitive sensor . . . . .	53
4.2.2	Microfabrication process of the polymer-based sensor . . . . .	55
4.2.3	Optical inspection of the fabrication process results . . . . .	58
4.3	Modeling and electro-mechanical characterization . . . . .	61
4.3.1	Modeling of the capacitive force sensor . . . . .	61
4.3.2	Electro-mechanical characterization of the 3-axial force sensor	63
4.4	Comparison between the sensitivity of the force sensor and the touch sense of human skin . . . . .	68
4.5	Summary and discussion . . . . .	69
<b>5</b>	<b>Flexible films with custom-designed microporosity</b>	<b>71</b>
5.1	Introduction . . . . .	72
5.2	Polymeric foams . . . . .	73
5.3	Microfabrication process of foam-like PI films . . . . .	75
5.3.1	Sacrificial material coating . . . . .	75
5.3.2	Mask deposition . . . . .	76
5.3.3	Sacrificial material etch . . . . .	77
5.3.4	Al barrier layer and PI overcoating . . . . .	79
5.3.5	Baking steps for PPC decomposition and PI polymerization . . .	80
5.3.6	Optical inspection of the fabrication process results . . . . .	82
5.3.7	Notes on the process . . . . .	82
5.4	Modelling of microcavity deformation under stress . . . . .	86

5.5	Compression experiments of microporous layers . . . . .	88
5.5.1	Conventional nanoindentation setup . . . . .	89
5.5.2	Home-built microcompressor tester . . . . .	91
5.6	Summary and discussion . . . . .	93
<b>6</b>	<b>Conclusions and outlook</b>	<b>95</b>
6.1	Flexible capacitive sensor for uni-axial large force measurements . . . . .	95
6.2	Flexible capacitive sensor for three-axial force measurements . . . . .	96
6.3	Flexible films with custom-designed microporosity . . . . .	97
6.4	Towards artificial skin . . . . .	98
<b>A</b>	<b>Appendix A</b>	<b>101</b>
<b>B</b>	<b>Appendix B</b>	<b>103</b>
	<b>Bibliography</b>	<b>126</b>
<b>C</b>	<b>Publications</b>	<b>127</b>
	<b>Curriculum Vitae</b>	<b>129</b>



# Nomenclature

---

## Abbreviations and Acronyms

---

1D	one-dimension(al)
2D	two-dimension(al)
3D	three-dimension(al)
Al	aluminum
Ar	argon
Au	gold
$\text{BCl}_3$	boron trichloride
CF	carbon fiber
Cl	chlorine
CMOS	complementary metal–oxide–semiconductor
CNT	carbon nanotube
Cr	chromium
Cu	copper
DMA	dynamical mechanical analyzer
DOF	degree of freedom
DRIE	deep reactive ion etching
DSC	differential scanning calorimetry
FEM	finite element method
FET	field effect transistor
FPCB	flexible printed circuit board
FSR	force-sensitive resistor
F/T	force and torque
Ge	germanium
GRF	ground reaction force
HF	hydrofluoric acid
HBP	hyperbranched polymer
IC	intergraded circuit
ICP	inductively coupled plasma
IPMC	ionic polymer metal composite

## Nomenclature

---

---

### Abbreviations and Acronyms – continued from previous page

---

MEMS	microelectromechanical systems
MOS	metal–oxide–semiconductor
MW	molecular weight
N <sub>2</sub>	nitrogen
Ni	nickel
NMP	n-methyl-2-pyrrolidone
NW	nanowire
O <sub>2</sub>	oxygen
OFET	organic field effect transistor
OTFT	organic thin-film transistor
PCB	printed circuit board
PCR	pressure-conductive rubber
PDMS	polydimethylsiloxane
PEC	polyethylene carbonate
PECVD	plasma-enhanced chemical vapour deposition
PEN	polyethylene naphthalate
PI	polyimide
PMMA	polymethylmethacrylate
PNB	polynorborene
POF	plastic optical fiber
POSFET	piezoelectric oxide semiconductor field effect transistor
PPC	polypropylene carbonate
PR	photoresist
Pt	platinum
PVD	physical vapour deposition
PVDF	polyvinylidene fluoride
RT	room temperature
SEM	scanning electron microscopy
Si	silicon/silicium
SiN	silicon nitride
SiO <sub>2</sub>	silicon dioxide
SF <sub>6</sub>	sulfur hexafluoride
TCD	tetracyclododecene
TGA	thermal gravimetric analysis
Ti	titanium
TrFE	trifluoroethylene
TS	Taylor series
TFT	thin-film transistor

---

**Abbreviations and Acronyms** – continued from previous page

---

UV	ultraviolet (light), ~10 nm–400 nm wavelength
W	tungsten
XPS	X-ray photoelectron spectroscopy
Zn	zinc

---



---

**Symbols**

---

$A$	area [m <sup>2</sup> ]
$\beta, a$	geometrical coefficients [-]
$C$	capacitance [F]
$\gamma$	shear strain [-]
$E$	Young's modulus [Pa]
$\epsilon$	dielectric constant, permittivity [-]
$\epsilon_z$	normal strain [-]
$f$	frequency [Hz]
$F$	force [N]
$G$	shear modulus [Pa]
$h$	height, depth / vertical distance [m]
$H$	hardness [Pa/m <sup>2</sup> ]
$L$	length [m]
$n$	number / quantity [-]
$\nu$	Poisson's ratio [-]
$P$	pressure [Pa]
$s$	spacing [m]
$S$	stiffness [N/m]/[Pa/m]
$\sigma$	compressive stress [Pa]
$t$	thickness [m]
$T_b$	boiling temperature [°C]
$T_g$	glass transition temperature [°C]
$\tau$	shear stress [Pa]
$w$	width [m]
$x$	transverse / horizontal displacement [m]
$z$	vertical displacement / deflection [m]
$Z$	impedance [ $\Omega$ ]

---

## Nomenclature

---

---

### Constants

---

$\varepsilon_0$	electric permittivity of vacuum ( $8.8541878 \cdot 10^{-12}$ F/m)
$\zeta$	nanoindenter's geometrical constant (of the order of unity)

---



# List of Figures

1.1	Examples of human-friendly robots. . . . .	2
1.2	Principle of operation of capacitive sensors introduced in this thesis. .	3
2.1	Mechanoreceptors in human skin. . . . .	6
2.2	Pressure distribution maps of a hand and feet. . . . .	7
2.3	An industrial robot with typical load sensors. . . . .	10
2.4	Examples of literature-reported piezoresistive tactile sensors. . . . .	13
2.5	Examples of literature-reported strain gauge-based tactile sensors. . .	16
2.6	Examples of literature-reported piezoelectric tactile sensors. . . . .	17
2.7	Examples of literature-reported conductive polymer sensors. . . . .	18
2.8	Examples of literature-reported transistor-based tactile sensors. . . . .	20
2.9	Examples of literature-reported capacitive tactile sensors. . . . .	24
2.10	The flexible capacitive 3-axial force sensor by Lee. . . . .	25
2.11	The flexible capacitive 3-axial force sensor by Cheng. . . . .	26
3.1	A conceptual view of the flexible capacitive force sensor. . . . .	37
3.2	Process flow for the fabrication of the capacitive sensor. . . . .	39
3.3	SEM cross-section micrographs of the fabrication steps of a smooth slope in PI. . . . .	40
3.4	A single manufactured capacitive force sensor. . . . .	41
3.5	The results of the X-ray photoelectron spectroscopy analysis of the contact pad surface. . . . .	42
3.6	The fabricated flexible sensor and an illustration of the bonding technique.	43
3.7	Results from a 2D simulation of the electrical field and potential for the capacitive sensor. . . . .	44
3.8	Simulation curves and the measurement results of an unloaded sensor.	45
3.9	Experimental setup and sensitivity of the sensor. . . . .	46
3.10	Measurement results of a loaded sensor. . . . .	47
3.11	Measurement results of a sensor when loaded on flat and non-flat surfaces.	50
4.1	A conceptual exploded view of the layers of the flexible capacitive force sensor. . . . .	53

## List of Figures

---

4.2	A conceptual view of the flexible capacitive force sensor. . . . .	54
4.3	Simulation of capacitance change dependent upon sensor geometry. . .	55
4.4	Process flow for the fabrication of the capacitive sensor. . . . .	56
4.5	The fabricated flexible sensor and an illustration of the bonding technique.	57
4.6	The fabricated flexible sensor. . . . .	59
4.7	SEM cross-section views and simulation results of the capacitive sensor.	60
4.8	Comparison between different PRs used in the fabrication of the top electrode. . . . .	61
4.9	Simulation curves and measurement results of an unloaded sensor. . .	62
4.10	Experimental setup. . . . .	64
4.11	Measurement results upon normal force applied to the sensor. . . . .	65
4.12	Measurement results upon shear force applied to the sensor. . . . .	66
4.13	Measurement results upon shear force applied to the sensor cd. . . . .	68
4.14	Sensitivity of the sensor. . . . .	69
5.1	A conceptual view of a foam-like material, in application to a pressure- sensitive sensor with a body site-dependent sensitivity. . . . .	73
5.2	Process flow for the fabrication of the microporous PI layer. . . . .	76
5.3	Micrographs of microfabrication process steps. . . . .	78
5.4	Chemical analysis results for the PI and PPC materials. . . . .	81
5.5	SEM cross-section views of the fabricated microfoams. . . . .	83
5.6	Micrographs of microfabrication process steps that exhibited major challenges. . . . .	85
5.7	Results from a 2D simulation of stress and deformation of a microcavity.	87
5.8	Simulation curves for deformation of the cavities under stress. . . . .	88
5.9	Nanoindentation results. . . . .	90
5.10	Microcompressor setup. . . . .	91
5.11	Microcompression results. . . . .	92
A.1	Capacitance of three strip lines and a plane. . . . .	101

## List of Tables

2.1	Comparison of the micromachined force sensors selected from literature.	28
2.2	Comparison of the force-sensing principles. . . . .	32
3.1	Comparison of capacitive force-detecting sensors. . . . .	49
5.1	Test results for different sacrificial PPC and PI overcoat layers. . . . .	77
5.2	Furnace baking steps for PPC decomposition and PI polymerization. . .	80
6.1	Characteristics of the developed artificial sensors and porous films. . .	99



To my daughter,  
Sophie Aster



# 1 Introduction

In 1939, science fiction writer Isaac Asimov authored the first story about harmless robots who help humanity [1]. In the story, set in the futuristic year 1996, the hero was a nursemaid robot (figure 1.1a). Surprisingly, exactly at that time, a robot was indeed developed to perform various household tasks with humans in daily life (figure 1.1b). For the first time in history a robot prepared a man scrambled eggs for breakfast [2], and science fiction became science fact.

Today, human-robot symbiosis is ubiquitous. Paralyzed patients use neural signals to control and navigate robotic arms *via* brain implants [3]. A therapeutic seal-robot calms patients in hospitals [4], welfare-robots transport patients in nursing homes [5] (figure 1.1d), while bartender-robots serve clients [6]. In manufacturing plants, industrial robots work in close proximity to and together with humans [7, 8]. Crowning the accomplishments of human-robot symbiosis, a bionic boy, fitted with an advanced hand prosthesis, carried the 2012 Olympic Torch [9, 10].

Eventually, robots will escape from their well-organized corner of a factory and will start dealing with the unstructured environment of the surrounding everyday world [14]. Thus, they will require human-friendly soft features [15, 16] and a variety of sensory information, including tactile cognition, to navigate, manipulate objects, protect themselves, and to protect humans in their neighborhood. An *artificial skin* – a synthetically-acquired flexible large-area sensing organ – could endow the robots with the ultimate sense of touch. Indeed, for many prosthetic and robotic applications, which require dexterous manipulation and safe interaction with people, the development of an artificial skin is of profound interest.

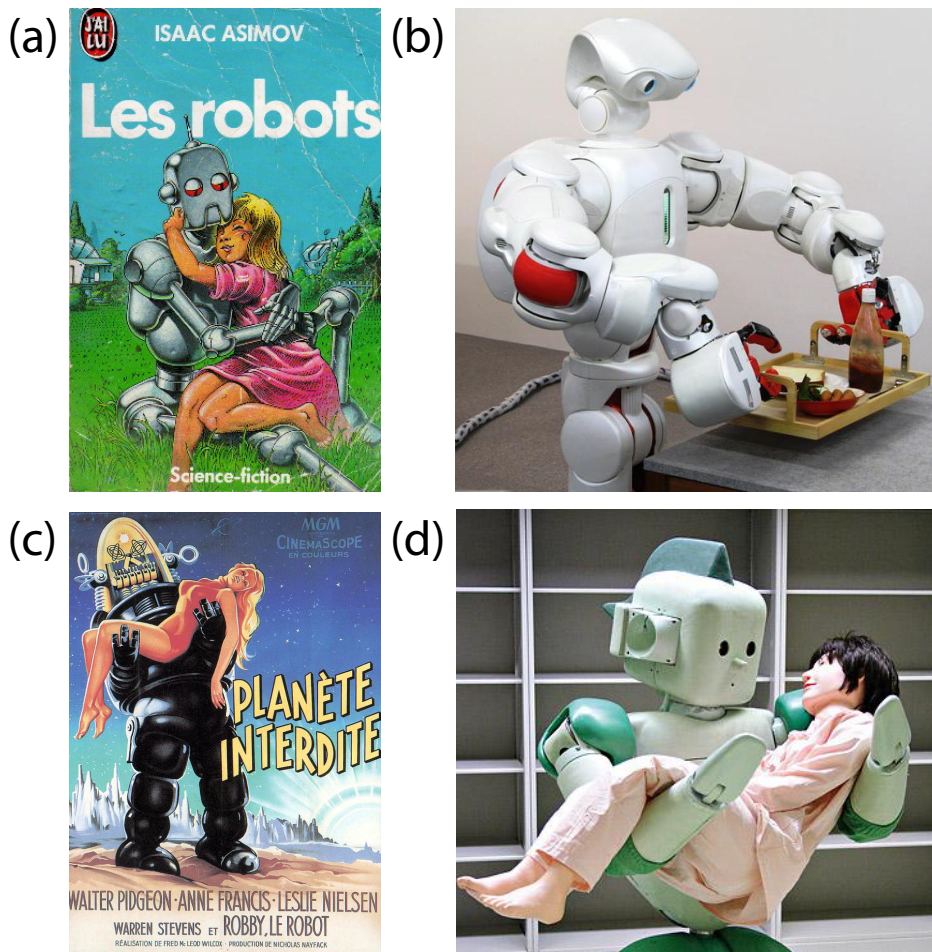


Figure 1.1: Robots providing help to humanity and assisting in daily-life activities: (a) a book cover of a 1939 science-fiction tale about a girl and her nanny-robot [11]; (b) a human-symbiotic robot TWENDY-ONE (2012) carrying a tray with breakfast for a caretaker [12]; (c) Hollywood's 1956 vision of a robot saving a crew member from a starship crash [13]; (d) a welfare-task RI-MAN robot (2012) transporting a hospital patient [5].

The constant miniaturization in engineering science has led to the development of remarkable *micromachining* techniques for mass-production of devices with small volume and weight, which are operational, sensitive and accurate with minimal amount of required space [17]. In particular, recent work on *micromachined force sensors* in *flexible* packages exhibited vast potential for the application in an artificial skin. Technological advances have already resulted in small and thin sensors, with high spatial resolution sensing cells. Integrated in *flexible polymeric substrates*, such sensors can be fixed on the non-planar surfaces of robotic bodies, human medical prostheses, or can be used in other applications, where large-area surface conformability, flexibility, deformability, and even stretchability of the skin-like substrate is



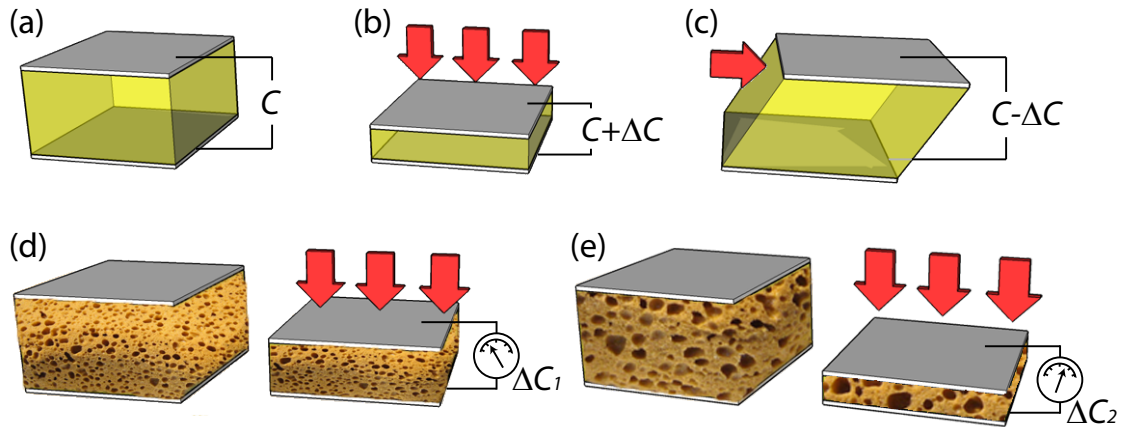


Figure 1.2: Principle of operation of capacitive sensors introduced in this thesis, consisting of a dielectric sandwiched by two metal electrodes. (a) A capacitive sensor under zero-load conditions (initial capacitance  $C$ ). (b) Compressive and (c) shear force applied to the sensor (change in capacitance by  $\Delta C$ ). (d, e) Compressive force applied to the sensor with a foam-like dielectric layer of custom-designed porosity (d) with low void fraction, and (e) with high void fraction. Under the same load, the capacitor shown in (e) is more compressed than the one in (d), thus a bigger change in capacitance is obtained ( $\Delta C_2 > \Delta C_1$ ).

necessary [18]. Amongst the sensors, one class of devices that can readily measure force are *capacitive* transducers. In capacitive sensors, upon load application, a flexible dielectric between the electrodes deforms, changing the geometry, and hence the capacitance value of the touch-sensitive cell.

This thesis focuses on *micromachined capacitive force sensors* and *flexible polymeric substrates* as promising concepts *towards an artificial skin*. The miniaturisation of the sensors yields a dense spatial arrangement onto large-area substrates. Micromachined capacitors are readily placed, with high spatial resolution, on flexible and large-area expandable polymer materials, which can in turn conformally cover robotic or prosthetic body surfaces. The capacitive approach offers high sensitivity and demonstrates both uni-axial and three-axial force sensing-capabilities.

Within the scope of this work, *micromachined capacitive sensors on flexible polymeric substrates* are developed and tested. The sensors measure normal loads, which induce a change in capacitance by reducing the spacing between the electrodes (figure 1.2b), and shear loads, which change the overlap-area of the electrodes (figure 1.2c). Moreover, an innovative concept of flexible cellular polymeric film is presented, which has the potential to be integrated into these sensors as a foam-like dielectric with customizable elasticity (figures 1.2d, e).

## Chapter 1. Introduction

---

Chapter 2 gives an overview on aspects of human and artificial tactile sensing. In particular, the state of the art in artificial touch sensors and tactile-sensing technologies is presented, with focus on capacitive sensors and sensors deposited on flexible polymeric substrates.

In chapter 3, an original *flexible capacitive sensor for uni-axial large force measurements* is presented. The design of the transducer and its theoretical model is introduced. I report on the microfabrication process and bonding techniques for obtaining a robust device. I demonstrate experimentally the durability and resistance of the prototype to large forces, and the reliable operation under uni-axial loads when placed on non-planar surfaces. The sensor brings promise for application to industrial robots, to measure grasp force while conforming to arbitrary gripper geometries.

Chapter 4 reports on a novel *flexible capacitive sensor for three-axial force measurements*. The design of the finger-shaped sensor electrodes is introduced, rendering a prototype for the measurement of 3D load with high sensitivity in all axes. Also a theoretical model of the capacitive transducer is provided. I present the microfabrication process of the sensor, based on flexible polymer technologies. The device undergoes loading experiments under a three-axial force to reveal the normal- and shear-force sensitivities of the tactile cells. The experimental results are compared with the typical range of forces appearing on human skin in the hand- and foot-areas, showing potential of the sensor for skin-like prosthetic and robotic applications.

An innovative concept of a flexible polymeric substrate is introduced in chapter 5. The development of thin *flexible films with custom-designed microporosity* is discussed, including the detailed microfabrication process steps and manufacturing challenges. I present analytical and numerical methods to model the mechanical stress–strain properties of the micropores. Compression tests of microporous films demonstrate an improvement of the elasticity for a foam-like layer when compared to non-porous films made of the same polymer. This sponge-like material is envisioned for future artificial skin size-expansions into large-area surfaces of prosthetic and robotic systems.

Finally, the results and findings of this work are summarized in chapter 6 and I conclude with an outlook for future applications of artificial skin.

## 2 Tactile sensing: from human skin to artificial receptors

By definition, the sense of touch refers to the sensations caused by physical contact between an external object and a sensory organ [14, 19]. Such an organ is, *e.g.*, the skin of a living organism; nevertheless skin-like touch-sensitive receptors can be also produced in an artificial manner.

This chapter gives an overview on the tactile sensing. In particular, it treats the sensing process, the requirements for tactile sensing, and emerging engineering approaches to develop tactile sensors. The following sections give an introduction to the science of human skin receptors and tactile perception. From this, the requirements for the design of artificial tactile sensing systems are deduced. Finally, a state of the art in artificial tactile sensing technologies is presented. A literature review focuses on *microfabricated force sensors* for uni-axial and three-axial force measurements. A particular emphasis is put on *capacitive sensors* and sensors deposited on *flexible polymeric substrates*, as these represent the main contributions of this thesis.

### 2.1 Cutaneous receptors in human skin

The human skin is a mosaic of cutaneous receptors, which, distributed all over the body with variable density and embedded at different depths (figure 2.1), provide sensitiveness to fine touch, pressure, pain and temperature [19–22]. The response to mechanical stimuli is mediated by *mechanoreceptors*, the sensory receptors responsive to pressure and vibrations, having various receptive fields and rates of adaptation.

*Merkel* cells respond to sustained pressure at very low frequencies and the stimuli of spatial deformation, curvatures, edges, and corners. They are useful for texture perception, form and pattern detection, and tactile flow perception, playing an important role, *e.g.*, in reading Braille. *Ruffini* endings respond to sustained downward

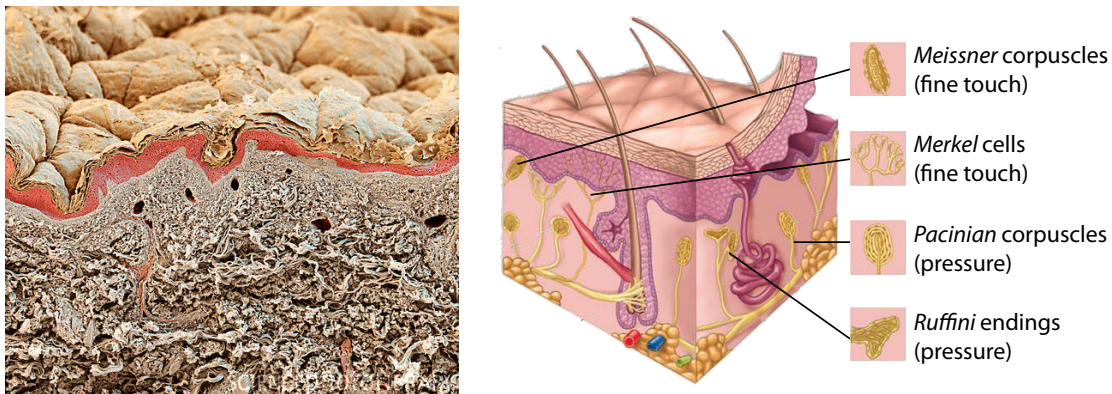


Figure 2.1: Section of human skin under a scanning electron microscope and a schematic showing the physical locations of mechanoreceptors. Two types of cutaneous receptors are sensitive to fine touch, and two other types are responsible for pressure sensing. Adapted from [23] © Science Photo Library and [21] © 2008 McGraw-Hill.

pressure at high frequencies, to lateral skin stretch and skin slip. They are responsible for motion detection, and tangential force determination on skin surface, enabling, *e.g.*, proper finger position when gripping an object, and a stable grasp. *Meissner* corpuscles respond to low-frequency vibrations, as caused by *e.g.* a slipping object across fingers. *Pacinian* corpuscles respond to high-frequency vibrations, experienced when an object first makes contact with skin, *e.g.*, when a mosquito lands on the arm.

The tactile sensation of the skin requires the four types of mechanoreceptors to always work together [24]. This complex and distributed nature of the human sense of touch remains challenging to be reproduced or substituted in an artificial manner [22].

As further shown in this thesis, artificial sensors can also support sensitivity both to fine touch and high pressure. Chapter 4 reports on an artificial tactile receptor, which mimics the tactile sensation provided with Merkel and Meissner's mechanoreceptors, and Pacinian and Ruffini corpuscles.

## 2.2 Human skin tactile perception

Human skin mechanoreceptors provide the sensory input for the central nervous system, *e.g.*, about hand orientation or foot placement. The information gathered, *e.g.*, from the skin of the fingertips or plantar surface of the foot, is used by the brain to actively control our hands for object manipulation or our feet for body-balance retention, respectively.

Hand-skin haptic data is a clue for deft manual performance. Object manipulation,

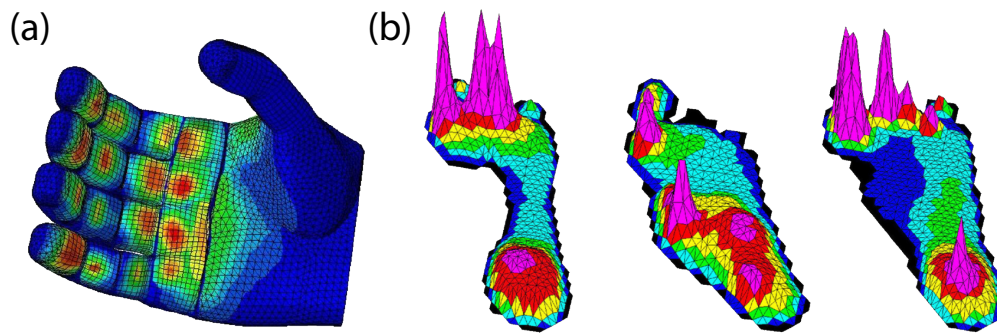


Figure 2.2: Pressure distribution maps of a hand and feet. (a) Pressure distribution on the hand surface when grasping a cylindrical handle [25] © 2011 IEEE. (b) Plantar pressure distribution of patients with severe foot deformation [26], with permission of Elsevier.

handovers [27], adjustment of grasp forces for gripping, adaptation to different grip object surfaces and weights [28], and collision detection [29, 30] are only possible when a sense of touch exists. In fact, when the sense of touch is removed, humans have great troubles performing [28, 31].

Various studies have evaluated hand skin touch-sensitivity and hand grasp force [28, 32–34] (figure 2.2a). The human skin at the hand fingertips is sensitive enough to perceive as little as 2.5 kPa of pressure, which corresponds to a gentle touch [33]. At the same time, the maximum fist grasp force ranges from 220–500 N, corresponding roughly to 150–350 kPa<sup>a</sup> exerted on the skin-parts of the hand that are in contact with the object [34]. A pressure of 5 N (~50 kPa<sup>a</sup>) is needed to hold a light rough object in between two fingers; when gripped, it will exert on our skin the shear force of 4 N (~40 kPa<sup>a</sup>) [28]. The same light object, but of slippery surface, requires a strong grip of 25 N of normal force (~250 kPa<sup>a</sup>) and 10 N of shear (~100 kPa<sup>a</sup>).

Nonetheless, tactile perception extends far beyond the hand-areas to the whole body surface covered with the skin. Likewise, the skin under the plantar surface of a foot provides important tactile sensation, which plays a crucial role for human balance and gait [35]. Plantar ground reaction force (GRF) data can provide clues towards the evaluation of patients' functional disabilities [26] (figure 2.2b) or progress after a surgical intervention [36]. Moreover, the sensitivity map of the foot is useful in creating footwear for better balance control and in designing comfortable shoes [37]. Numerous gait analysis studies assess human skin perception in the foot-area and the normal and shear GRF deformations of the plantar skin. Normal sole pressure when standing is ~15 kPa, while, in gait, pressures of up to 100 kPa in the midfoot, 250 kPa in the toes [38], and 170 kPa in the heel [39] can be observed. Foot shear pressure

<sup>a</sup>values interpreted from figures or estimated from the data available in the publications [28, 34]

accounts for up to 16% of normal force [40], resulting in peak shear pressures of 50 kPa in the heel and 90 kPa in the metatarsus [39].

Artificial skin-like tactile sensors can be of use for the evaluation of the forces existing when human skin is in contact with an object, or for the applications that mimic human skin tactile perception. Chapter 4 reports on a tactile sensor, whose range of measurable 3D forces and 3-axial sensitivity is compatible with the tactile sensation of human skin in the hand- and feet-areas.

### 2.3 Requirements to artificial mimicking of human tactile sensing

Based on the discussions of sections 2.1 and 2.2, the desirable features of artificial sensors, mimicking human sense of touch, can be formulated. Hints and requirements for the design of artificial tactile sensing systems have been earlier reported in review papers [22, 41, 42], and some of their main findings are summarized in this thesis.

Taking the analogy of the human skin, whose tactile sensibility depends on the body site [19], an artificial touch system should be a distributed *large-area* sensory organ, with a spatial resolution and sensitivity based on the body site where it is to be placed. In particular, for prosthetic applications, the spatial resolution should be 1–2 mm for more-sensitive areas [42], and 5 mm for the less-sensitive [22].

A critical ability required from a single *taxel* (tactile pixel) is the measurement of not only the *magnitude*, but also the *direction* of load [22, 41], a force vector which is referred to in this thesis as a *three-axial* or a *three-dimensional* (3D) force. In mechatronics, the detection of the 3D contact forces is important, *e.g.*, to sense the shape of an object in a gripper [43], to scan the surface texture [44, 45], and to recognize slip [45], or for robotic balance control [46] and walk stabilization [47–49]. Since human skin experiences constant 3-axial force deformations (see section 2.2), 3D aspects in sensing should be particularly considered, *e.g.*, when designing artificial skin for prosthetic applications.

An application-specific sensitivity and an adapted dynamic range are envisaged for touch-sensing systems. Considering sensors for prosthetics or symbiotic robots, the involved touch forces to be measured are in the range of those reported in section 2.2. In contrast, industrial robots operate in the kN range of contact forces, when gripping and manipulating objects [50].

In addition to the factors above, distributed tactile sensors should be ideally elastic, *flexible*, conformable [22], soft and stretchable [18]. For applications that require

determining forces against human body parts, the sensors must cover the involved body area surface and be conformal to its shape [51]. When distributed over a robotic body, touch sensors should only insignificantly increase the thickness of a part, and they should rather aim at simple integration methods [22]. Robust artificial touch systems should withstand harsh conditions of temperature, humidity, chemical stress, electric field, or sudden force [42].

Yet today, even with the state-of-the-art engineering science advancements, an integration of the above-mentioned design clues into a functioning system remains technologically challenging [22]. An envisaged solution is the integration of highly sensitive miniaturised 3D force sensors onto large-area flexible substrates in a dense spatial arrangement [41].

In this thesis, chapters 3 and 4 report on artificial tactile sensors, and chapter 5 on thin flexible films, whose features are comparable with those of a human skin.

## 2.4 Tactile sensing implemented

Since most of the robotic grippers employed in industry are designed on an *ad hoc* basis [52], a large number of robots have no sensory capabilities [14, 52] and their tasks are performed in a programmed sequence of movements, with “open gripper” and “close gripper” commands only. However, there are robots that possess some form of sensing, which, together with control systems, allow for handling of objects with a varying shape, for locating randomly placed targets, or for protecting against unexpected and dangerous situations [14].

This section presents a brief overview on the *commercial sensors* that are used in tactile sensing in robots and prostheses. Most systems use sensors that are widely available, and which can be divided into three main groups: actuator effort sensors, force and torque sensors, and tactile sensors (see figure 2.3).

### 2.4.1 Actuator effort sensors

One indirect method to measure the force at the point of contact with an object is to quantify the amount of the effort required by an actuator to perform the grasp or a touch-task. Information from the actuator effort sensors can be combined with knowledge about the robot geometry to estimate the location of, and the force at, the contact point [53].

For systems that use electric drives, a measure of the actuator effort can be obtained directly by measuring the motor current or the motor torque at the output of the

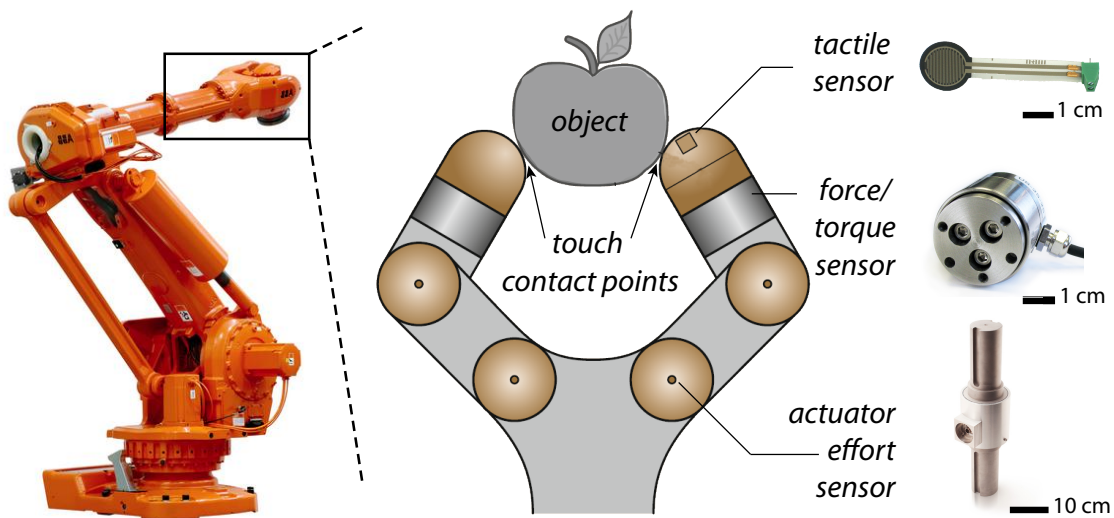


Figure 2.3: An industrial robot (courtesy of ABB) and its typical load sensors. Robotic hand scheme adapted from [53], © 2008 Springer. The hand is equipped with a tactile sensor (courtesy of Interlink Electronics), a force/torque sensor (courtesy of ATI Industrial Automation), and an actuator effort sensor (courtesy of FUTEK Advanced Sensor Technology).

gearbox. In commercial motors, solutions to this problem include resistors, which are embedded in series with the motor and measure voltage drop; shaft torque load cells furnished with strain gauges; and mechanical structures at the joint of a robotic arm whose deflections can be measured using electromagnetic or optical sensors [53]. For cable- or tendon-actuated arms and grippers, it is useful to monitor the cable tension, detected by strain gauges mounted on deflecting beams [14, 53]. The dexterous prosthesis Shadow Hand (Shadow Robot Company) [54] is equipped with sensors on tendon-based pneumatic artificial muscles, to allow its precise control. The pressure-driven control of the pneumatic drive of the Bionic Handling Assistant (Festo) [55] results in a smooth movement of a robotic arm and in the precise grasp of an elephant's trunk-like robotic gripper (see figure on the front-page of chapter 3).

### 2.4.2 Force/torque sensors

Force and torque sensors are found most often at the base joint or wrist of a robot, but can also be distributed throughout its body [53]. Any type of multiaxis load cell can be used to sense the manipulator force and torque. However, miniaturized six degrees of freedom (DOF) force/torque (F/T) sensors are usually preferred. F/T sensors assess the touch force at a single contact point.

The 6 DOF force sensors are strain gauge-based sensors measuring and outputting



forces and torques for all three Cartesian coordinates ( $x$ ,  $y$  and  $z$ ). Miniature T/F sensors are available from many manufacturers (*e.g.* ATI Industrial Automation, BL Autotec Ltd) and are offered in packagings of sizes below 2 cm both in diameter and height [56, 57]. The 6 DOF F/T sensors perform well with respect to creep, hysteresis and long time stability [58].

The TWENDY-ONE robot (Sugano Laboratory) has a four-finger-hand with 6-axis force sensors installed at each fingertip [29, 59]. With the tactile feedback, the machine is able to grip and manipulate various objects, such as a paper cup or a pencil. The new generation of dexterous hands of Light-Weight Robots (DLR) [8] are also equipped with miniature 6-component F/T sensors at the fingertips [60]. This allows controlling the grasp forces on the fingertips [61] and enables dexterous object manipulation [62].

### 2.4.3 Tactile sensors

In contrast to actuator effort sensors and F/T sensors, tactile sensors, mounted at the inside of gripper fingers and fingertips, measure directly contact of the robot with an object, or the amount of pressure applied on the touch surface. They help to detect proper gripping and slippage of objects [63], and, being often embedded in deformable elastic packagings, support grasp stability [53].

The most common, simplest, and most readily available off-the-shelf tactile sensing component is a force-sensitive resistor (FSR) [53]. An FSR consists of a polymer thick film, realized by printing conductive ink, whose resistance decreases when force is applied to its surface. Although similar in operating principle to piezoresistors, FSRs cannot be used for precise force measurements, but rather for the detection and discrimination between load cycles. Arrays of FSRs (Interlink Electronics) [64], and their equivalents, Flexiforce sensors (Tekscan) [65], are available on flexible polymer substrates. The finger prosthesis i-limb digits (Touch Bionics) [10] uses FSRs to sense pressure from a remnant digit, and control the “open” and “close” operation of the prosthetic hand.

Commercial pressure sensors (*e.g.* from Honeywell) can also be used for touch-sensing applications [66]. The bionic hand of Shadow Robot Company [54] uses pressure-sensor-based tactile transducers BioTac (SynTouch) [67]. A robotic finger equipped with BioTac outperforms human touch, discriminating between 117 different textures with an accuracy of 95% [68].

### 2.4.4 Commercial sensors summary

The interest in tactile sensing has shifted away from the industrial arena, and it may be surprising to find so little tactile sensing applied in industrial robotics and automation, considering these domains as a major area of application [69]. Very few industrial or commercial tactile sensing devices are available, and even less are in regular application in industry.

The few existing commercial devices are bulky and rigid, they lack flexibility and large-area expendability. Actuator effort sensors provide rough feedback for grip estimation only. The F/T sensors, which allow 3-axial force measurements, are bulky and limited to sampling data from local contact points. The existing tactile sensor arrays, which are flexible and perform over a large area, are restricted to uni-axial force measurements. To the best of my knowledge, none of the currently available commercial products is able to measure both normal and shear contact forces at the arbitrarily-shaped large-area surfaces of robotic and prosthetic bodies.

## 2.5 Microfabricated force sensors

The realization and application of microfabricated force sensors is well documented in literature [22, 41, 42, 58, 70–74]. Technological advances in microfabrication have already provided small and thin sensors, characterized by a high spatial resolution of sensing cells. A variety of applications deals with sensor arrays that can accurately sense texture [44, 45], evaluate fine touch over large skin-like areas [75–79], measure hand forces [80–85], forces in orthodontia [86, 87], or in upper [88] and lower prosthetic limbs [89–91], forces of end-effectors in minimally invasive surgeries [92–97], or plantar pressure in humanoid robots [49], to name a few.

This section focuses on *micrometer-scaled* single tactile sensors and tactile sensor arrays, which are fairly close to what we imagine by an artificial skin, as they can be custom-designed for 3D force detection schemes and deposited on thin flexible substrates. Various *uni-axial* and *three-axial* micromachined force sensors are reviewed from the recent literature, including piezoresistive, strain-gauge, piezoelectric, conductive polymer, optical, magnetic and transistor-based systems. In this thesis, particular focus is shifted to *flexible substrate*-based force sensors and *capacitive force sensors*. A broader review of literature on micromachined force sensors is available in the table 2.1 and various review papers [22, 41, 42, 58, 73, 74].

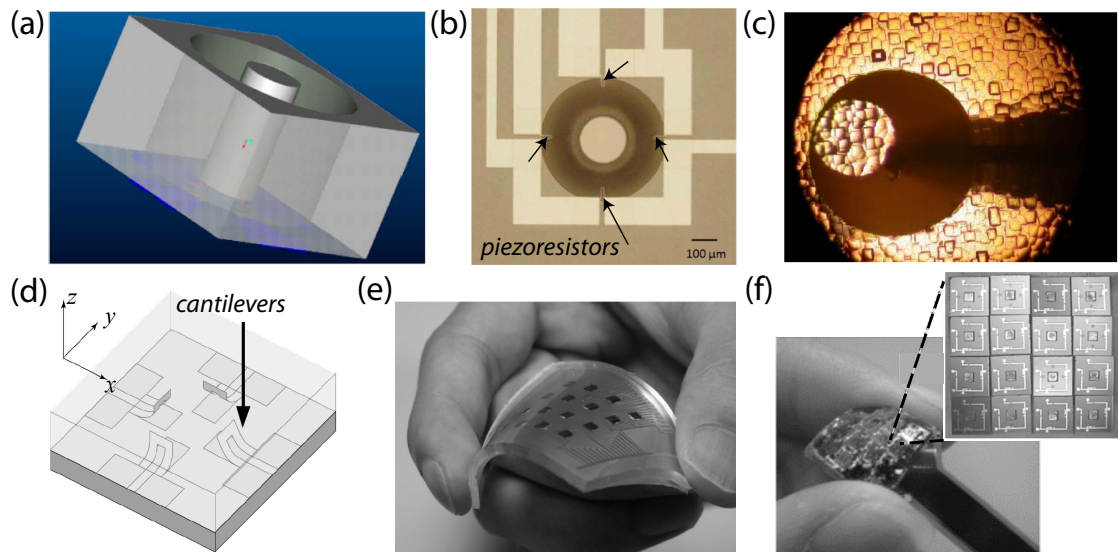


Figure 2.4: Piezoresistive tactile sensors. (a-c) The piezoresistive hair-like sensor by [92]: (a) schematic 3D illustration of a silicon post embedded on a PI diaphragm, (b) top view of the fabricated structure, and (c) top view photograph of the post being pushed by a microneedle and stopped by the cylindrical wall, © 2010 IEEE. (d) Concept of a cantilever-based tactile sensor, reprinted from [99], and (e) photograph of piezoresistive cantilever chips embedded in a flexible rubber [100], © 2009 IEEE. (f) Image of a semi-flexible piezoresistive tactile sensor array, embedded in PDMS and wired on the FPCB, reprinted from [101], © 2006 IOP Publishing.

### 2.5.1 Micromachined piezoresistive sensors

Piezoresistive sensors function upon the piezoresistive effect, which causes change in electrical resistance under an applied strain and deformation. The resistance value is determined by both the bulk resistivity and by the dimensions. Consequently, there are two ways by which the resistance value can change in response to an applied strain – the dimensions (length and cross section), and the resistivity, which can change as a function of strain for certain materials (*e.g.* doped silicon, ceramics). Piezoresistors are resistors whose resistivity changes with applied strain [98].

Silicon (Si)-based batch-fabricated piezoresistive force sensors have been well reported in the literature [81, 92, 99, 101–107]. Kane *et al.* composed an array of piezoresistive stress sensing elements, constructed with a fully complementary metal–oxide–semiconductor (CMOS)-compatible fabrication process, allowing the integration of the sensing structures with digital control circuitry [102]. The sensors demonstrated a linear response to applied normal stress up to 35 kPa. Bartsch *et al.* developed a miniaturized multi-axis piezoresistive force sensor, with which they estimated the 3D GRFs of a running cockroach [106]. Although these Si-based force sensors offered the

possibility for miniaturization, they were not useful as tactile imagers, because of their hard and bulky packaging and lack of force-overload protection.

In order to overcome the technological incompatibility between piezoresistive materials and polymeric films<sup>b</sup>, and to create semi-flexible sensors, flexible membranes were used by some research groups as a connecting material between Si-diaphragm sensors [81, 92]. Others mounted Si-dies on flexible substrates using a conductive epoxy glue [101, 104, 108]. Silicon piezoresistive force sensors packaged in flexible polyimide (PI) were proposed by Beebe *et al.* [81]. Hybrid piezoresistive tactile sensors composed of both rigid Si posts and a flexible PI diaphragm, mimicking a hair-like structure, have been reported by Hu *et al.* [92] (figure 2.4a-c). They revealed an improved durability and resistance to excessive load and were able to measure 3D forces up to 3 mN. Similar piezoresistive sensors have been glued as Si-dies on a flexible printed circuit board (FPCB) [101], Kapton<sup>®</sup> [104] and polyurethane [108] substrates. Nevertheless, the large-area expandability of these sensors was limited due to the design of the sensing cells, intended for force-sensing at a contact point, not pressure-sensing over a large surface.

For large-area pressure-sensing applications, cantilever-based piezoresistive sensors were demonstrated in elastic silicone rubber packagings [99, 100, 105] (figure 2.4d, e). Sohgawa *et al.* demonstrated a tactile array sensor with 3×3 piezoresistive micro-cantilevers for 3D force measurements [99]. The Si-dies bearing the cantilevers were embedded in polydimethylsiloxane (PDMS) for protection and transfer of surface-applied stress to the cantilevers. The sensor measured normal and shear loads up to 130 kPa and 25 kPa, respectively. Kim *et al.* developed a 3D force sensor matrix using rigid Si micromachining and packaging technologies of the FPCB with PDMS [101] (figure 2.4f). The resulting device was a semi-flexible tactile sensor array containing 4×4 piezoresistive chips, providing sensitivity of 2.1% /N and 0.5% /N, for normal and shear force, respectively.

Exploiting the piezoresistive behavior of a carbon fiber (CF), Park *et al.* proposed a tactile sensor replacing Si-based piezoresistors with CFs [109]. Such an approach allowed depositing the sensing elements on elastomeric polymer surfaces.

Micro-machined piezoresistive tactile sensors offer 3D force sensing, a high spatial resolution, high stress sensitivity, and direct integration with signal-processing electronics. However, these sensors expose limited flexibility and poor large-area expandability due to a Si-based packaging of the sensing cells, and are therefore not suitable for tactile sensing skin-like applications.

---

<sup>b</sup>*i.e.*, polymers cannot withstand the high temperatures of silicon doping processes

### 2.5.2 Micromachined strain gauge-based sensors

Strain gauges are metal resistors that change their resistance in response to strain and due to the shape deformation mechanism. The magnitude of resistance change stemming from this principle is much smaller than what is achievable from the stress-induced resistivity change in piezoresistors. Typical strain gauge patterns are zigzagged conductor paths that effectively increase the length of the resistor and the amount of total resistance under a given area [98]. Since strain gauges are metal-based, they can be deposited and processed under temperatures much lower than what is needed for doping processes for silicon piezoresistors. Therefore, strain-gauge force sensors are compatible with polymeric substrates, which endows them with mechanical flexibility over a large-area sensory surface.

Various force sensors reported in literature have been deposited onto flexible polymeric substrates [49, 83, 110–113]. Engel *et al.* demonstrated a  $10 \times 10$  array of nickel-chrome (NiCr) alloy strain gauges embedded in flexible membrane-like structured polyimide (PI) substrate [83]. Such uni-axial force sensors, complemented with other gauges, were used for temperature, thermal conductivity, surface contour and hardness sensing over the large surface area of a flexible skin [110]. Park *et al.* embedded microchannels of conductive eutectic gallium-indium liquid in silicone rubber. This microdevice served as a hyper-deformable pressure-sensitive strain gauge [113].

Strain gauge technology is easily integrated in a 3D force detection scheme. Hwang *et al.* developed a deployable PI-based strain-gauge tactile matrix operating up to 40 kPa [49]. Four copper (Cu)-Ni strain gauges were embedded in a ductile substrate below a stress-distributing bump structure (figure 2.5a-c). The reported sensitivities of the force sensing array were 7.5 mV/N in normal direction and 0.6 mV/N in shear. Although the sensor allowed 3-axial force measurement, the discrimination between shear and normal force signals was difficult. Similar designs (figure 2.5d) of 3D load-sensing tactile sensors involved the structuring of the flexible polymeric substrate into thin membranes, by which their force sensitivity was increased to 200 mV/N and 70 mV/N, for normal and shear forces, respectively [111, 112]. The force range of these force sensors was relatively small ( $<1$  N). Carbon nanotubes (CNTs) vary their resistance upon application of a load, and therefore offer an alternative to metal strain gauges. Distributed over elastic rubber surfaces, CNTs proposed by Su *et al.* can serve for similar type of sensors with high normal and shear force sensitivity [114].

Strain gauges provide large-area expandable, flexible substrate-based 3D force sensing solutions, with well established, simple and cheap fabrication techniques. Nevertheless, due to low piezoresistive gauge factors, such sensors exhibit a relatively low sensitivity, when compared to piezoresistive, piezoelectric or capacitive solutions.

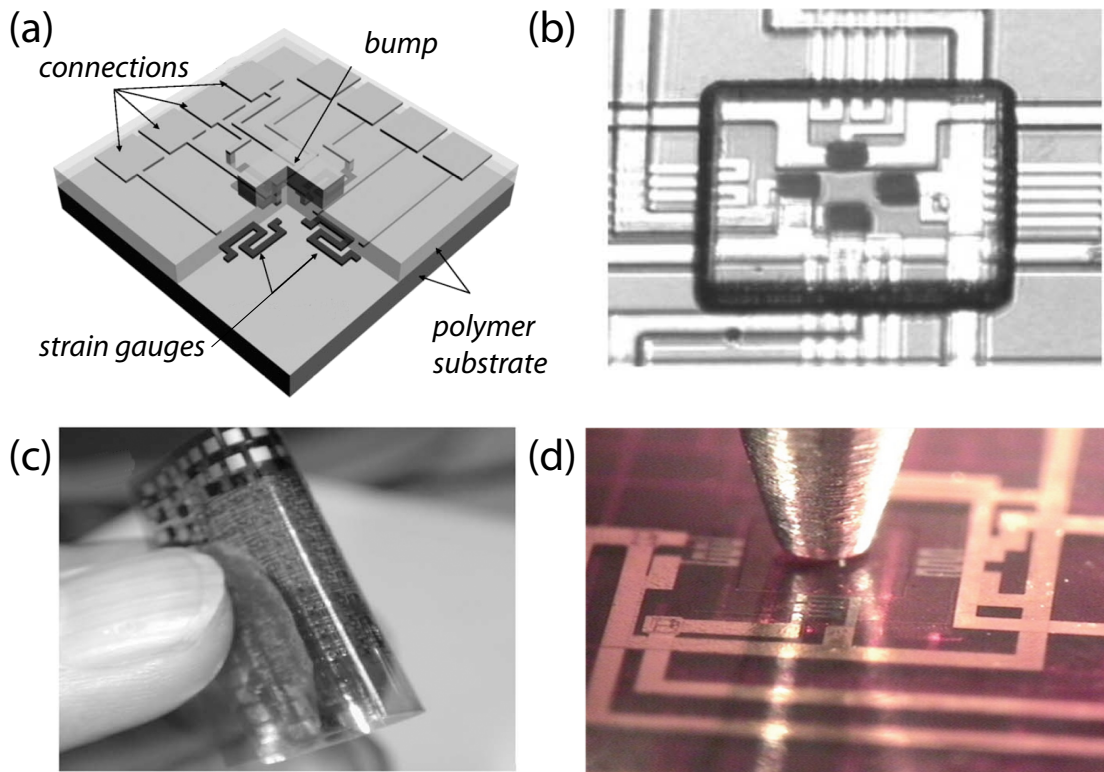


Figure 2.5: Strain gauge-based tactile sensors. (a-c) The tactile sensor by [49]: (a) schematic view of the sensor, (b) top view of the fabricated structure, (c) demonstration of the flexibility of the sensor matrix, © 2008 IEEE. (d) The four strain gauges of a tactile sensor by [111] under a load applied by the measurement setup, with permission of Springer.

### 2.5.3 Micromachined piezoelectric sensors

Piezoelectric sensors convert an applied mechanical stress or force into electrical charge that accumulates in a piezoelectric material [115]. They are highly stress-sensitive, providing large voltage outputs in response to even small deformations.

Common piezoelectric materials include crystals and ceramics, which are, however, not compatible with flexible substrates due to their high sintering temperature. Certain polymers exhibit strong piezoelectricity, *e.g.* a mechanically flexible polyvinylidene fluoride (PVDF), which has been used as a pressure-sensitive film in tactile sensor matrices for object imaging [116]. Recently, Chang *et al.* demonstrated zinc oxide (ZnO) nanorods deposited on a flexible PI substrate as an effective piezoelectric material [117].

Dahiya *et al.* used piezoelectric PVDF-trifluoroethylene (TrFE) copolymer for the construction of a piezoelectric polymer oxide semiconductor field effect transistor

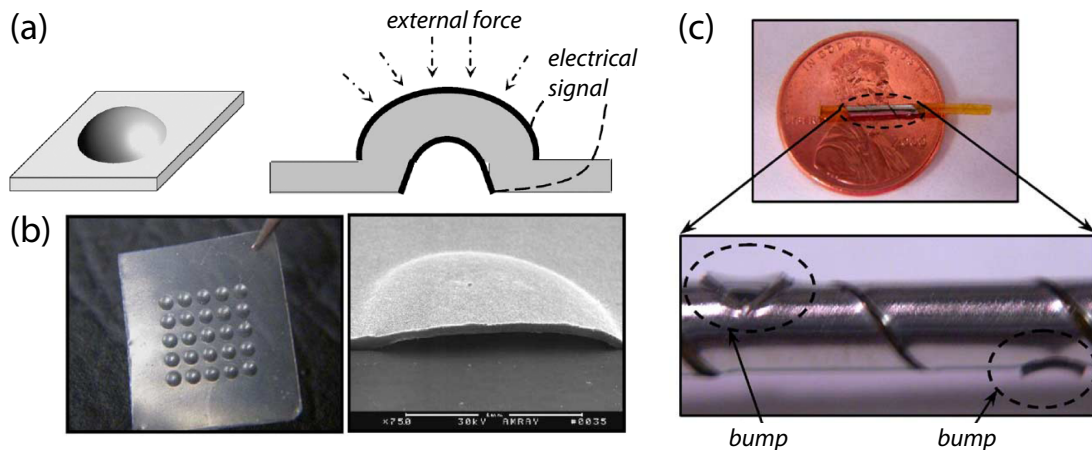


Figure 2.6: The piezoelectric tactile sensor by [119]. (a) Schematics of the dome-shaped sensor. (b) Cross-section micrograph of the micromachined PVDF-TrFE dome. (c) Photograph of the assembled flexible tactile sensors on a tube. © 2008 IEEE.

(POSFET) touch-sensitive device [118], designed as a metal–oxide–semiconductor (MOS) with a piezoelectric polymer film on the gate area. When a force was applied, the charge developed on the piezoelectric film modulated the charge in the induced channel of the MOS device. Although the device responded with a high sensitivity of 49 mV/N to the applied dynamic sinusoidal normal force, it was a rigid silicon chip structure.

Li *et al.* fabricated flexible piezoelectric PVDF-TrFE copolymers shaped in tiny domes and bumps, and characterized them as sensing components for tactile sensors [119] (figure 2.6). These films were assembled along flexible tubes and achieved a pressure-sensitivity of 10.6 mV/N, yet, similarly to [118], responded only to dynamic loads.

Piezoelectric sensors are especially suitable for detecting dynamic forces, since the electrical charge accumulated in the piezoelectric material decreases over time. This limitation disfavors the use of piezoelectric sensors for truly static measurements in artificial skin applications, unless static load detection is compensated by other type of detectors [120].

### 2.5.4 Micromachined conductive polymer sensors

Polymers offer mechanical flexibility, robustness, large-area low-cost fabrication techniques, and, in case of elastomers, fantastic stretchability characteristics. In recent years, various technologies have been developed [121] to benefit from the advantages of conductive polymers for tactile sensing applications. The conductive polymeric films commonly used as pressure-sensitive materials are pressure-conductive rub-

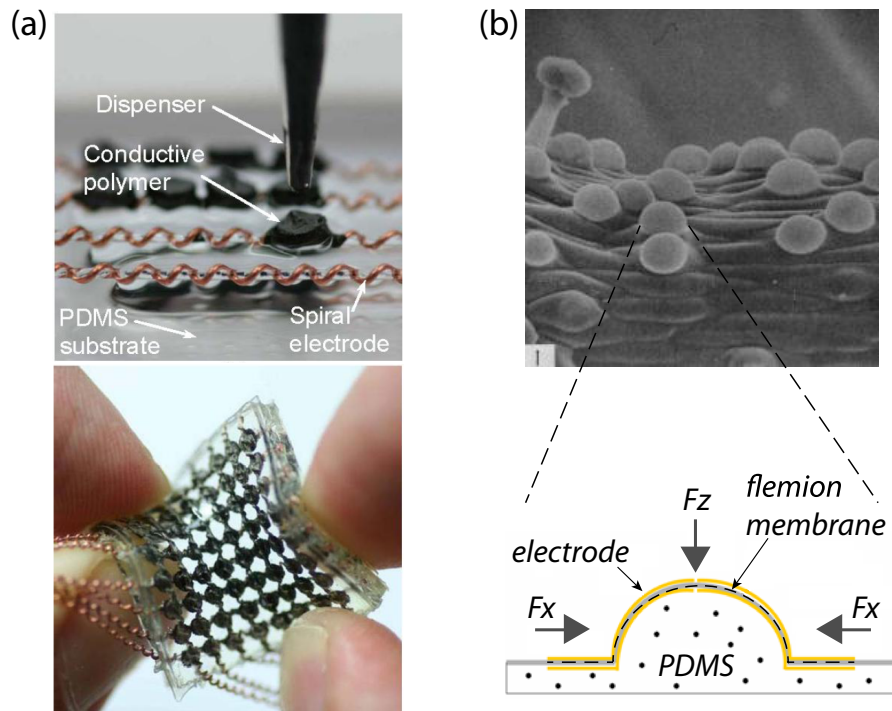


Figure 2.7: Micromachined conductive polymer sensors. (a) The process of dispensing PCR onto the electrodes of a touch sensor by [123], and the fabricated sensor array under bending conditions, © 2009 IEEE. (b) Top: tendril of a plant showing tactile receptors, bottom: cross-section view of a bioinspired, flemion-based sensor, adapted from [122], with permission of American Institute of Physics.

bers (PCRs) and ionic polymer metal composites (IPMCs). PCRs are elastomers with homogeneously dispersed conductive particles. In the absence of external forces, a PCR behaves as an insulator, but with external force applied, the particles come into contact with each other allowing current to flow. IPMC is a class of materials, in which, under an applied force, surface charges are accumulated on the electrode, as a result of a nonuniform distribution of cations inside the membrane [122]. IPMCs are composed of an ionic polymer film, solvent, and surface electrodes.

In 1993 Bell Laboratories introduced a tactile 2D shear sensor which involved a Ni microparticle-based PCR [124]. Another PCR, based on PDMS and nanoparticles of carbon black and silver, and Cu powder microparticles, was used by Cheng *et al.* to create a tactile sensing array of embedded flexible spiral electrodes [123]. Two spiral metal wires were aligned perpendicularly with a PCR inbetween (figure 2.7a). When applying pressure, the conductive polymer deformed, decreasing the resistance between the metal wires. The sensor matrix was highly flexible and operated up to 650 kPa of applied normal force. Integrated with transistors, PCRs have also been used to form flexible touch-sensitive sensor matrices [75, 76, 78].



Wang *et al.* introduced a novel 3D force sensor structure, similar to the biological receptors in plants for sensing touch [122] (figure 2.7b). An ionic polymer, flemion, was used to create a 3D force-sensitive IPMC with a dome-shaped design. The sensor responded to forces up to 0.4 N with the sensitivities of 17 mV/N and 8 mV/N, for normal and shear force, respectively. Nevertheless, the lifetime of the tactile sensor was limited to two weeks, due to evaporation of solvent from the flemion membrane. Porous nylon with electro-active dopants has also been proven conductive and exhibits prominent piezoresistive effects. Yu *et al.* deposited patterns of porous nylon filled with polypyrrole above a flexible PI substrate and obtained a pressure-sensitive material [125]. The resulting sensitivity of the flexible 1D force tactile sensor array with such composite was 0.1% /kPa in the 0-30 kPa range.

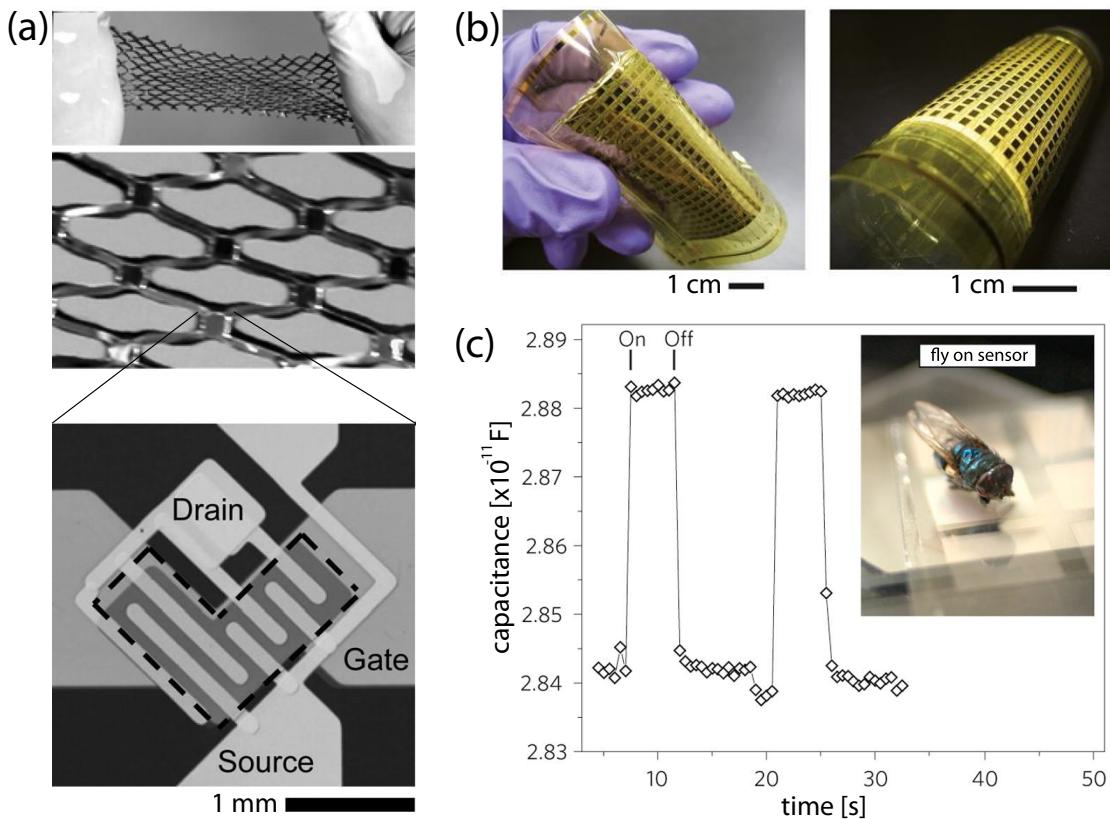
Nowadays, soft polymer-based sensors have become popular [121] and replace rigid silicon chips. However, flexible conductive polymer force sensors have not yet drawn adequate attention, being rarely reported in literature. Conductive polymer films and elastomer composites bring prospective approaches for skin-like touch sensors, since they are large-area-expandable and soft, mimicking human skin.

### 2.5.5 Transistor-based sensors

Transistors are semiconductor devices used to amplify and switch electric current between a source and drain terminals. Field-effect transistors (FETs) are transistors that use an electric field to control the conductivity of an active source-drain channel. Organic field-effect transistors (OFETs) use an organic semiconductor in its channel instead of a silicon semiconductor. Unlike typical FETs, where the semiconductor material is the substrate as well, thin-film transistors (TFTs) are deposited over a supporting substrate. Technologies of FETs [126], nanowire (NW)-based FETs [78], OFETs [75–77, 127, 128], carbon nanotube-based organic transistors [129], TFTs [130, 131], organic thin-film transistors (OTFTs) [132] or POSFETs [118, 133, 134] show genuine promising concepts for the artificial reconstruction of human touch sense.

Rigid Si-based three-axial force sensors exploiting the shear piezoresistive effect in FETs have already been constructed with a fully complementary CMOS-compatible fabrication process, allowing the integration of the sensing element with circuitry and data processing [126]. Moreover, active transistor elements have been integrated with flexible polymeric substrates and have been used for pressure sensing in pioneering works [75–78, 129].

Someya *et al.* developed a large-area pressure sensor matrix based on OFET technology [75]. The organic transistors were deposited on a flexible polyethylene naphthalate



superior flexibility (figure 2.8b), including its integrated electronics, a high sensitivity of  $30 \mu\text{A}/\text{kPa}$ , and functionality in the 2-15 kPa range.

Thin flexible microstructured rubber films have also been successfully demonstrated as the dielectric layer of an OFET in the work of Mannsfeld *et al.* [77]. A new type of OFET pressure-sensing device was developed, by integrating the compressible rubber between the single-crystal source-drain channel and a gate of the transistor, making the device highly pressure-sensitive. In particular, unlike [78, 130, 135], the sensor exhibited high sensitivity of  $\sim 3 \mu\text{A}/\text{kPa}$  in the low-pressure regime of  $< 2 \text{ kPa}$ , and a lower detection limit of 3 Pa, corresponding to a pressure induced by a sitting fly (figure 2.8c).

Moreover, cellular propylene films exhibiting piezoelectric properties (ferroelectrets) have been used in combination with TFTs for flexible pressure-sensing circuits [130, 135]. Graz *et al.* laminated ferroelectric films with transistors fabricated on flexible PI substrates, to generate an electric field under an applied pressure and to modulate the conductance of the source-drain channel of a TFT, forming pressure-sensitive transducer arrays [130].

Organic semiconductors offer numerous advantages for sensor development: mechanical flexibility, large-area expandability, low cost and relative ease of fabrication. The low mobility of organic semiconductors is acceptable for most large-area sensor applications [76], otherwise alternative materials can be used [77, 78, 129, 130, 135]. Transistor matrix technologies embedded in flexible and stretchable polymeric substrates are currently the most promising concepts of artificial skin, including stretchable electronic circuitry [129, 131, 132], but they only address the detection of uni-axial force.

### 2.5.6 Micromachined optical sensors

The large number of taxels in the matrix of an artificial skin imposes issues of complex wiring and electrical cross-talk [41]. Optical components, such as optical fibers, light-emitting diodes, photodiodes, lasers and charge-coupled device detectors are one solution to carry and detect signals eliminating these problems.

Flexible plastic optical fibers (POFs) [136] can be bent into arbitrary shapes and buried in elastomeric substrates. Heo *et al.* demonstrated crossed POFs embedded in a silicone rubber as a tactile sensor, when combined with microbending optical fiber sensors [137]. The (micro)bending of the optical fiber caused a loss of transmitted light and thus allowed detecting the forces applied to a joint up to 15 N. Similar designs of POF-crossing joints were integrated into woven textiles [138].

Kim *et al.* synthesized custom soft polymers with different refractive indices for light transmission in a transparent and flexible force sensor array [139]. The sensor measured contact forces based on the change of light intensity due to scattering at the contact area. The device responded to a uni-axial load of 19 N by a light intensity reduction from 100% to 5%.

Missinne *et al.* reported a tactile shear-stress sensor based on a surface-emitting laser and a photodiode facing each other and separated by a deformable PDMS layer [140]. The sensor sensed shear force up to 5.5 N, however its usability was limited to a small detection area, since the signal circuitry was complex and required bulky packaging.

Optical tactile sensors require expensive systems such as cameras, optical sources and detectors, which enlarge the total package size even if the sensor is small. Moreover, bending or flexing of the sensor often induces errors, making the optical sensors not readily fit for compliant skin-like touch sensors.

### 2.5.7 Micromachined magnetic and inductive sensors

Magnetic sensors measure the change in magnetic flux density as a result of the applied force. The flux measurement is usually conducted with Hall-effect devices or magnetoresistive detectors [22]. Although micromachined electromagnetic transducers have already been utilized in haptics for vibro-tactile displays [141, 142], or for relief and profile imaging of magnetic mediums [143, 144], very little has been reported in literature about micro-scaled magnetism-based force sensors.

A small magnetic rod-joystick has been proposed in combination with magnetoresistive detectors as a device sensitive to 3-axial forces [145]. However, a miniaturization of the sensor for skin-like applications was not possible, mainly due to the design and because, to date, thin ferrite films are not processable with micro-technological methods [146]. Nevertheless, integrated into flexible substrates, miniaturized planar coils [147] and 3D microcoils [148, 149] have still potential in force sensing applications.

Futai *et al.* demonstrated a planar spiral inductor embedded in a rubber as a tactile force-sensing element [84]. Distributed in a soft body, coils changed their shape when a force was applied, detecting the contact of external objects. However, the inductance values of the coils showed a relatively weak variation as a function of force. Moreover, the proximity between the inductor and the object touching the sensor produced parasitic capacitance between them, inducing unwanted self-resonance that interfered with the resonant measurement circuit.

Inductive and magnetism-based sensors suffer from electric and magnetic fields interference, and are limited to nonmagnetic mediums in their proximity, therefore

their application in skin-like force sensors remains unexplored and challenging.

### 2.5.8 Micromachined capacitive sensors

Capacitive sensors measure the force-induced change in capacitance between conductors separated by a dielectric [150]. Most capacitive sensors have a parallel-plate geometry, and the capacitance value depends on the surface of the electrode plates, the distance between them, and the dielectric constant of the medium in-between the plates. Therefore, to change the value of capacitance  $C = \epsilon_0 \epsilon A / h$ , one can either change the electrode overlap area  $A$ , the electrode spacing  $h$ , or, one can vary the dielectric constant  $\epsilon$  of the medium between the plates (with  $\epsilon_0$  being the vacuum permittivity). Most capacitive sensors rely upon the change of the distance between the plates rather than the change in surface [151], with the dielectric constant being found the rarest varied-parameter<sup>c</sup>.

In 1984, Bell Laboratories reported a robotic capacitive touch sensor array, a semi-flexible three-layer sandwich structure, with electrodes printed on an FPCB [153]. Similar normal force capacitive sensors were fabricated with the use of silicon technology [154], while 1D-shear and normal force sensors were demonstrated with the use of rubber-encapsulated FPCBs [155]. Three-axial force sensors were developed based on rigid Si and glass substrates [156]. In 1995, Chase and Ren proposed the first design of a flexible capacitive tactile sensor for both normal and shear force detection [157]. The parallel-plate capacitive sensor consisted of four bottom electrodes and a single top electrode, separated by a flexible compressive dielectric, deformable under an applied load.

Recently, rigid Si-based capacitive 3D tactile sensors were developed [158] and integrated with CMOS technology [159], merging the sensing structures with digital control circuitry. Micromachined flexible capacitive transducers have been developed for tactile displays and touch screen applications [160, 161], for the measurement of forces in medical devices [86, 95], or to determine *in-vivo* tissue elasticity [96, 97], to mention a few.

A stretchable capacitive 1D force sensor was demonstrated by Cotton *et al.* using gold (Au) films embedded in a silicone rubber [85]. Mannsfeld *et al.* demonstrated highly flexible polymeric substrates fabricated over large areas by microstructuring of thin PDMS films [77] (figure 2.9a). These microstructured rubbers were highly compressible, exhibiting elastic deformation when pressure was applied, and minimizing the problems associated with visco-elastic creep behaviour of the polymers [162]. When

---

<sup>c</sup>for some elastomers, change in permittivity can result from their deformation [86, 152]

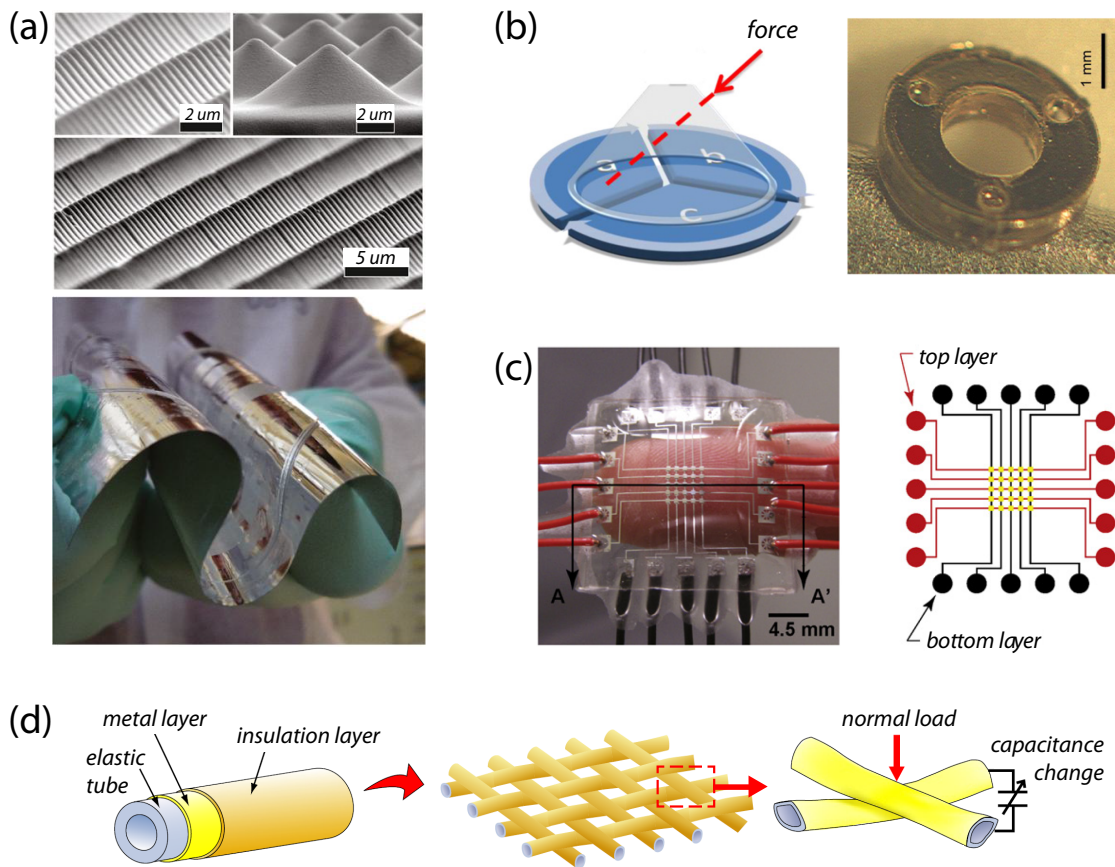


Figure 2.9: Capacitive force sensors. (a) Micrographs of pressure-sensitive microstructured PDMS films and a film molded on a flexible substrate [77], with permission of Nature Publishing Group. (b) Schematic illustration of the 3-axial tip-contact force sensing transducer and a photograph of the device [95], © 2008 IOP Publishing. (c) PDMS-based normal force sensor and microfluidic wire paths [163], with permission of Elsevier. (d) Schematic view and operation principle of a fabric tactile sensor [164], © 2008 IOP Publishing.

employed as capacitor dielectric, the capacitive sensors demonstrated superior sensitivity and response times in the millisecond range. Although flexible and stretchable, these sensors were exclusively responding to applied uni-axial force.

Sundara-Rajan *et al.* demonstrated a 3D force sensing cell operating up to 2 MPa in normal and 220 kPa in shear direction, with sensitivities of 0.04% /kPa and 0.025% /kPa, respectively [91]. Nevertheless, the single 10×10 mm<sup>2</sup> taxel, composed of a PCB and PDMS pillars, was rigid, thick (>4 mm) and bulky, with a low capacitance value per unit surface (~2.5 pF/cm<sup>2</sup>). Lu *et al.* reported a capacitive transducer for sensing 3-axial contact forces on a tip of a small-diameter tubular medical device [95] (figure 2.9b). Three proof mass blocks were connected with a tip to which a 3-axial force was

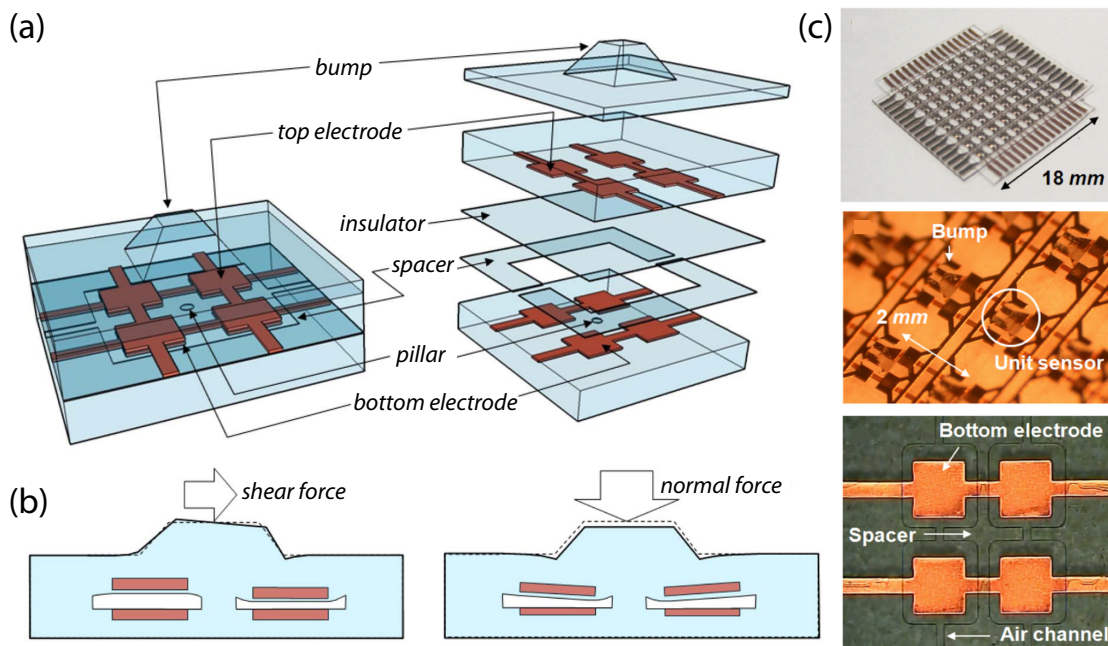


Figure 2.10: The flexible capacitive 3-axial force sensor by Lee *et al.* [79, 165–167]. (a) Schematic view of the tactile cell [165], © 2008 IEEE. (b) Principle of operation to measure normal and shear stress [165], © 2008 IEEE. (c) Photographs of the 3D tactile sensors [79], © 2011 IOP Publishing.

applied, moving them towards or away from the bottom capacitive electrode plate. However, large area expandability of the device was limited, as its design was oriented for the measurement of contact forces applied locally and on a small surface only.

Lee *et al.* developed a fully flexible PDMS-based capacitive tactile array capable of measuring 3-axial forces up to 131 kPa [165–167] (figure 2.10). The proposed structure was a smart combination of those previously reported in the literature [81, 153, 154, 156]. A tactile cell consisted of four capacitors arranged in a square by an array of crossing electrodes [153], which were measured differentially [156]. The electrodes were separated by an air gap-spacer [154, 156]. A protruded bump [81, 156] was placed on the top of the sensing cell to transfer the 3D loads into the electrodes underneath. The reported sensitivity of the sensor was  $2.3 \cdot 10^{-4} \text{ kPa}^{-1}$  in the normal direction and  $2 \cdot 10^{-4} \text{ kPa}^{-1}$  when applying shear loads. An improved design permitted to act in the 0-250 kPa range with a real-time measurement sensitivity of  $\sim 10^{-4} \text{ kPa}^{-1}$  [79]. The absolute capacitance value per unit surface of a sensing cluster was high ( $\sim 25 \text{ pF/cm}^2$ ). This device remains today probably the most advanced, fully flexible 3D force sensor array. However, due to a complicated multilayer bonding process, extension of the sensory matrix to a large-area artificial skin is complicated.

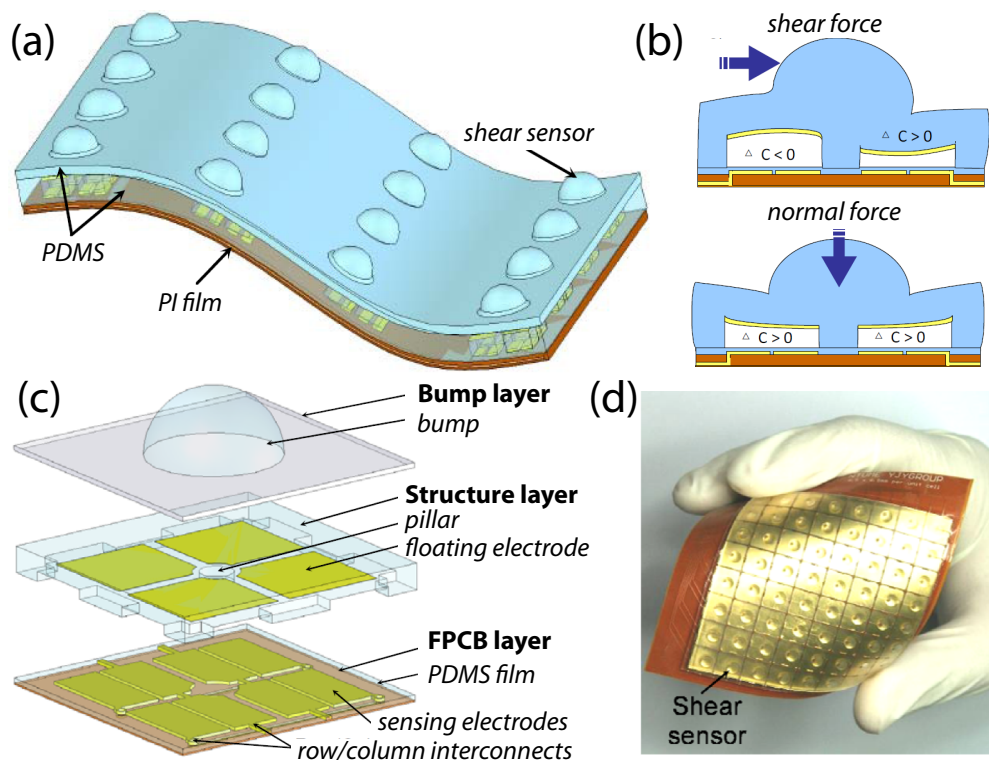


Figure 2.11: The flexible capacitive 3-axial force sensor by Cheng *et al.* [169], © 2010 MDPI Publishing. (a) Schematic of the artificial skin. (b) Principle of operation to measure normal and shear stress. (c) Exploded drawing of the tactile cell. (d) Photograph of the flexible tactile sensing array.

Cheng *et al.* used an FPCB-PDMS-based capacitive sensing array for pressure measurements [168]. The sensor design exploited the use of a floating electrode, reducing the complexity of the electrical circuitry, and increasing the sensor's durability and its resistance to deformation. However, compared to other designs [156, 165–167], the floating electrode approach yielded lower capacitance values. An improved version of the sensor array (figure 2.11) was capable of measuring both normal and shear forces and was equipped with a grounded shield to effectively minimize the capacitance noise level and enhance the signal-to-noise ratio of the sensing elements [169]. The 3D force sensitivity of the device was up to 0.95% /mN and 1.67% /mN, in normal and shear direction, respectively. Yet, the absolute initial capacitance per unit surface of a sensing cluster was quite low<sup>d</sup> (~713 fF/cm<sup>2</sup>).

Surapaneni *et al.* proposed polymer-based normal and shear sensing clusters of fingered capacitive sensors [170]. The initial measurements suggested an operation of

<sup>d</sup>herewith as large as ~130 pF/cm<sup>2</sup> (sensor reported in chapter 3) and ~23 pF/cm<sup>2</sup> (sensor reported in chapter 4)



up to 120 kPa normal and 60 kPa shear pressures, with a sensitivity of  $4.4 \cdot 10^{-4} \text{ kPa}^{-1}$  and  $7.6 \cdot 10^{-4} \text{ kPa}^{-1}$ , respectively. However, a systematic study that discusses capacitor read-outs in a comprehensive way, takes into account measurement errors, and investigates the sensor behavior during unloading and multiple loading cycles, has not been presented so far. Also the absolute capacitance per unit surface of a sensing cluster was rather small ( $\sim 1.4 \text{ pF/cm}^2$ ).

A similar design by the same authors [171] addressed the problem of reliable interconnects [18] for flexible capacitive force sensors. PDMS-embedded Au electrodes were complemented with liquid metal filled-microchannels to self-repair eventually broken Au connections upon exerted load.

Similarly to references [113, 171], Wong *et al.* embedded microchannels of conductive eutectic gallium-indium-tin alloy liquid in PDMS rubber [163] (figure 2.9c). The metal-filled microfluidic channels served as the capacitive plates and conductive interconnects of a hyperelastic pressure-sensitive capacitive sensor. However, due to the liquid nature of the conductive medium used, the force from the applied load on the sensor was unintentionally transmitted to the complete matrix, causing unloaded taxels being responsive.

An alternative approach to meet the essential requirement of flexibility was achieved by incorporation of sensory structures into a textile [164, 172]. Hasegawa *et al.* reported a fabric capacitive tactile sensor for the detection of a normal force [164] (figure 2.9d), and the combination of both normal and lateral forces [172]. Thin metallic wires were cross-plaited into a cotton yarn forming a cloth. When a load was exerted, the fibers deformed elastically changing the capacitance between the wires.

Capacitance-sensing schemes offer numerous advantages for the development of flexible skin-like sensors. Miniaturized capacitors can be readily placed, with high spatial resolution, on flexible, stretchable, and large-area expandable polymer materials [77, 79, 85, 163, 165–171]. Three-axial force sensing can be obtained with relatively simple designs [79, 91, 95, 165–167, 169–171], offering a high sensitivity to 3D loads. Capacitive matrix technologies embedded in flexible and stretchable polymeric substrates show promising concepts of artificial skin, although they require relatively complex read-out circuitry.

### 2.5.9 A comparison of micromachined sensor solutions and sensing techniques

Table 2.1 summarizes the above reviewed tactile sensor solutions, many of which fulfil the functional specifications of the skin-like force sensors. While piezoresistive [81, 92, 99–109], piezoelectric [118–120, 133, 134], inductive [84], optical [137–140], and conductive polymer principles [75, 76, 78, 122, 123, 125] can be found in microscale force sensing systems, the predominant and most advanced read-out schemes integrated into *flexible substrates* are strain-gauge- [49, 83, 110–114], transistor- [75–78, 127–132, 135] and capacitance-based [77, 79, 85, 160, 163, 165–172] sensors. The usual compliant film substrates and materials used for these sensors were Kapton<sup>®</sup> [168, 169], Mylar<sup>™</sup> [127, 128], PEN [75], PET [77], Parylene-C [132, 164, 170, 172], silicone rubbers [49, 75–77, 79, 85, 113, 114, 122, 123, 129–132, 163–165, 165–169, 171], and PI [49, 76, 78, 83, 110–112, 125, 131, 135, 170], the latter being commonly used as a dielectric interlayer in integrated circuits (ICs) [173] or a flexible package material for sensors [174].

Observations on the general advantages and disadvantages of the different sensing principles are presented in table 2.2. In this thesis, the capacitive approach was preferred due to numerous assets [151]: capacitive sensors have a high sensitivity, a good temperature performance, and a low power consumption, a feature that is especially essential for an autonomous portable application of an artificial skin.

A further review of literature on force sensors not discussed in this thesis is available in [14, 22, 41, 42, 53, 58, 69, 73, 74].

Table 2.1: Comparison of the micromachined 3-axial and uni-axial (flexible and non-flexible) force sensors, as selected from literature.

author	date	ref.	sensor type	force/pressure sensitivity <sup>a</sup>		force/pressure range <sup>a</sup>		flexibility	flexible materials
				normal	shear	normal	shear		
Kane	2000	[102]	piezo-resistive	1.59 mV/kPa	0.32 mV/kPa	35 kPa	60 kPa	no	-
Tseng	2004	[86]	capacitive	269 fF/kPa	-	50 mN	-	no	-
So-meya	2004	[75]	transistor, cond.polymer	0.2 $\mu$ A/kPa	-	30 kPa	-	yes	PEN, PDMS
Ruther	2005	[103]	piezo-resistive	430 mV/N	430 mV/N	0.6 N	0.6 N	no	-

## 2.5. Microfabricated force sensors

Table 2.1 – continued from previous page

author	date	ref.	sensor type	sensitivity <sup>a</sup>		range <sup>a</sup>		flexi- -bility	ma- -terials
				normal	shear	normal	shear		
Beccai	2005	[104]	piezo- resistive	3.2% /N	3.23% /N	2 N	2 N	rigid Si on FPCB	-
Graz	2006	[130]	tran- sistor	0.0008 $\mu$ A/kPa	-	800 kPa	-	yes	PI
Kim	2006	[101]	piezo- resistive	2.1% /N	0.5% /N	2 N	2 N	rigid Si on FPCB	-
Noda	2006	[105]	piezo- resistive	-	0.13% /kPa	-	5 kPa	rigid Si in PDMS	-
Hwang	2007	[49]	strain gauge	7.5mV/N	0.6 mV/N	4 N, 40 kPa	1.5 N, 15 kPa	yes	PI, SU-8, PDMS
Lee	2008	[165]	capa- citive	6 fF/mN, 2.9%/mN, 0.22% /kPa	3% /mN, 0.23% /kPa	10 mN, 131 kPa	131 kPa	yes	PDMS
Hase- gawa	2008	[164]	capa- citive	1.5 fF/mN	-	350 mN	-	yes	rubber, Parylene-C
Heo	2008	[137]	optical	20 gray scale value/N	-	15 N	-	yes	PDMS, POF
Roth- maier	2008	[138]	optical	4% /N	-	30 N	-	yes	rubber, POF
Li	2008	[119]	piezo- electric	10.6 mV/N	-	1 N	-	yes	PVDF- TrFE, Parylene-C
Yu	2008	[125]	cond. poly- mer	0.1% /kPa	-	30 kPa	-	yes	PI, nylon
Dahiya	2009	[118]	piezoelectric, transistor	49 mV/N	-	5 N	-	no	-
Cotton	2009	[85]	capa- citive	0.13 fF/kPa, 0.04% /kPa	-	180 kPa	-	yes	PDMS
Graz	2009	[135]	tran- sistor	6.25 pA/kPa	-	22 MPa	-	yes	PI, propy- lene

## Chapter 2. Tactile sensing: from human skin to artificial receptors

Table 2.1 – continued from previous page

author	date ref.	sensor type	sensitivity <sup>a</sup>		range <sup>a</sup>		flexi-bility	ma-terials
			normal	shear	normal	shear		
Soh-gawa	2009 [99]	piezo-resistive	0.07 mV/kPa	0.05 mV/kPa	130 kPa	25 kPa	rigid Si in PDMS	-
Noda	2009 [100]	piezo-resistive	0.00393% /kPa	0.0485% /kPa	10 kPa	6 kPa	rigid Si in PDMS	PDMS
Wang	2009 [122]	cond. polymer	17 mV/N	8 mV/N	0.4 N	0.4 N	yes	PDMS, flemion
Cheng	2009 [123]	cond. polymer	300-500 $\Omega$ /kPa	-	650 kPa	-	yes	PDMS
Cheng	2009 [168]	capacitive	17.8 fF/kPa, 2.27% /kPa	-	5 N, 430 kPa	-	PDMS on FPCB	PDMS, Kapton <sup>®</sup>
Cheng	2010 [169]	capacitive	0.95% /mN	1.67% /mN	0.3 N	0.3 N	PDMS on FPCB	PDMS
Takei	2010 [78]	transistor, cond. polymer	11.5 $\mu$ S/kPa, 30 $\mu$ A/kPa	-	15 kPa	-	yes	PI
Mann-sfeld	2010 [77]	transistor	0.3-3 $\mu$ A/kPa	-	18 kPa	-	yes	PET, PDMS
Mann-sfeld	2010 [77]	capacitive	15-55% /kPa	-	15 kPa	-	yes	PET, PDMS
Park	2010 [113]	strain gauge	0.1-5 m $\Omega$ /kPa	-	100 kPa	-	yes	PDMS
Hu	2010 [92]	piezo-resistive	0.35% /mN	1.08% /mN	30 mN	6 mN	no	-
Choi	2010 [111]	strain gauge	207 mV/N	70 mV/N	0.8 N	0.8 N	yes	PI
Lee	2011 [79]	capacitive	1.2% /mN, 0.096% /kPa	1.3% /mN, 0.104% /kPa	20 mN, 250 kPa	250 kPa	yes	PDMS

## 2.5. Microfabricated force sensors

Table 2.1 – continued from previous page

author	date	ref.	sensor type	sensitivity <sup>a</sup>		range <sup>a</sup>		flexi- -bility	ma- -terials
				normal	shear	normal	shear		
Sura-paneni	2011	[170]	capacitive	0.044% /kPa, 0.4 fF/kPa	0.076% /kPa, 0.68 fF/kPa	120 kPa	60 kPa	yes	PI, PDMS, Parylene- C
Sura-paneni	2011	[171]	capacitive	0.074% /kPa	0.022% /kPa	60 kPa	40 kPa	yes	PDMS
Mis-sinne	2011	[140]	optical	-	350 $\mu$ A/N	-	5.5 N	semi- flexible	PDMS, PI
Kwon	2011	[112]	strain gauge	200 mV/N	70 mV/N	1N	1N	yes	PI
Lu	2011	[95]	capacitive	not re- ported	not re- ported	750 kPa	750 kPa	semi- flexible	SU-8
Sun-dara- Rajan	2012	[91]	capacitive	1 fF/kPa, 0.04% /kPa	0.025% /kPa	2 MPa	220 kPa	rigid PCB in PDMS	-
Brook-huis	2012	[158]	capacitive	16 pF/N	2.7 pF/N mm	50 N	25 N mm	no	-
Kim	2012	[139]	optical	0.25% /N	-	19 N	-	yes	custom- synthesized polymers
Wong	2012	[163]	capacitive	0.009% /mN	-	2.5 N	-	yes	PDMS
this work, chap- ter 3	2012	[175]	capacitive	0.5-1 fF/N, 50-100 aF/kPa, 0.8% /kN	-	3 kN, 30 MPa	-	yes	PI
this work, chap- ter 4	2012		capacitive	0.066- 2.4% /kPa, 15-563 fF/kPa	0.028% /kPa, 5 fF/kPa	14 N, 140 kPa	14 N, 220 kPa	yes	PI, PDMS, Parylene- C

<sup>a</sup> Unless explicitly indicated in the publication, the values were interpreted from figures or estimated from the data available in the publication.

## Chapter 2. Tactile sensing: from human skin to artificial receptors

Table 2.2: Comparison of the force-sensing principles.

SENSOR TYPE	ADVANTAGES	DISADVANTAGES
<b>piezo-resistive</b>	<ul style="list-style-type: none"> <li>• high piezoresistive gauge factors, high stress sensitivity</li> <li>• direct integration with signal-processing electronics</li> <li>• suitable for static and dynamic applications</li> <li>• 3D force sensing possible</li> </ul>	<ul style="list-style-type: none"> <li>• technology not readily compatible with polymeric substrates</li> <li>• flexibility limited to Si-based packaging</li> <li>• even if sensor small, total package size large</li> <li>• poor large-area expandability</li> <li>• packaging processes for flexibility and robustness very complex, they reduce yield</li> <li>• costly materials and fabrication techniques</li> </ul>
<b>strain gauge</b>	<ul style="list-style-type: none"> <li>• well established, simple, cheap fabrication techniques</li> <li>• can be placed on flexible polymer materials</li> <li>• 3D force sensing possible</li> <li>• suitable for static applications</li> <li>• large-area expandability</li> </ul>	<ul style="list-style-type: none"> <li>• low piezoresistive gauge factors, low sensitivity</li> </ul>
<b>piezo-electric</b>	<ul style="list-style-type: none"> <li>• high strain sensitivity</li> <li>• well suited for dynamic applications</li> <li>• mechanically flexible</li> <li>• sensing elements do not require electrical power supply</li> <li>• insensitive to electric and magnetic fields</li> <li>• wide measuring range</li> <li>• linearity between output signal and applied load</li> </ul>	<ul style="list-style-type: none"> <li>• charge amplifier required</li> <li>• not suitable for truly static applications</li> <li>• 3D force sensing difficult</li> </ul>
<b>conductive polymer</b>	<ul style="list-style-type: none"> <li>• mechanically flexible, stretchable</li> <li>• large-area expandability</li> <li>• chemically resistant, robust</li> <li>• low-cost fabrication techniques</li> </ul>	<ul style="list-style-type: none"> <li>• 3D force sensing difficult</li> <li>• low sensitivity</li> <li>• short lifetime (IPMC)</li> <li>• material hysteresis (PCR)</li> </ul>

## 2.5. Microfabricated force sensors

Table 2.2 – continued from previous page

TYPE	ADVANTAGES	DISADVANTAGES
<b>transistor</b>	<ul style="list-style-type: none"> <li>• can be placed on polymer materials</li> <li>• mechanically flexible, stretchable substrates</li> <li>• large-area expandability</li> <li>• suitable for static and dynamic applications</li> <li>• ease of integration with other flexible MEMS</li> <li>• relative ease of fabrication</li> </ul>	<ul style="list-style-type: none"> <li>• restricted to 1D force sensing</li> </ul>
<b>optical</b>	<ul style="list-style-type: none"> <li>• no cross-talk between wiring</li> <li>• insensitive to electric and magnetic fields</li> <li>• flexible, durable, robust (POF)</li> </ul>	<ul style="list-style-type: none"> <li>• 3D force sensing difficult</li> <li>• signal alternation due to bending</li> <li>• require expensive optical sources and detectors</li> <li>• even if sensor small, total package size large</li> </ul>
<b>magnetic &amp; inductive</b>	<ul style="list-style-type: none"> <li>• high sensitivity</li> </ul>	<ul style="list-style-type: none"> <li>• parasitic effects and noise</li> <li>• sensitive to electromagnetic interference</li> <li>• limited to nonmagnetic mediums</li> <li>• fabrication issues (thin ferrite films)</li> </ul>
<b>capacitive</b>	<ul style="list-style-type: none"> <li>• high sensitivity</li> <li>• temperature independence</li> <li>• 3D force sensing possible</li> <li>• can be placed on flexible polymer materials</li> <li>• large-area expandability</li> <li>• small sizes, high spatial resolution possible</li> <li>• low power consumption of capacitive elements</li> <li>• low drift, robust</li> </ul>	<ul style="list-style-type: none"> <li>• parasitic capacitances</li> <li>• cross-talk between elements</li> <li>• complex read-out circuitry</li> <li>• sensitive to electromagnetic interference</li> </ul>





### 3 Flexible capacitive sensor for uni-axial large force measurements

This chapter describes a microfabrication process for the realization of a flexible polyimide-based capacitive force sensor. The sensor has the ability to measure uni-axial loads in the range of industrial robots' grip forces. Capacitance and pressure sensitivity were modeled. Electrical characterization of the sensor under applied uni-axial force is presented.



Adapted from the journal article [175]:

*Flexible polyimide-based force sensor* (2012) **Dobrzynska J A** and Gijs M A M,  
Sensors and Actuators A: Physical **173**(1)127-135  
DOI: 10.1016/j.sna.2011.11.006

and conference proceedings [176]:

*Capacitive flexible force sensor* (2010) **Dobrzynska J A** and Gijs M A M,  
Procedia Engineering **5** 404-407, Eurosensors XXIV Conference  
DOI: 10.1016/j.proeng.2010.09.132

Photograph: the robotic gripper by Festo inspired by an elephant's trunk [55]

### 3.1 Introduction

Industrial robots work far beyond the physical abilities of humans – they experience constant heavy workloads and perform harsh repetitive tasks in dirty, hazardous factory environments. Just as hands are the organs of human manipulation, robots use *grippers* to come in direct contact with the workpiece [50]. However, tasks that appear simple to men, such as picking up and manipulating objects, can be vexingly complicated for robots [177].

The gripping mechanisms of an industrial robot are usually gripper jaws, claws or mechanical fingers [14, 50], whose contact surface is shaped according to the object that the robot lifts; *i.e.*, if a robot is designated a task to lift barrels, the gripper's contact surface is round to make the grip efficient. Moreover, modern industrial robots and their grippers are expected to adapt to the changes in environment [7, 55]. They are designed in various geometries, with soft and flexible materials [15, 16], conforming to arbitrary shapes, as, *e.g.*, a ground-coffee-filled balloon-gripper for picking up unfamiliar objects [177], or a smooth-movement handling genuine biomechatronic elephant's trunk [55].

The secure gripping and handling of objects requires an adequate *force sensing* mechanism. Yet, in a typical factory environment, robots are required to work constantly with heavy objects and at high speeds. Hence, the grip forces of industrial robots hit relatively large values, caused primarily by the heavy weight of the grasped object, secondly due to acceleration exerted upon its motion. Thus, the gripper force required to handle, *e.g.*, a packet of 10 kg may easily reach as much as a few kN [50].

For reliable grasp operation, the force sensors must respond to criteria of a large load range and adapt to the non-planar or flexible surfaces of grippers, hence very few tactile sensors find regular application in industry [14, 52, 73].

This thesis chapter discusses a microfabrication technology of flexible force sensors with an excellent durability and resistance to forces in the kN range. Polyimide (PI)-based capacitive force sensors were realized using a clean room batch-type process and a robust bonding scheme. I also present an analytical model and the electrical characterization of the sensor. Such flexible and durable force sensors can find possible application in the measurement of the grip force of an industrial robot, conforming to arbitrary shapes of gripper jaws.

## 3.2 Materials and methods

### 3.2.1 Design of the capacitive sensor

Figure 3.1a presents a conceptual view of my flexible capacitive force sensor. Two metallic electrode levels are embedded in three layers of polymeric packaging, forming four redundant capacitors (C1-C4) with a common top electrode. Figure 3.1b is a schematic diagram of the metal electrode parts of the sensor with the two levels of finger-like microstructures. The finger-like geometry of the sensor has been chosen to maintain the flexibility of the sensor, when it is deformed during force application on curved and rough surfaces, thereby preventing deformation and cracking of the relatively large electrode surface, which could be a problem when using a parallel full-plate capacitor. The electrodes' shape has been adopted to allow also three-axial force measurements when combined with an appropriate polymer dielectric medium (see chapter 4). Contact pads were designed on the lower metal layer, which is electrically connected to the top layer *via* a tapered pad. Consequently, bonding on the contact pads was possible and mechanical stability of the sensor has been maintained, even when the top electrode is displaced with regard to the bottom electrode. The electrode

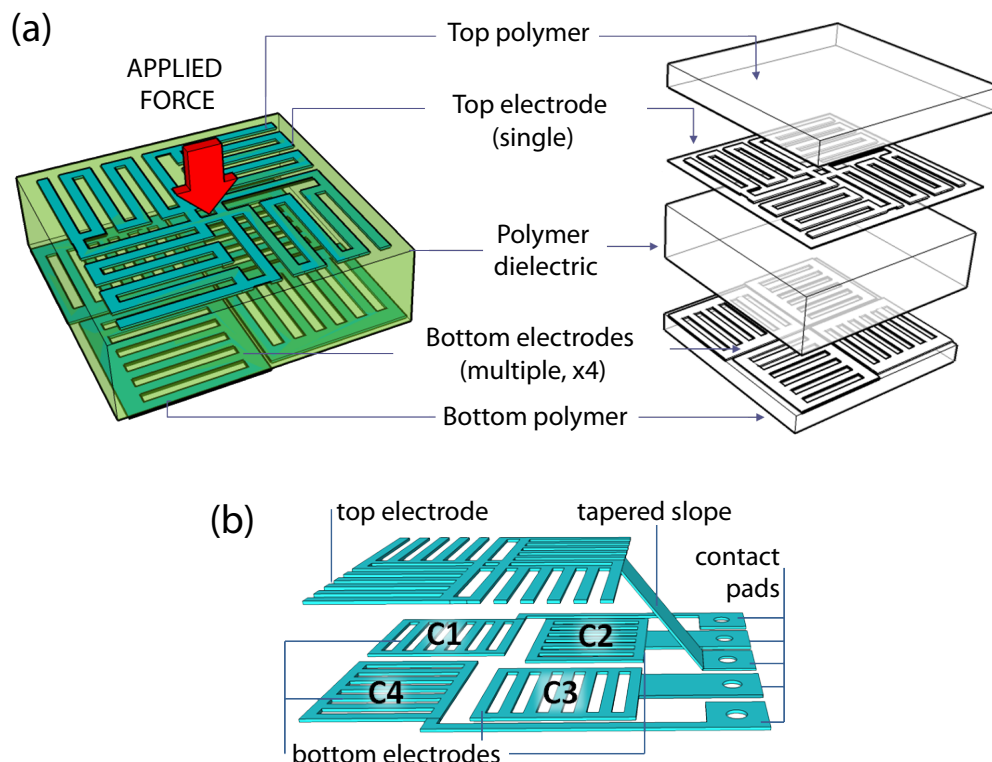


Figure 3.1: A conceptual view of (a) the flexible capacitive force sensor, (b) the metallic electrode parts of the capacitive structure.

structure is embedded in PI, except for openings on the contact pads. Each capacitor is composed of two fingered electrodes and has an area of  $5 \times 5 \text{ mm}^2$ ; the width  $w$  of a single finger is  $10 \text{ }\mu\text{m}$ , and the fingers are uniformly spaced by distance  $s$  of  $10 \text{ }\mu\text{m}$ <sup>a</sup>. The thickness of the insulation layer between top and bottom electrode in the absence of a load has been fixed at  $5 \text{ }\mu\text{m}$ . The cell deforms upon application of a normal force, decreasing the thickness of the insulation layer and increasing the capacitance value.

### 3.2.2 Microfabrication process of the PI-based sensor

The microfabrication process flow of the sensor is shown in figure 3.2. We started by sputtering on a silicon substrate a 500 nm thick conductive layer of tungsten (W), followed by the deposition of a sacrificial  $1 \text{ }\mu\text{m}$  aluminum AlO layer (figure 3.2a) (BAS450, Balzers). The W/AlO metallic layer was needed for anodic dissolution of the final flexible structure from the silicon support. The  $5 \text{ }\mu\text{m}$  thick PI1 layer was spin-coated and baked (figure 3.2b) (LSM 200, Sawatec), and a low-stress PI (PI2611, HD Microsystems) [178] was chosen in order to avoid buckling of the sensor structure after release from the silicon support wafer. The lower 500 nm thick aluminum electrode layer (Al1) was sputtered following an oxygen plasma surface activation step of the PI1 layer and deposition of a 50 nm film of Ti for adhesion (Spider 600, Pfeiffer). The electrodes were patterned in a dry etching process with  $\text{Cl}_2/\text{BCl}_3$  chemistry (figure 3.2c) (Multiplex ICP, STS), after which the remaining photoresist (PR) mask was dissolved in a remover bath (1165 Microposit Remover, Shipley).

The  $5 \text{ }\mu\text{m}$  dielectric layer PI2 was spin-coated (figure 3.2d), baked and patterned in such a way, that smooth slopes in PI2 were obtained. The smooth PI slopes were obtained by combining lithographic resist-reflow techniques [179, 180] with dry etching procedures. A photolithographic process was used to structure the PR in a tapered shape (figure 3.2e), followed by an anisotropic plasma etch to transfer the pattern into PI. For this photolithographic process two distinct PRs were tested:

- (i) AZ ECI 3027 (AZ Electronic Materials), a PR which after exposure and development exhibits an oblique sidewall topography (SVG 88, Rite Track),
  - (ii) AZ 9260 (AZ Electronic Materials), a PR with vertical sidewalls (EVG150, EV Group), which we melted after the development, on a hot plate at  $130 \text{ }^\circ\text{C}$  (RC8 THP, Karl Süss).
- Next, the  $5 \text{ }\mu\text{m}$  thick tapered PR pattern was transferred into PI2 by an anisotropic oxygen plasma etch (figure 3.2f) (Multiplex ICP, STS). Because of the very poor selectivity of the PR mask with respect to the etched PI2 layer, the profile of the PR was directly

---

<sup>a</sup>capacitors with smaller electrode areas of  $500 \times 500 \text{ }\mu\text{m}^2$ ,  $1 \times 1 \text{ mm}^2$ , and  $2 \times 2 \text{ mm}^2$  have also been fabricated, but are not further discussed in this thesis, since the measured with my setup force-induced signal change from these sensors was relatively small

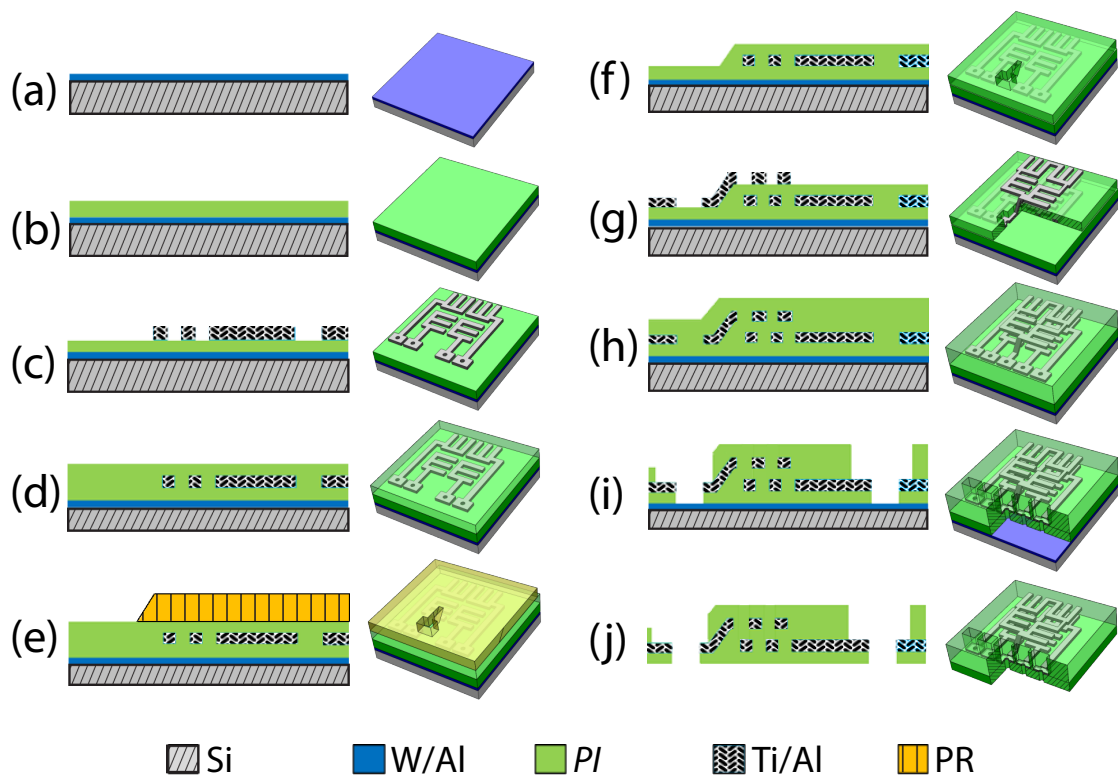


Figure 3.2: Process flow for the fabrication of the capacitive sensor: (a) sputter sacrificial W/Al<sub>0</sub>, (b) spin coat PI<sub>1</sub>, (c) sputter and pattern Ti/Al<sub>1</sub> bottom electrode, (d) spin coat PI<sub>2</sub> dielectric layer, (e) realization of a smooth PR slope, (f) dry etch PI<sub>2</sub>, (g) sputter and pattern Ti/Al<sub>2</sub> top electrode, (h) spin coat PI<sub>3</sub>, (i) dry etch PI<sub>3</sub> to open contact pads, (j) anodic dissolution of sacrificial Al<sub>0</sub> layer.

copied into the PI<sub>2</sub> substrate. The tapered slope allowed conformal metallization by a 50 nm Ti adhesion layer, followed by a 500 nm Al<sub>2</sub> top electrode layer (Spider 600, Pfeiffer), which was patterned in a dry etching process (figure 3.2g) (Multiplex ICP, STS).

The process continued by depositing the 5  $\mu\text{m}$  thick PI<sub>3</sub> layer (figure 3.2h), and deposition (Spider 600, Pfeiffer) and structuring (Multiplex ICP, STS) of an amorphous Si mask for defining the contact pad openings during a subsequent oxygen plasma dry etching step (figure 3.2i). Finally, the structures were released from the rigid Si wafer by anodic dissolution of the sacrificial Al<sub>0</sub> [181] (figure 3.2j). After microfabrication, the sensors were annealed at a temperature of 100 °C for 30 minutes, at a 3 kN load, in order to reduce the influence of eventual material meta-stabilities, cracks or irregularities, both in the PI and the electrodes.

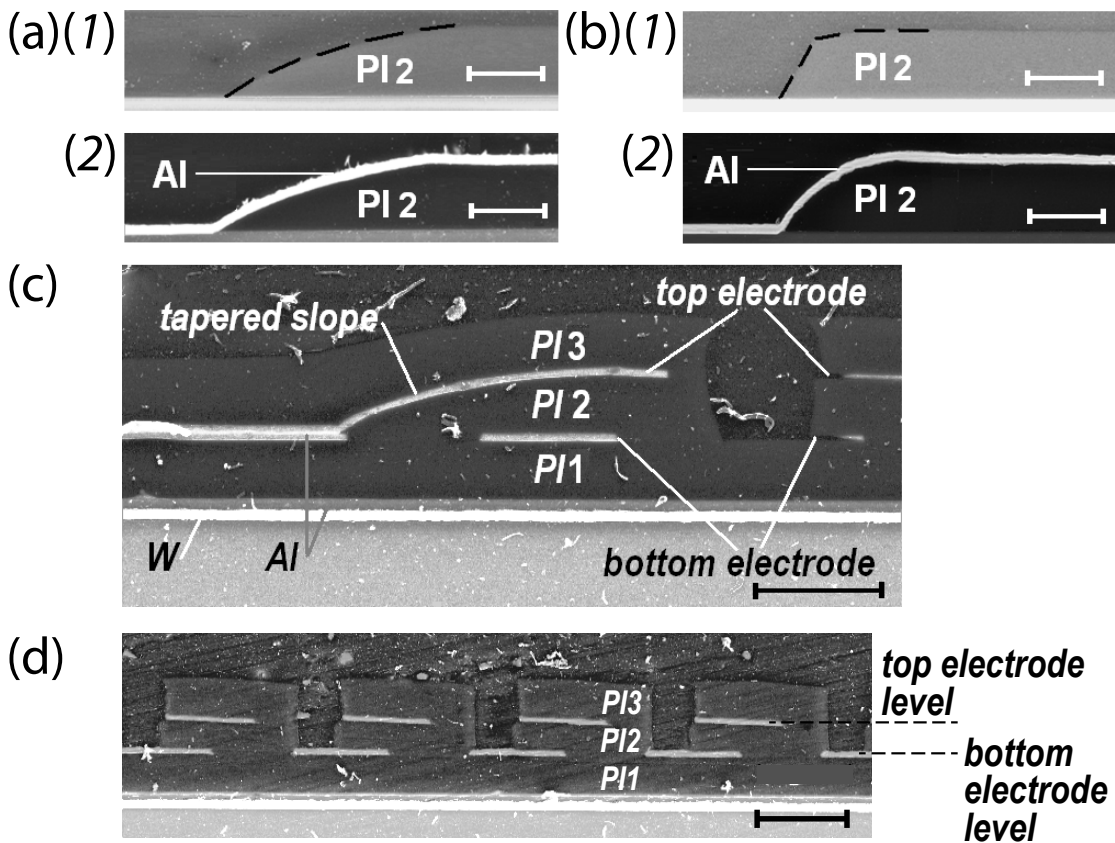


Figure 3.3: SEM cross-section micrographs (1) after realization of the smooth slope in PI2 and (2) after Al2 metal coverage, for two different photoresists used as a mask: (a) AZ ECI 3027, (b) AZ 9260. The scale bars correspond to  $5 \mu\text{m}$ . (c, d) SEM cross-section micrographs of the final device, before release from the rigid Si wafer. The scale bars correspond to  $10 \mu\text{m}$ .

### 3.2.3 Optical inspection of the fabrication process results

Figures 3.3a and 3.3b are Scanning Electron Microscopy (SEM) graphs showing the smooth PI2 slope after the PR structuring/dry etching step and after sputtering the layer Al2, for the two photolithographic methods proposed (see section 3.2.2). Figure 3.3c is a cross-section SEM graph of the finalized sensor stack embedded in three PI layers before release from the rigid support wafer, illustrating the connection between the top and bottom electrode *via* a tapered Al slope. The cross-section samples were prepared by embedding the sensor in a hard epoxy, and polishing with a tripod on a diamond paper with a grain size of up to 500 nm (Allied High Tech Products Inc).

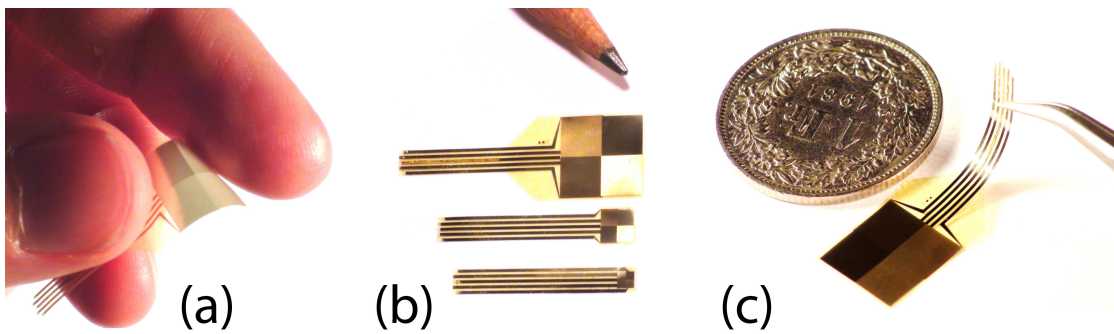


Figure 3.4: A single manufactured flexible capacitive force sensor released from the rigid support wafer.

A capacitive force sensor after release from the rigid Si wafer is shown in figure 3.4. The sensor is pliable and capable of being shaped to adapt to non-planar surface conditions.

### 3.2.4 Sensor packaging

For the connection of the sensor to the measurement system, several bonding techniques were investigated, such as conductive epoxy-based adhesives, soldering pastes, or polymeric anisotropically conductive adhesives. However, due to the extensive oxygen plasma dry etching processes, the oxidation of the aluminum contact pads imposed a serious connection problem.

The results of the X-ray photoelectron spectroscopy (XPS) analysis (AXIS Ultra HSA, Kratos) of the aluminum pad surface are shown in figure 3.5. In the analysis, two samples of aluminum pads were examined. The first sample (figure 3.5a) was oxidized in atmospheric conditions resulting in a native aluminum oxide layer. The second one (figure 3.5b) was treated with an oxygen plasma etch, which was long enough to open the metallic contact pads covered by the top polymeric layer. In order to remove the excess of the surface aluminum oxide layer, both samples were treated *in situ* with an ion beam (Ar<sup>+</sup>, 3 kV, 2 min). Based on the calculations of Carlson [182] and Strohmeier [183] and using an aluminum oxide/hydroxide thickness calculator [184], the analysis revealed an oxide layer that is twice as thick (6.4 nm), compared with the native oxide (3.2 nm), on top of the connection pad.

As the oxide layer is difficult to be removed with standard microfabrication processes, we preferred to fissure this layer and make the connection with the underlying metallic aluminum using mechanical action *via* a gold bump bonding technique [185], attaching the sensor reliably to a printed circuit board (PCB) (manual wire bonder,

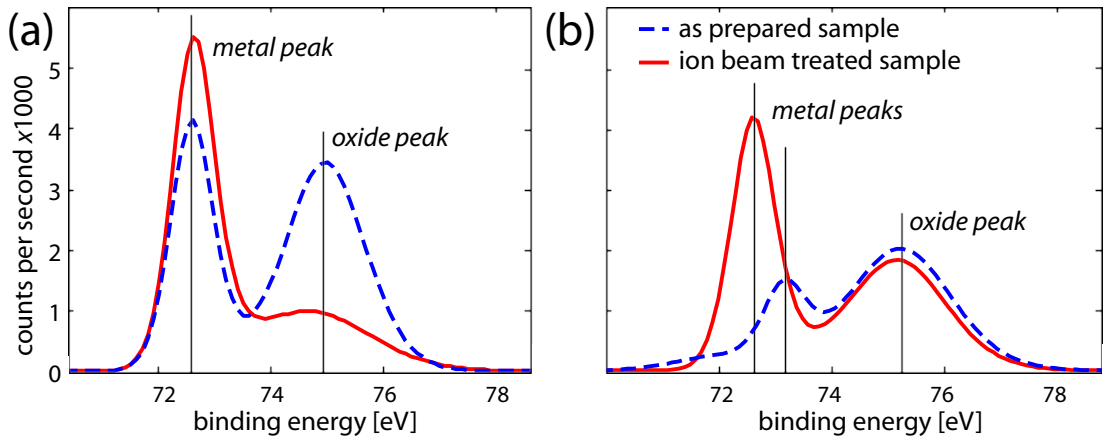


Figure 3.5: X-ray photoelectron spectroscopy (XPS) analysis of the Al contact pad surface, as prepared (dashed line), and treated with an ion beam (solid line) to remove the top oxidized layer. Two distinct natures of oxidation were examined: (a) native oxide: grown under atmospheric conditions, (b) oxide: formed in an oxygen plasma process.

Kulicke & Soffa), and maintaining the flexibility of the package. Figures 3.6a-d show a sensor, obtained after release from the silicon support, and attached to the PCB, connecting sensory pads with a golden stud.

### 3.3 Modelling and electrical characterization

#### 3.3.1 Modelling of the finger-like capacitive sensor

Finite Element Method (FEM) analysis (COMSOL Multiphysics 3.5a) was used to compare the modeled capacitance to its experimentally measured values. The geometry of the simulated sensor is illustrated in figure 3.1 and the dimensions are those mentioned in section 3.2.1. For the analysis, the dielectric material constant of the polymer was chosen  $\epsilon = 4$  [178]. The simulation results are shown in figure 3.7 (with indication of the geometrical parameters  $t$ ,  $s$ ,  $w$ , and  $h$ ) and represent two-dimensional (2D) analysis along the cross-section plane, similar to the one presented in figures 3.3c and 3.3d.



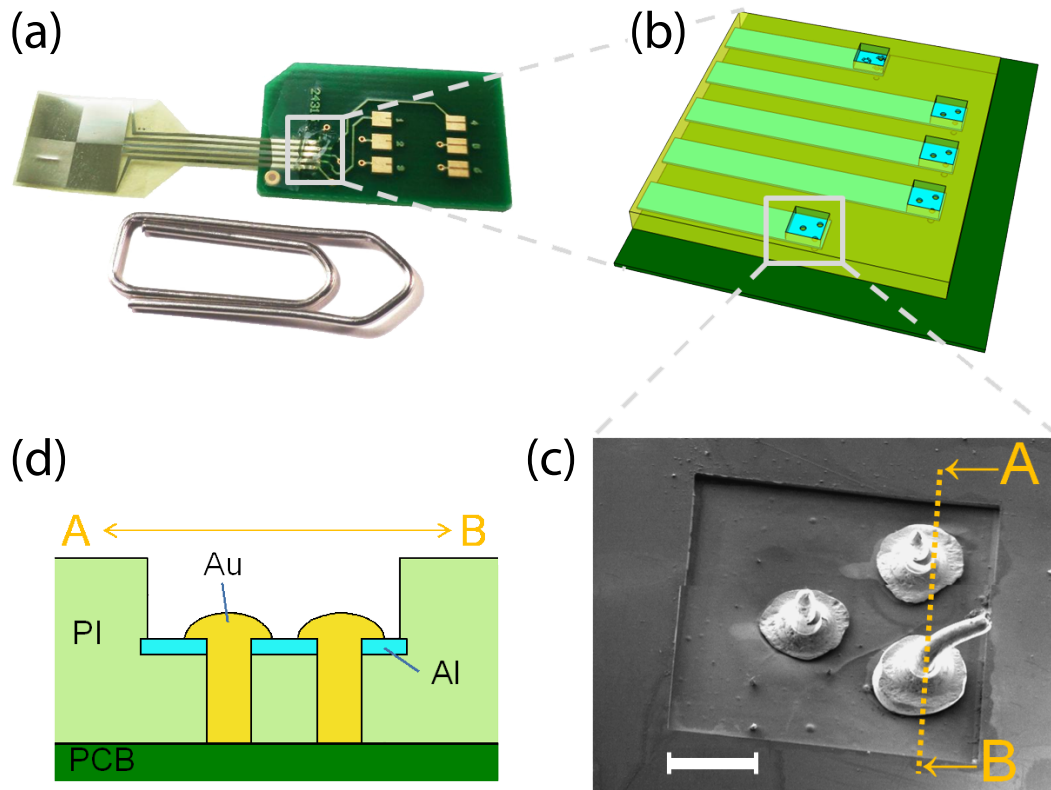


Figure 3.6: (a) Flexible sensor released from the silicon support wafer and bonded to a PCB; (b) magnified schematic view of the connection pads area. (c) SEM picture of the gold bump bonding: 3 gold bumps on the surface of the square Al contact pad, form the through-hole contact with the PCB. The scale bar is  $100\ \mu\text{m}$ . (d) Cross-section view of the through-hole bonded pads.

I also used the FEM analysis for the simulation of the effect of polymer thickness  $h$ . The results are shown in figure 3.8a. The capacitance change as a function of the dielectric's thickness is in excellent agreement with a modified Sakurai's formula<sup>b</sup> [186] (equation 3.1).

$$\begin{aligned}
 C \cong n \cdot \epsilon_0 \epsilon \left\{ a_1 \cdot 1.15 \left( \frac{w}{h} \right) + a_2 \cdot 2.8 \left( \frac{t}{h} \right)^{0.222} + \dots \right. \\
 \left. + 2 \left[ a_3 \cdot 0.03 \left( \frac{w}{h} \right) + a_4 \cdot 0.83 \left( \frac{t}{h} \right) + a_5 \cdot 0.07 \left( \frac{t}{h} \right)^{0.222} \right] \cdot \left( \frac{h}{s} \right)^{1.34} \right\} \cdot L
 \end{aligned} \quad (3.1)$$

where  $C$  is the capacitance between the top and bottom electrode,  $n$  is the number of electrode fingers,  $\epsilon_0$  is the vacuum permittivity,  $h$  is the dielectric thickness,  $w$  is the width of a single electrode finger,  $s$  is the spacing between single electrode fingers,  $t$  is the thickness of a single electrode,  $L$  is the length of electrode fingers, and

<sup>b</sup>for original Sakurai's formula refer to appendix A (A.1)

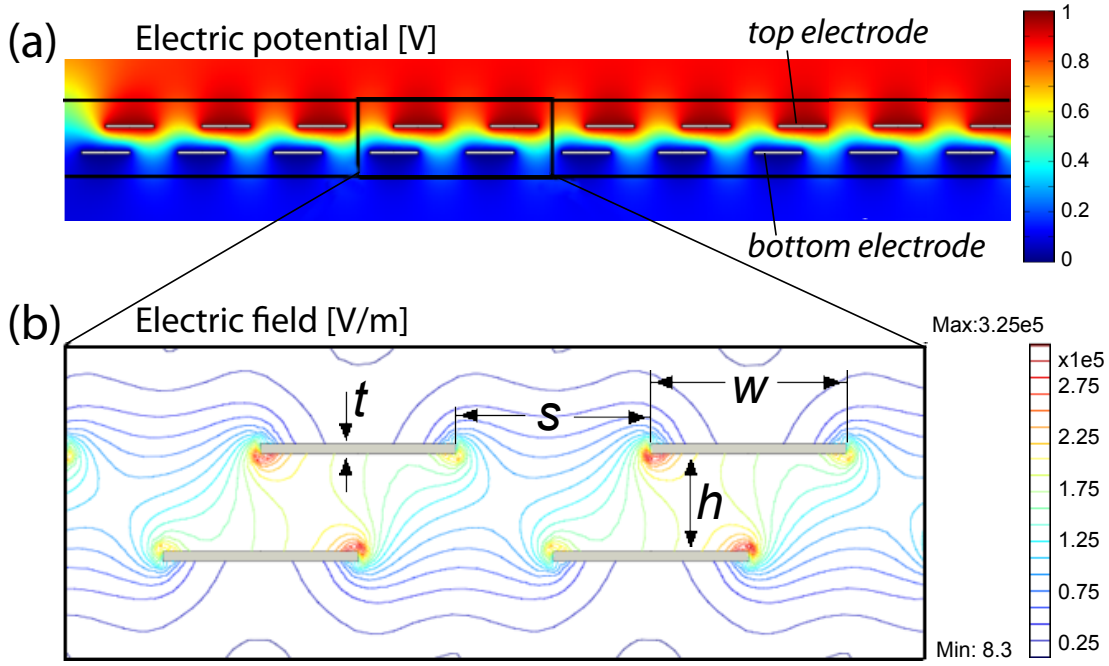


Figure 3.7: Results from a 2D simulation of the electrical field and potential for a finger-like electrode capacitive sensor. The geometrical parameters are defined in Sakurai's formula.

$a_1 \dots a_5$  are fixed fitting parameters of order one<sup>c</sup>, which take into account that the two capacitor electrodes have finger-like structures (the original Sakurai's formula is only modeling the stray capacitance between a finger-like electrode and the continuous plane counter electrode).

The force sensitivity of the sensor  $\frac{\Delta C}{\Delta F} = \frac{\Delta C}{\Delta h} \cdot \frac{\Delta h}{\Delta F}$ , given with equation 3.3, was calculated from formulas 3.1<sup>d</sup> and 3.2:

$$\Delta F = F_0 \frac{\Delta h}{h_0} \quad (3.2)$$

$$\begin{aligned} \frac{\Delta C}{\Delta F} = & \frac{-b_1}{(F_0 + F)} + \frac{b_2}{F} \left[ \left( \frac{F_0}{F_0 + F} \right)^{0.222} - 1 \right] + \dots \\ & + \frac{b_3}{F} \left[ \left( \frac{F_0 + F}{F_0} \right)^{0.34} - 1 \right] + \frac{b_4}{F} \left[ \left( \frac{F_0 + F}{F_0} \right)^{1.118} - 1 \right] \end{aligned} \quad (3.3)$$

<sup>c</sup>in this thesis, I employed  $a_1 = 0.34, a_2 = 2.10, a_3 = -39.75, a_4 = 1, a_5 = 6.58$ , which were obtained by curve-fitting and result in the root-mean-square error of 0.08583 pF when compared with the FEM analysis

<sup>d</sup>equation 3.3 was obtained *via* Taylor series expansion of equation 3.1 (see appendix B, equation B.2)

### 3.3. Modelling and electrical characterization

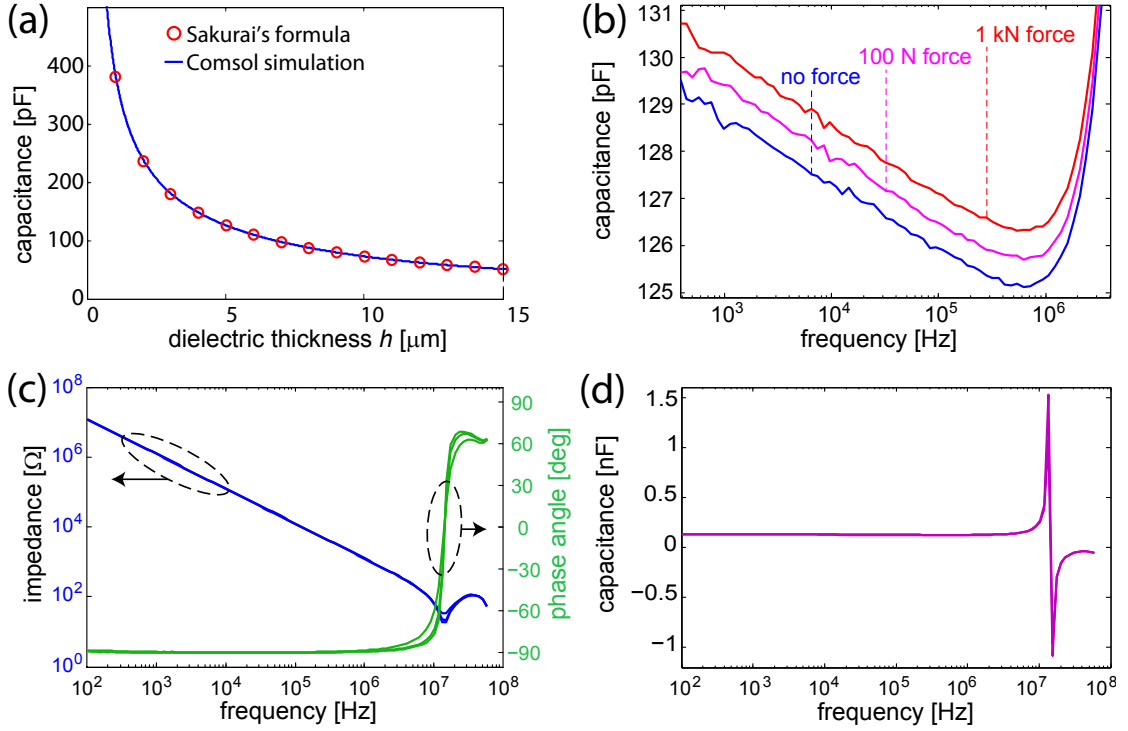


Figure 3.8: (a) Numerically simulated capacitance *vs* dielectric thickness, and its fit with equation 3.1. (b) Sensor response to applied experimental loads: capacitance *vs* frequency characteristics. (c, d) Frequency characteristics of the four redundant capacitors of one sensor: (c) impedance and phase angle, and (d) capacitance. The overlapping curves indicate the high reproducibility of the fabrication process.

where  $h_0$  and  $\Delta h$  is the dielectric's initial thickness and its change,  $b_1 \dots b_4$  and  $F_0$  are geometrical and material constants defined in formulas 3.4a-e, and  $E$  is the Young's modulus of the dielectric material.

$$b_1 = 1.15n \cdot \epsilon_0 \epsilon w L a_1 h_0^{-1} \quad (3.4a)$$

$$b_2 = 2.8n \cdot \epsilon_0 \epsilon t^{0.222} L a_2 h_0^{-0.222} \quad (3.4b)$$

$$b_3 = n \cdot \epsilon_0 \epsilon s^{-1.34} L (0.06 w a_3 + 1.66 t a_4) h_0^{0.34} \quad (3.4c)$$

$$b_4 = 0.14n \cdot \epsilon_0 \epsilon t^{0.222} s^{-1.34} L a_5 h_0^{1.118} \quad (3.4d)$$

$$F_0 = EA \quad (3.4e)$$

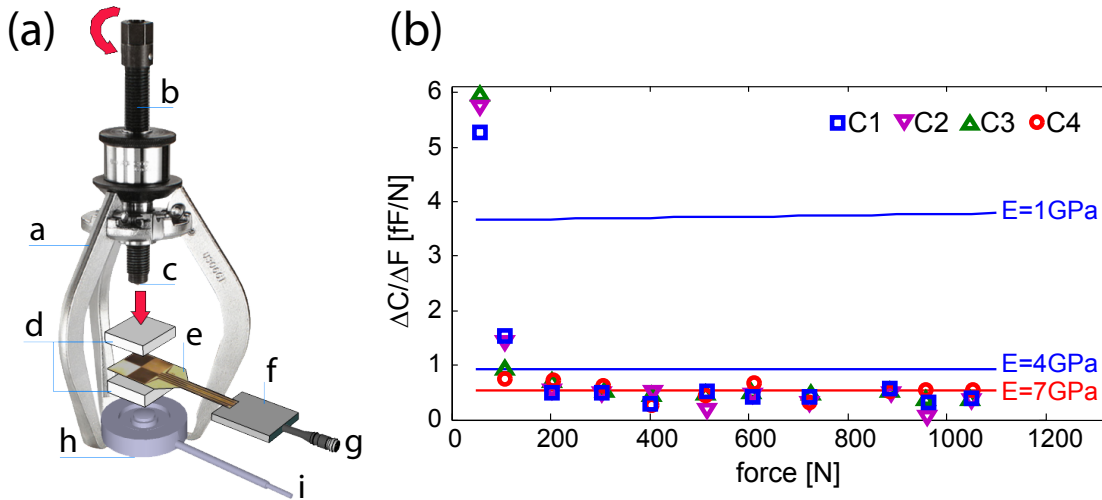


Figure 3.9: (a) Conceptual view of the experimental setup for testing the force sensor: a - gripper; b - screw; c - bearing; d - blocks; e - flexible force sensor; f - PCB; g - connection to impedance analyzer; h - load cell; i - connection to a PC. (b) Sensitivity of the sensor  $\Delta C/\Delta F$  vs applied force: as measured (points) and calculated from equation 3.3 (curves), for various values of polymer's Young's modulus  $E$ .

### 3.3.2 Electro-mechanical characterization of the uni-axial force sensor

Figures 3.8c, d show the electrical characterization<sup>e</sup> of the four unloaded capacitors of a single sensor, as measured with an Agilent 4294A impedance analyzer, at stable laboratory conditions (room temperature, 70% relative humidity). The measured initial (under zero-load conditions) capacitances were in the range of 120-140 pF. The curves of the four capacitors of the same sensor coincide, showing the high reproducibility of the fabrication process. The measured and the calculated capacitance values (125 pF, see section 3.3.1) are in good agreement. The measured cut-off frequency of the device was 10 MHz.

Force sensing experiments were done with the measurement setup shown in figure 3.9a. A self-centering, self-gripping puller with a ball-bearing ended screw was used to compress the force sensor locked in-between stiff blocks and a load cell (iLoad Pro Digital, LoadStar Sensors), the latter being used to measure the applied force. The sensor's response was found to be susceptible to the nature of the material of the blocks, especially if these had conductive metallic surfaces. When a conductive object was in proximity to the surface of the sensor, it disturbed the capacitive cou-

<sup>e</sup>capacitance  $C$  was derived from the imaginary part of the  $Z$  complex impedance,  $\Im(Z) = \frac{-1}{2\pi fC}$ , where  $f$  is the frequency

### 3.3. Modelling and electrical characterization

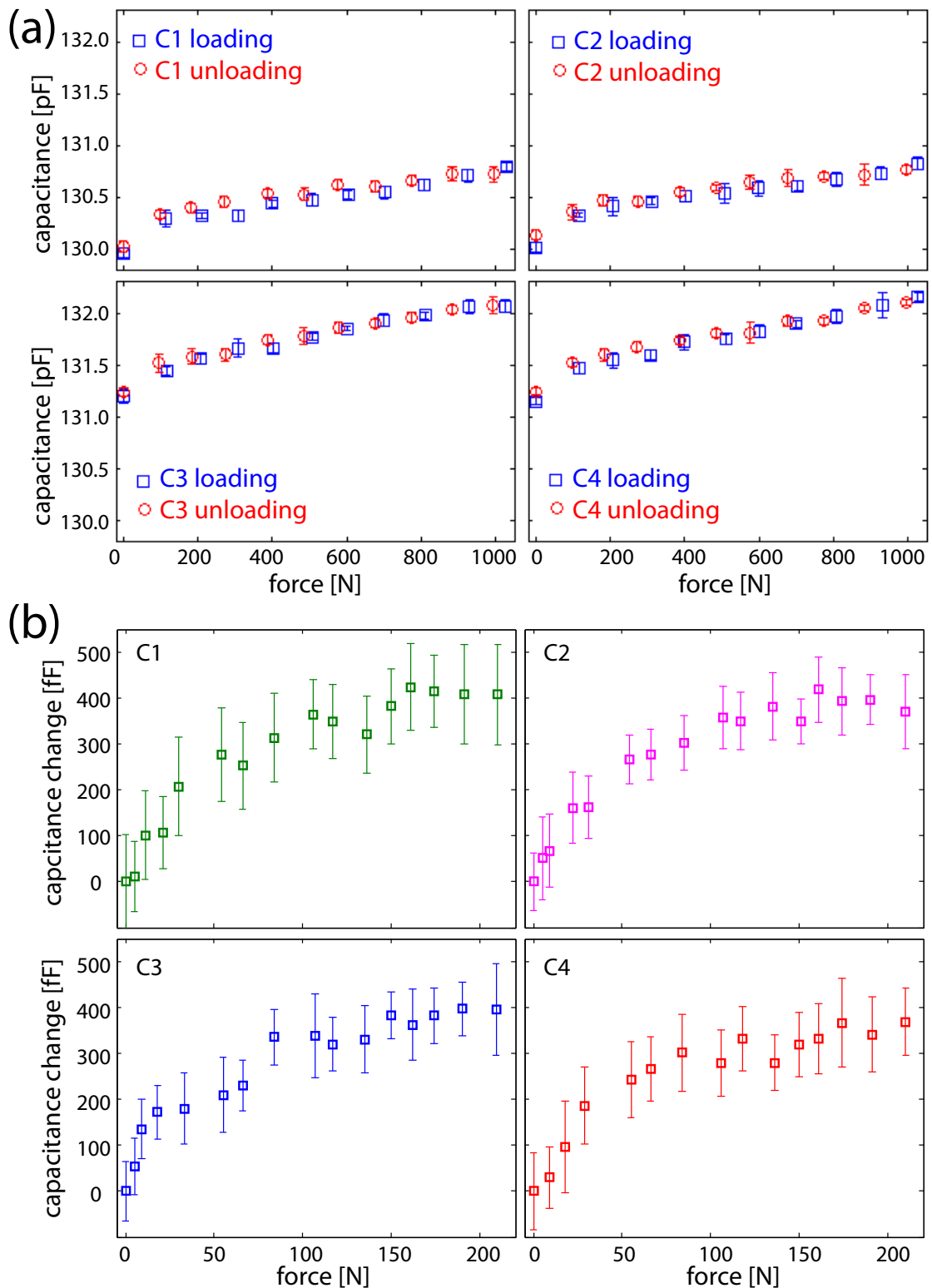


Figure 3.10: Measurement results: output capacitance at 5 kHz *vs* applied compressive load for four capacitors (C1-C4) of the same sensor during (a) loading (squares) and unloading cycle (circles), and (b) loading experiments in the lower force range of 0-200 N.

### Chapter 3. Flexible capacitive sensor for uni-axial large force measurements

---

pling between the electrodes. Indeed, when the material was electrically conductive and floating, it acted as an additional capacitive plate and the measured capacitance  $C$  increased; *e.g.* when a conductive steel plate was placed at  $150\ \mu\text{m}$  distance to the sensor, its initial capacitance  $C_0=130.9\ \text{pF}$  increased by  $\sim 1.5\ \text{pF}$ . On the contrary, when the sensor was close to a grounded metal plate, the measured capacitance  $C$  decreased. For our loading experiments, we avoided therefore metals in proximity of the capacitive sensor and used polymethylmethacrylate (PMMA) as material for the blocks.

Figure 3.8b shows the sensor's capacitive response to two applied loads. The measurements of the relative capacitance change as a function of frequency show that the capacitors responded similarly at all frequencies outside the range of the resonance. A frequency of  $5\ \text{kHz}$  has been chosen for further electrical characterization of the sensor. Figure 3.10a shows the results of the measured capacitance *versus* applied force in the  $0\text{-}1\ \text{kN}$  range. In order to minimize errors in the measurement, the average value from 5 consecutive sample measurements was taken for every data point, and the error bars indicate the standard deviation from the mean value. Both sensor loading and unloading characteristics were obtained, revealing no hysteresis effect. Moreover, the sensor response was nearly linear over the whole measurement range. The value of the experimentally measured capacitance was in excellent agreement with the computer simulations from figure 3.8a. The deviation from linearity in the lower force range (up to  $100\ \text{N}$ ) could be due to the change of the dielectric material constant  $\epsilon$  upon compression of the polymer, or the presence of microcracks in the aluminum film, an effect that has been already observed for mechanically stressed platinum films [187]. A minor difference of initial capacitance values between the four capacitors can be noticed, most probably due to the geometrical design of the electrical leads. From dedicated loading experiments in the lower force range, illustrated in figure 3.10b, a lower limit of detection of  $100\ \text{N}$  was deduced.

Figure 3.9b illustrates the sensitivity of the sensor over the whole measured force range. For forces above  $200\ \text{N}$ , a sensitivity of  $\Delta C/\Delta F \sim 0.5 - 1\ \text{fF/N}$  was found, which corresponds to  $\sim 5 - 10\ \text{fF/100 kPa}$ , in agreement with similarly designed sensors [85]. For a given elastic modulus  $E$ , the calculated sensitivity (formula 3.3) was compared with the measurement results in figure 3.9b. The theoretical prediction using a PI's modulus value of  $E = 7\ \text{GPa}$  [178] shows a good match with the experimental data.

Table 3.1 compares my sensor with similar capacitive force-detecting sensors reported in the literature [85, 86, 156, 165, 166, 168, 188]. The maximum applicable force on the sensor exceeded that of similar flexible sensors by a factor of at least 100, resulting in a more suitable range for large force applications. Moreover, the sensor yields much

Table 3.1: Comparison of capacitive force detecting sensors.

Device	Sensitivity	Maximum force limit	Cut-off/resonance frequency	Sensory surface flexibility
this work [175]	0.5-1 fF/N 5-10 fF/100 kPa ~0.8%/kN	3 kN 30 MPa	10-20 MHz	yes
Cheng [168]	290-1780 fF/100 kPa <sup>a</sup> 2.27-0.03%/kPa	5 N 430 kPa	13 kHz	yes
Lee [165, 166]	5-6 fF/mN <sup>a</sup> 43-48 fF/100 kPa <sup>a</sup> 2.9%/mN	10-40 mN 130-250 kPa	not reported	yes
Cotton [85]	13-17 fF/100 kPa	~5 N <sup>a</sup>	>32 kHz	yes
Kothari [188]	17 pF/100 kPa <sup>a</sup>	3 MPa	100-200 kHz	no
Tseng [86]	26.9 pF/100 kPa	50 mN	not reported	no
Chu [156]	13 fF/mN	10 mN	162 Hz	no

<sup>a</sup> Values interpreted from figures or estimated from the data available in the publication.

higher cut-off frequency (by a factor of not less than 100).

In addition, the testing was performed on surfaces with curvatures. Figure 3.11 compares the response of the flat sensor to the situation when it was bent, by placing it in-between convex and concave cylindrical surfaces with various radii  $R$  of 15 mm, 25 mm, 50 mm, and 75 mm. The sensor has tolerated the increased curvature and remained functional. A minor decrease in capacitance was obtained, which was due to differences between the normal force applied to the surface of the capacitor in the flat and bent case.

### 3.4 Summary and discussion

A flexible capacitive force sensor for large force measurements has been developed. Flexibility was assured by using PI as a dielectric. Robust packaging of the sensor was obtained by embedding all metal electrode parts in PI, and a reliable connection with a PCB was realized by using a gold bump bonding technique. The experimental capacitive values were in good agreement with theoretical predictions. The sensor revealed high strength and high durability. When operated in the 1 kN force range, it exhibited linearity and absence of hysteresis, a lower detection limit of 100 N, as well as an acceptable sensitivity of 0.5-1 fF/N. The force sensor could continuously

### Chapter 3. Flexible capacitive sensor for uni-axial large force measurements

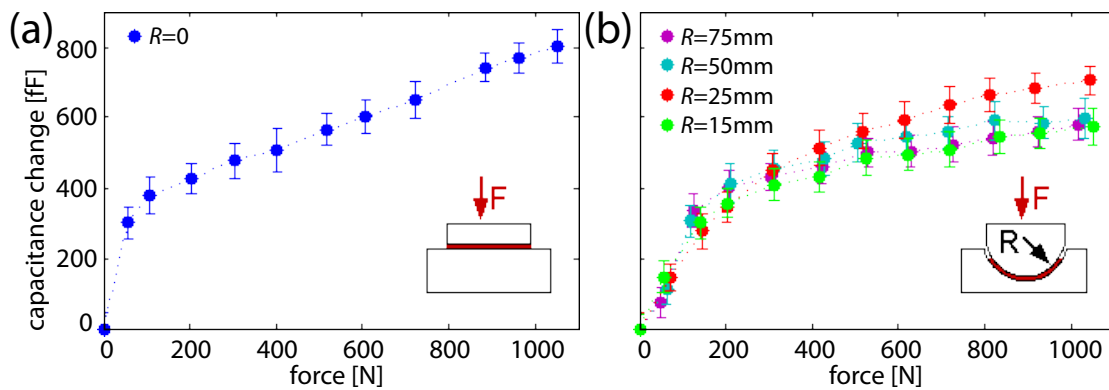


Figure 3.11: Measured change in capacitance  $vs$  force applied to the sensor when compressed (a) on a flat surface, (b) in-between convex and concave cylindrical surface with radius  $R$ .

withstand higher loads, in excess of 3 kN, without damage. The transducer was flexible and functioned well on curved surfaces with radii between 15 mm and 75 mm.

The functionality of the sensor has been maintained due to a tapered slope connection between the top and the bottom electrode, and fabricated entirely in the PI material. Similar 3D microstructures or microstructures with inclined sidewalls have been manufactured so far for optical lenses [179], microcavities [189], or suspended bridges and cantilevers [180]. However, most reported techniques have applied to the 3D structuring of PR, and concerned to less extent alternative resins such as PI, although commonly used as an interlayer dielectric in ICs [173] and a flexible package of sensors [174]. In my work, the PI was structured in a 3D tapered shape using photolithographic processes with dry etching procedures, resulting in a 3D microstructure that provided robustness to the device.



## 4 Flexible capacitive sensor for three-axial force measurements

This chapter describes the design and the microfabrication process of a flexible-substrate-based capacitive force sensor. Being sensitive both to normal pressure and shear forces, the sensor has the ability to measure three-axial loads as perceived by human foot-skin in gait and hand-skin in grasp. Capacitance and 3D force sensitivity were modeled. Electrical characterization of the sensor under applied 3D force is presented.



Adapted from the journal article [190]:

*Polymer-based flexible capacitive sensor for three-axial force measurements*

(2013) **Dobrzynska J A** and Gijs M A M,

Journal of Micromechanics and Microengineering **23**(1)015009

DOI: 10.1088/0960-1317/23/1/015009

Photograph: the precise manipulation of dexterous hand fingertips, Shadow Robot Company [54]

### 4.1 Introduction

Science fiction fans certainly recall well the scenes of the 1980s movies in which the cyborg Terminator repaired his bionic arm [191] or the Star Wars hero Luke Skywalker tested his brand-new prosthetic hand [192]. Appearing as unrealistic futuristic visions of Hollywood, today, the technological advancements offer active prosthetic hands and fingers as commercial products [10], dexterous robotic hands which map precise manipulation from a human to a robot [54], and brain implants to control and navigate sophisticated robotic arms [3]. The emerging and the prospective 21<sup>st</sup> century technologies call for *artificial skin* – a flexible large-area-expandable tactile sensing system.

A single taxel of an artificial skin should be robust, *flexible*, compliant, conformable, stretchable, and soft; able to withstand elevated temperatures, humidity, and chemical conditions, and sudden force impacts [42]. Moreover, it should exhibit a high sensitivity and a wide dynamic range, measuring a 3-*axial* contact force [22, 41]. So far, only few types of 3-axial force sensing devices have been reported which are deposited on, or entirely encapsulated in, elastic substrates [49, 79, 111, 112, 122, 165–168, 170, 171]. In particular, the measurement of 3D forces is needed, *e.g.*, for in-hand object manipulation, or determining the optimal grip force [28]. First, the *normal force*<sup>a</sup> tactile feedback limits the force to compress an object in a hand, so that the object does not crush. Second, the *shear force*<sup>b</sup> tactile feedback controls how strong to hold an object, so that the object does not slip between fingers. Similarly, the skin under the plantar surface of a foot provides important 3D tactile sensation, *e.g.* for human balance and gait [35]. Three-axial plantar ground reaction force (GRF) is a significant indicator in clinical evaluations [193–195], allowing, *e.g.*, control of a patient’s health state or progress after orthopedic surgical intervention [36].

In this chapter of the thesis I discuss the design and fabrication technology of a novel flexible-substrate-based 3-axial capacitive force sensor. The overall mechanical flexibility of the sensor is realized by an appropriate integration of three polymers – polyimide (PI), Parylene-C, and polydimethylsiloxane (PDMS) – with standard metallization techniques in a clean room batch-type fabrication process. I present a theoretical model and a complete electro-mechanical characterization of my sensor as a response to static 3-axial load, the results of which are compared with the range of pressures perceived by human hand- and foot-skin. This flexible 3D force sensor cell may serve as a taxel of an artificial skin.

---

<sup>a</sup>acting perpendicular to the surface

<sup>b</sup>acting parallel to the surface

## 4.2 Materials and methods

### 4.2.1 Design of the three-axial capacitive sensor

Figures 4.1 and 4.2a, b are schematics of the proposed flexible 3-axial force sensor. Two metal electrode levels are embedded in three layers of polymeric packaging, forming four unit capacitors (C1-C4) with a common top electrode. The electrodes have a finger-like shape which supports a high sensitivity to 3-axial forces and maintains the flexibility of the sensor. Several sensor designs have been adopted (figure 4.2c): I have basically varied the capacitor's area  $A = L \times L$  and the finger width  $w$ , while the distance  $h_0$  between the two electrode levels in all designs has been fixed at  $11 \mu\text{m}$  in the absence of a load. These geometrical parameters were chosen based on the simulation (Comsol Multiphysics 3.5a) of an optimized sensor's shear-detection performance, so that the high sensitivity to shear forces is provided (figure 4.3).

The sensing cell operation under the application of a 3-axial load is as follows. When a normal force  $F_z$  is applied to the sensor, the elastic dielectric is compressed, decreasing the distance  $h$  between the electrode levels and all four capacitors (C1-C4) increase their value.

When an  $x$ -axis ( $y$ -axis) shear force  $F_x$  ( $F_y$ ) is applied along the  $x$ -axis ( $y$ -axis), the elastic dielectric deforms in the direction of the shear, and the finger-like top electrode slides in parallel to the bottom electrode. Since each capacitor consists of a series of  $x$ -axis- (C1, C3) and  $y$ -axis-sensitive (C2, C4) fingered electrodes, the movement of the top plate affects the overlapping area between the corresponding

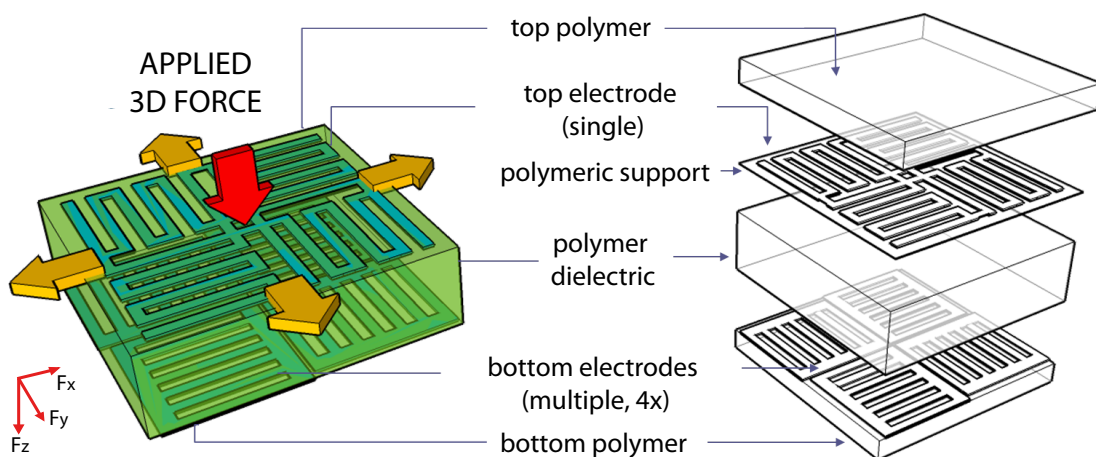


Figure 4.1: A conceptual exploded view of the layers of the flexible capacitive 3-axial force sensor.

## Chapter 4. Flexible capacitive sensor for three-axial force measurements

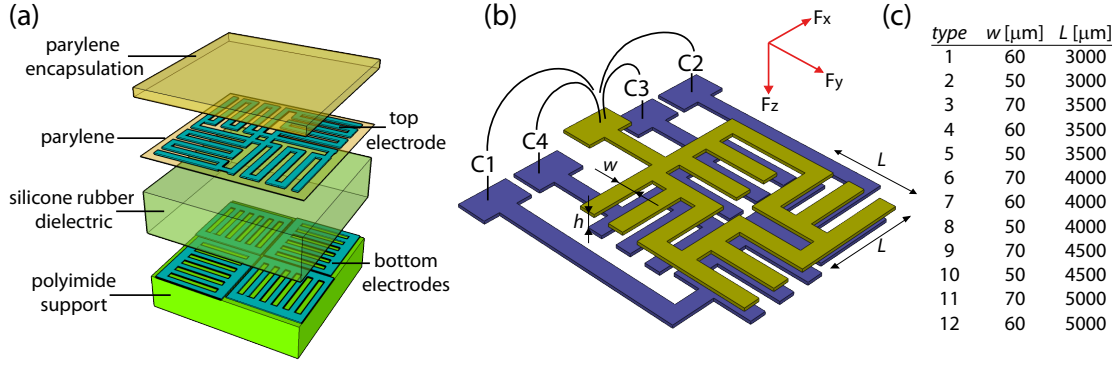


Figure 4.2: A conceptual view of the flexible capacitive force sensor. (a) Two metallic electrode levels are embedded in three layers of polymeric packaging. (b) The finger-like electrodes form four unit capacitors C1-C4, whose shape supports sensitivity to 3-axial force. (c) Table of fabricated sensors with varying geometry design.

electrodes, thus changing the capacitance value. Furthermore, the design of finger-electrodes is differential, so that under uni-axial shear, one shear-sensitive capacitor increases while the second one decreases its value; the remaining two capacitors are only sensitive to shear forces applied in an orthogonal direction, hence their values remain unchanged.

For example, when an  $x$ -shear force  $F_x$  is applied to the sensor, one  $x$ -shear-sensitive capacitance increases (capacitor C3), while the second one decreases (capacitor C1), and the  $y$ -axis-sensitive capacitors (C2, C4) remain unresponsive.

The normal pressure  $P_z$  is a function of  $\Delta C_z$ , which is independent of the applied shear force and can be derived from the read-out of the four capacitors as follows

$$\Delta C_z = (C_1 + C_2 + C_3 + C_4) - (C_1^0 + C_2^0 + C_3^0 + C_4^0) \quad (4.1)$$

where  $C_1 - C_4$  are the measured capacitances under an arbitrary 3-axial load and  $C_1^0 - C_4^0$  are the corresponding initial capacitances in the absence of load.

The shear pressures  $P_x$  ( $P_y$ ) are a function of  $\Delta C_x$  ( $\Delta C_y$ ), which are independent of the applied normal force and can be derived from the read-out of the two capacitors as follows

$$\Delta C_x = (C_3 - C_1) - (C_3^0 - C_1^0) \quad (4.2a)$$

$$\Delta C_y = (C_2 - C_4) - (C_2^0 - C_4^0) \quad (4.2b)$$

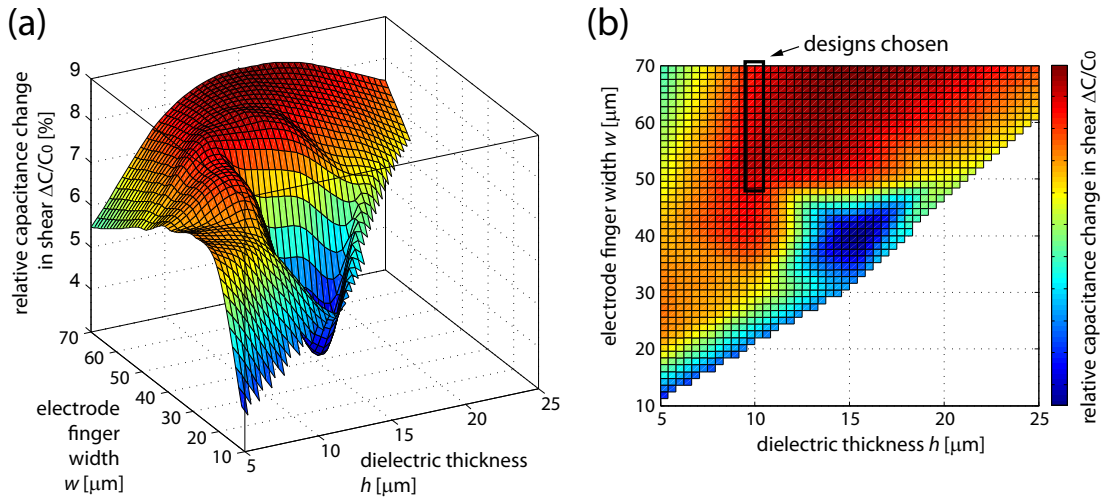


Figure 4.3: Relative capacitance change  $\Delta C/C_0$  when a given shear force  $F_x = 190$  kPa is applied on a sensor, as simulated by Comsol, assuming constant shear modulus  $G = 250$  kPa.  $\Delta C/C_0$  is dependent on the sensor's geometrical parameters: thickness  $h$  of the polymer dielectric and width  $w$  of the electrode finger. (a) the 3D and (b) the 2D representations of the parameters for optimization purposes. The designs chosen (marks) provide high sensitivity to shear forces.

#### 4.2.2 Microfabrication process of the polymer-based sensor

The fabrication process flow of the sensor is shown in figure 4.4. We started by sputtering (BAS450, Balzers) on a 4-inch silicon substrate a 200 nm conductive layer of tungsten-titanium (W:Ti 10%), followed by deposition of a sacrificial 800 nm aluminium (Al) layer needed for anodic dissolution of the final flexible sensor from the silicon support. The 5  $\mu\text{m}$  thick low-stress PI (PI2611, HD Microsystems) support layer was spin-coated and baked (figure 4.4a) (LSM 200, Sawatec). The lower 250 nm thick platinum electrode layer (Pt) was sputtered following an oxygen plasma surface activation step of the PI layer (Spider 600, Pfeiffer). A 50 nm film of Ti was used for adhesion of the Pt electrode, and deposited below and above the Pt layer. Over the metallic layer a heat-resistant resist mask (AZ ECI 3027, AZ Electronic Materials) was structured (SVG 88, Rite Track), preventing the photoresist (PR) from thermal degradation in subsequent high-power plasma etch. The electrodes were patterned in a dry etching process with  $\text{Cl}_2/\text{Ar}$  chemistry (figure 4.4b) (Multiplex ICP, STS), after which the remaining PR mask was dissolved in a remover bath (1165 Microposit Remover, Shipley). The wafers were primed for adhesion (VM-651, HD Microsystems) in an oven for 15 min at 105  $^\circ\text{C}$ , and backside-covered with a UV-curable adhesive tape (Adwill E-6142S, Lintec) for protection from subsequent polymer coatings. The 10  $\mu\text{m}$  silicone rubber PDMS (Sylgard 184, Dow Corning) dielectric layer with a curing agent:polymer ratio 1:10 was spin-coated (6800, SCS) and baked at 80  $^\circ\text{C}$  overnight.

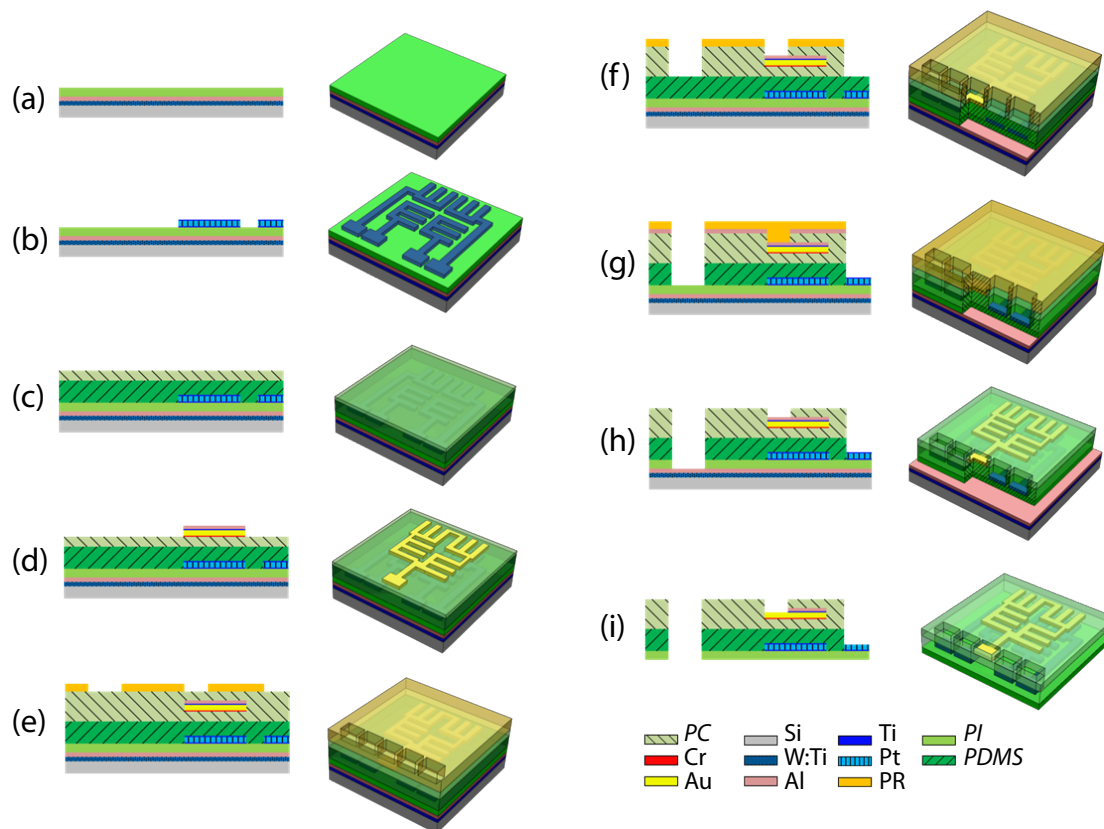


Figure 4.4: Process flow for the fabrication of the capacitive sensor: (a) sputter sacrificial W:Ti/Al, spin coat PI, (b) sputter and pattern Ti/Pt/Ti bottom electrodes, (c) spin coat PDMS dielectric, deposit Parylene-C, (d) evaporate and pattern Cr/Au/Ti/Al top electrode by lift-off, (e) deposit Parylene-C, spin-coat PR etch mask for contact pads openings, (f) dry etch Parylene-C, (g) spin-coat PR mask, dry etch PDMS, (h) dry etch PI, (i) wet etch Ti/Al, anodic dissolution of sacrificial Al layer.

The silane adhesion promoter (A-174, Comelec SA) was deposited and baked in an oven for 15 min at 90 °C, prior to room temperature (RT) deposition of a 1  $\mu\text{m}$  thick Parylene-C layer (figure 4.4c) (C-30-S, Comelec), and the backside protective tape was removed.

Next, lift-off patterns for the top electrode were prepared, by using an image reversal photoresist (nLOF 2070, AZ Electronic Materials), given the delicateness of the polymeric substrate, which cannot be processed at high temperatures, as these would degrade the PDMS and induce thermal stresses. This photolithography step was critical to obtain an undercut in the PR profile for subsequent metal evaporation and a reproducible lift-off of the film. The process parameters of exposure dose, reversal bake time and temperature, and development time had been optimized to get the desired PR profile. A 3.2  $\mu\text{m}$  thick PR layer was spin-coated and soft-baked at 110 °C

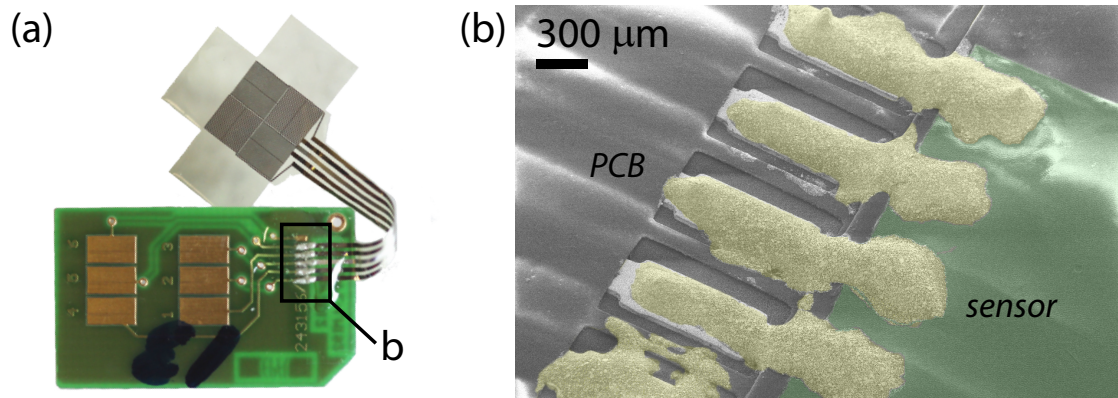


Figure 4.5: (a) Flexible sensor released from the silicon support wafer and bonded to a PCB. (b) Enlarged view of the bonding area, showing the connection between the sensor and the PCB by epoxy glue.

for 3 min (OPTIspin SB20, ATM), followed by an i-line UV-exposure with a dose of  $15 \text{ mJ/cm}^2$  (MJB4, Karl Süss). A post-exposure reversal bake at  $120 \text{ }^\circ\text{C}$  was performed on a hot plate for 2 min. The PR structures were developed by immersion (Microposit MF CD-26, Rohm and Haas Electronic Materials) for 3 min 30 sec.

The top electrode metallic layer was deposited over the patterned PR by RT evaporation (LAB 600H, Leybold Optics) of 20 nm of chromium (Cr) for adhesion, 200 nm of gold (Au), and 20 nm of Ti with 100 nm of Al as etch-stop layers for further processing steps. The electrodes were patterned by lift-off and placing the wafer in a solvent bath (Microposit Remover 1165, Shipley) for 24 hours (figure 4.4d). A  $1 \mu\text{m}$  thick protective layer of Parylene-C was RT-deposited over the structures (C-30-S, Comelec), and a  $14 \mu\text{m}$  thick low temperature PR (AZ 9260, AZ Electronic Materials) mask was deposited, soft-baked at  $90 \text{ }^\circ\text{C}$  (RC8 THP, Karl Süss) and patterned (MA6, DV10, Karl Süss) for succeeding etching steps to create contact pad openings (figure 4.4e). After the development step, the wafer was placed on a hot plate for 15 min at  $90 \text{ }^\circ\text{C}$ , in order to remove solvents remaining from the photolithography process. The Parylene-C was anisotropically etched in oxygen plasma, opening the contact pad areas of the top electrode (figure 4.4f) (Multiplex ICP, STS). The PR mask was redeposited (RC8 THP, MA6, DV10, Karl Süss) and PDMS was anisotropically etched in an Inductively Coupled Plasma (ICP) reactor (Multiplex ICP, STS) with  $\text{SF}_6$  chemistry using the process developed in [196], opening contact pad areas of the bottom electrodes (figure 4.4g). Oxygen plasma (Multiplex ICP, STS) was used to etch the bottom PI layer and render the final shape to the sensory structures (figure 4.4h). Wet etch in hydrofluoric acid (HF) removed the protective layers of Ti and Al from the cleared pad areas of the Pt and Au electrodes.

Finally, the flexible structures were released from the rigid Si wafer by anodic disso-

lution of the sacrificial Al [197] (figure 4.4i). The sensors were bonded to a printed circuit board (PCB) by using silver-filled conductive epoxy glue (Epo-Tek H20E, Epoxy Technology) (figure 4.5).

### 4.2.3 Optical inspection of the fabrication process results

Figure 4.6a shows a matrix of fabricated sensors on a wafer, before the final release step, while a single fabricated capacitive sensor composed of four capacitors C1-C4 is presented in figure 4.6b. The sensor released from the rigid wafer support is shown in figures 4.6c, d. The flexible sensor is pliable and capable of being shaped to adapt to various surface conditions.

Figure 4.6e is a Scanning Electron Microscopy (SEM, Carl Zeiss) picture of an enlarged contact pad area of four bottom Pt electrodes and a top Au electrode. The magnified view of the sensor's electrode area is shown in figure 4.6f, illustrating the initial half-finger shift between the top and bottom electrode. The surface of the top electrode is somewhat rough (see also a corresponding electrode area of cross-section image in figure 4.7b), since the surface of the PDMS film is buckled after the deposition of the Parylene-C, an effect which has been observed in other works [198] and that, in our case, is most likely attributed to stress inside an as-deposited Parylene-C film [199, 200].

Figure 4.8 illustrates how different PRs and process parameters influence the quality of the top electrode. Under optimum process conditions, the image reversal PR nLOF 2070 provides the best results for patterning the top electrode.

Figure 4.6e is a SEM photograph of the edge of etched Parylene-C and PDMS polymeric layers in the Pt contact pad area. The magnified view into this area, presented in figure 4.6g, demonstrates the anisotropy of the polymer etch and shows a clear pad surface ready for sensor bonding.

Figures 4.7a, b show cross-section SEM pictures of the finalized sensor stack embedded in three polymeric layers before release from the rigid Si wafer, illustrating the half-finger shift between the electrodes in the different levels and the local surface roughness of the top electrode. The cross-section samples were prepared by embedding the sensor in a hard epoxy, and polishing with a tripod on a diamond paper with a grain size of up to 500 nm (Allied High Tech Products Inc.).



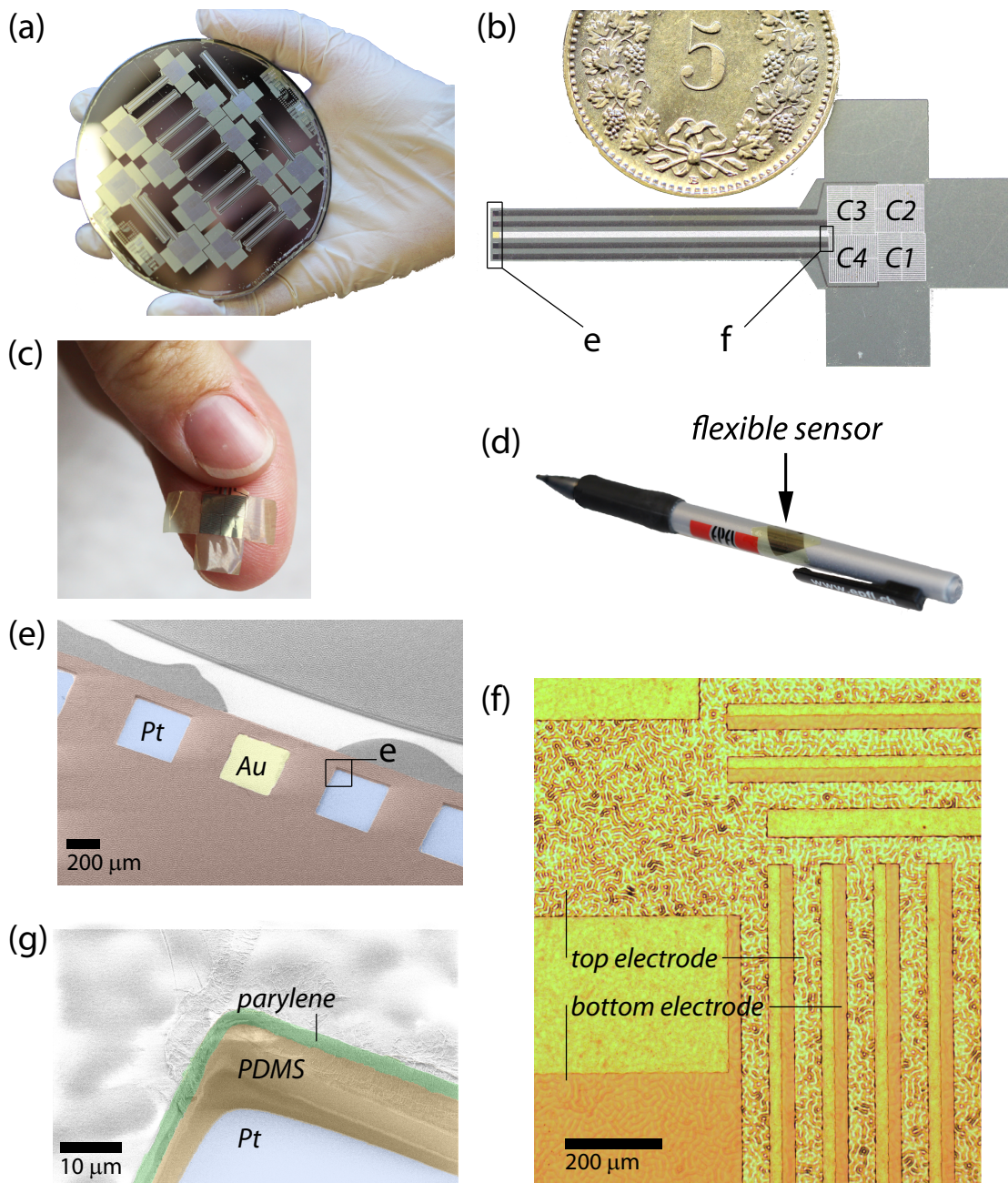


Figure 4.6: (a) A matrix of fabricated sensors on a wafer. (b) A single manufactured capacitive force sensor in comparison with a piece of 0.05 CHF. (c, d) Sensors released from the wafer support are capable of being flexed to adapt to various surface shapes. (e) SEM picture of an enlarged area around the contact pads, (f) magnified view of the electrodes' area illustrating the two levels of overlapping finger-like structures, and (g) SEM zoom onto the edge of anisotropically etched polymeric layers in the contact pad area.

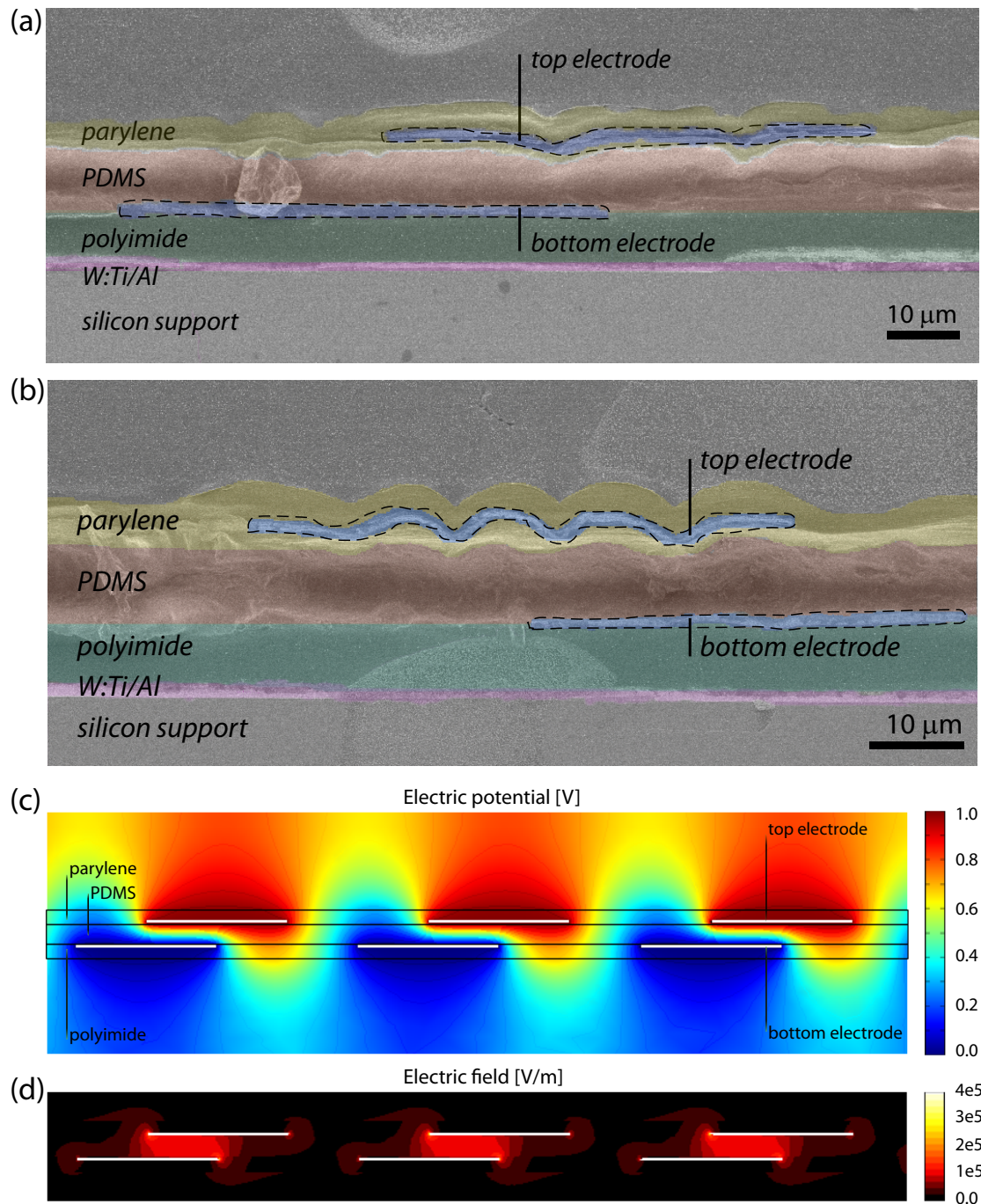


Figure 4.7: Cross-section views of the capacitive sensor. (a, b) SEM cross-section micrographs of the finalized device, before release from the wafer support, in (b) the cross-section was taken at a different plane to clearly show the the top electrode buckled. (c, d) Results from a 2D simulation of (c) the electric potential and (d) the electric field of a finger-like electrode capacitive sensor under zero-force conditions.

### 4.3. Modeling and electro-mechanical characterization

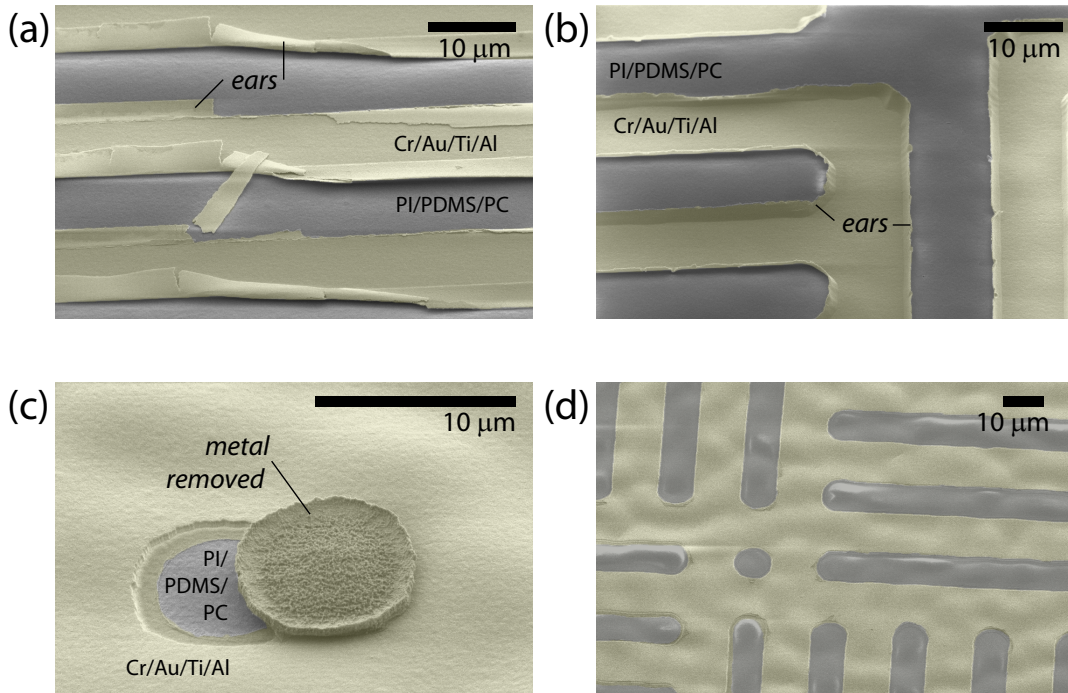


Figure 4.8: Comparison between different PRs used in the fabrication of the top electrode on the polymeric stack of PI/PDMS/Parylene-C: (a) collapsed ears of Cr/Au/Ti/Al patterned in lift-off by using PR AZ 9260, the sidewalls of which were not sufficiently inclined for lift-off, (b) oblique ears of Cr/Au/Ti/Al patterned in lift-off by using PR nLOF 2070, the sidewalls of which were not sufficiently inclined for lift-off, (c, d) desired pattern of Cr/Au/Ti/Al electrode, structured in lift-off by using PR nLOF 2070 with optimal process parameters.

## 4.3 Modeling and electro-mechanical characterization

### 4.3.1 Modeling of the capacitive force sensor

**Electrical model of the capacitive sensor.** For theoretical modeling I used Finite Element Method (FEM) analysis (COMSOL Multiphysics 3.5a) to compare with experimentally measured capacitance values. The simulated sensor's geometry and the structure's dimensions are those referred to in figures 4.2b, c. For the analysis, the dielectric material constants of the PI, PDMS and Parylene-C polymeric layers were chosen as  $\epsilon_{PI} = 4.15$ ,  $\epsilon_{PDMS} = 2.8$ ,  $\epsilon_{Par-C} = 3.1$ , respectively.

The simulation results are shown in figures 4.7c, d and represent the two-dimensional (2D) electric potential and electric field distribution along the cross-section plane, corresponding to the profiles presented in figures 4.7a, b.

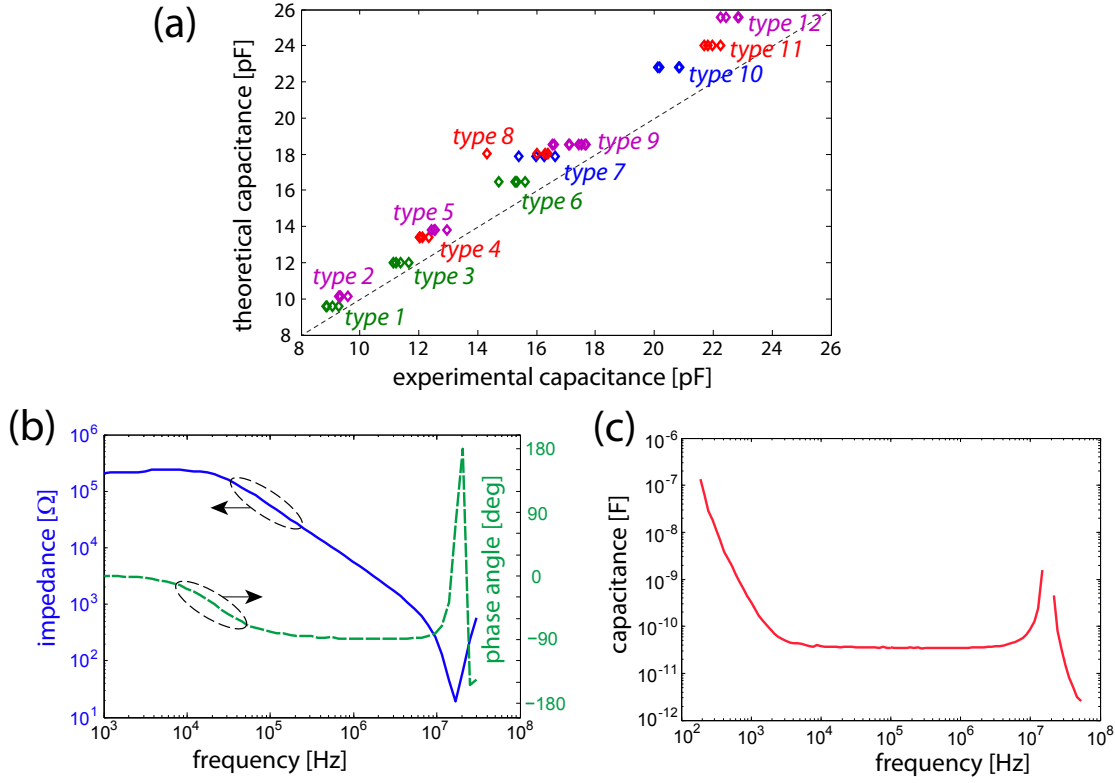


Figure 4.9: (a) Numerically simulated capacitance *vs* experimentally measured capacitance, in the absence of load, for all types of sensor designs referred in figures 4.2b, c. Colour enhancement for distinguishing different design types. (b, c) Frequency characteristics of the sensor’s capacitors: (b) impedance and phase angle, (c) capacitance derived from the imaginary part of the complex impedance.

The calculated theoretical values of the as-made capacitors are in the range of 10-25 pF, which is in good agreement with the experiments (figure 4.9a). A small deviation is due to the presence of parasitic capacitance arising from the measurement circuit and connection leads.

**Mechanical model of the 3-axial force sensor.** For the simulation of the sensor’s behavior upon applied load, we assumed a simplified linear elastic stress-strain model [201] as given by equation 4.3.

When normal compressive stress  $\sigma_z$  is applied to the sensor, the polymer dielectric compresses and the initial distance  $h_0$  between the electrodes decreases by  $\Delta h$ , and the Young’s modulus  $E$  of the polymeric material between the electrodes can be written as:

$$E = \frac{\sigma_z}{\epsilon_z} = \frac{F_z / A_0}{\Delta h / h_0} \quad (4.3)$$

### 4.3. Modeling and electro-mechanical characterization

with  $\epsilon_z$  the normal strain, and  $A_0$  the original area on which the normal force  $F_z$  is applied.

When shear stress  $\tau_x$  ( $\tau_y$ ) is applied to the sensor, it deforms from a rectangular prism into a parallelepiped by a transverse electrode displacement over  $\Delta x$  ( $\Delta y$ ), and the shear modulus  $G$  of the dielectric polymer can be written as:

$$G = \frac{\tau_{x(y)}}{\gamma_{x(y)}} = \frac{F_{x(y)}/A_0}{\Delta x(\Delta y)/h_0} \quad (4.4)$$

with  $\gamma_x$  ( $\gamma_y$ ) the shear strain resulting from the applied shear force  $F_x$  ( $F_y$ ).

The Young's and shear moduli values were set for the analysis as  $E_{PDMS} = 5$  MPa,  $G_{PDMS} = 900$  kPa, accounting for polymer hardening as caused by numerous lithography baking steps [202] and the presence of the thin Parylene-C layer.

For a full electro-mechanical analysis of the sensor, the FEM electrical model was combined with the calculations of deformation under applied stress.

#### 4.3.2 Electro-mechanical characterization of the 3-axial force sensor

Figures 4.9b, c show the electrical characterization of a typical single sensor in the absence of load, as obtained using an impedance analyzer (4294A, Agilent Technologies). The measured cut-off frequency of the device is 10 MHz and for all further electrical characterization of the capacitance, an out-of-resonance frequency of 1 MHz was chosen. Figure 4.9a presents the initial capacitance, derived from the imaginary part of the complex impedance<sup>c</sup>, for all types of sensor designs concerned in figure 4.2c.

Force sensing experiments were done with the measurement setup shown in figure 4.10. To apply a well-defined load, a motorized microstep  $z$ -stage (T-LSR150B, Zaber) was used in combination with a reference force gauge (Nano17, ATI Industrial Automation). The sensor was mounted vertically or horizontally, for normal ( $F_z$ ) and shear ( $F_x$ ,  $F_y$ ) force employment schemes, respectively. A dielectric polymethylmethacrylate (PMMA) plate of the size of the sensor's surface was placed between the latter and the force gauge, to uniformly apply the pressure over the surface of the device and to diminish the effects of conductive coupling with the environment and crosstalk of signal transmission circuits. Before the experiments, the sensors had been pre-loaded (14 N) to diminish for the presence of eventual material meta-stabilities, microcracks or irregularities, both in the polymeric and the electrode layers.

The electro-mechanical characterization of the sensors was carried out by measuring

---

<sup>c</sup>  $\Im(Z) = \frac{-1}{2\pi fC}$ , where  $f$  is the frequency and  $Z$  the impedance

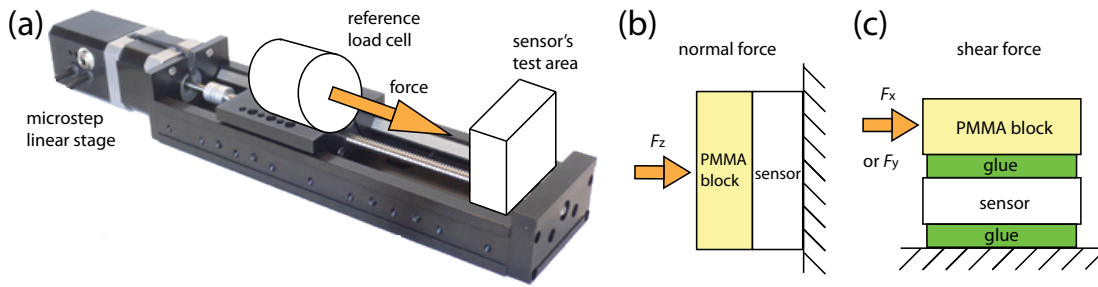


Figure 4.10: (a) Conceptual view of the experimental setup used for testing the force sensor. Configuration of the sensor in the setup for (b) normal and (c) shear force testing.

a response to a static uni-axial load in the 0-14 N force range. Thus pressure response was derived by simply dividing the force value by the sensor area (normal pressure  $\equiv$  normal force/sensor area; shear pressure  $\equiv$  shear force/sensor area). A settling time of  $\sim 10$  s was allowed between the application of the strain and the measurement of the sensor response to reduce the effect of polymer creep. In order to minimize errors in the measurements, the average value from 275 data points were taken by the impedance analyzer and the standard deviation from the mean value is reflected in the data of figures 4.11 and 4.13.

**Normal force measurements.** Figure 4.11 demonstrates the results of the measured capacitance *versus* applied compressive *normal* force  $F_z$  in the 0-140 kPa range, for the sensor of type 12 (see figure 4.2c). Sensor loading and unloading characteristics of four capacitors C1-C4 of the same sensor were obtained, revealing no hysteresis effect (figures 4.11a-d). A minor difference of initial capacitance value and capacitance change can be noticed between the four capacitors, most probably due to the geometrical design of the electrical leads.

Figure 4.11e shows this small spread in capacitance change values for the four capacitors. Figure 4.11f shows the normalized capacitances  $\Delta C_x/C_0$ ,  $\Delta C_y/C_0$ , and  $\Delta C_z/C_0$  derived from the data of figure 4.11e using equations 4.1 and 4.2.

The normalized  $z$ -sensing capacitance  $\Delta C_z/C_0$  *versus* pressure curve exhibits two distinct regions of elasticity, as if two elastic materials with different  $E$  were superposed in the dielectric stack. I think that the initial slope may be attributed to flattening of the rough surface of the top electrode during compression at low pressures (see figures 4.6f and 4.7b), as well as due to the change of the dielectric material constant  $\epsilon$  upon compression of the polymers. The normalized capacitance  $\Delta C_z/C_0$  shows a nearly linear behaviour over the 20-140 kPa range corresponding to compression of the bulk dielectric material. In this linear regime, the slope of the normal  $\Delta C_z/C_0$  *versus*  $P$  curve is given by  $1/E$  and is plotted in figure 4.11f.

### 4.3. Modeling and electro-mechanical characterization

**Shear force measurements.** Figure 4.12 characterizes the sensor (type 6, see figure 4.2c) in a *shear* force sensing scheme. The measured capacitance of the four unit capacitors of the same sensor *versus* an applied shear force  $F_x$  is shown in figure 4.12a. The  $x$ -shear-sensitive capacitors (C1, C3) respond to the applied pressure by decreasing (C1) and increasing (C3) the value of the capacitance. The response is linear over the whole measurement range. Simultaneously, in the absence of  $F_y$  shear,

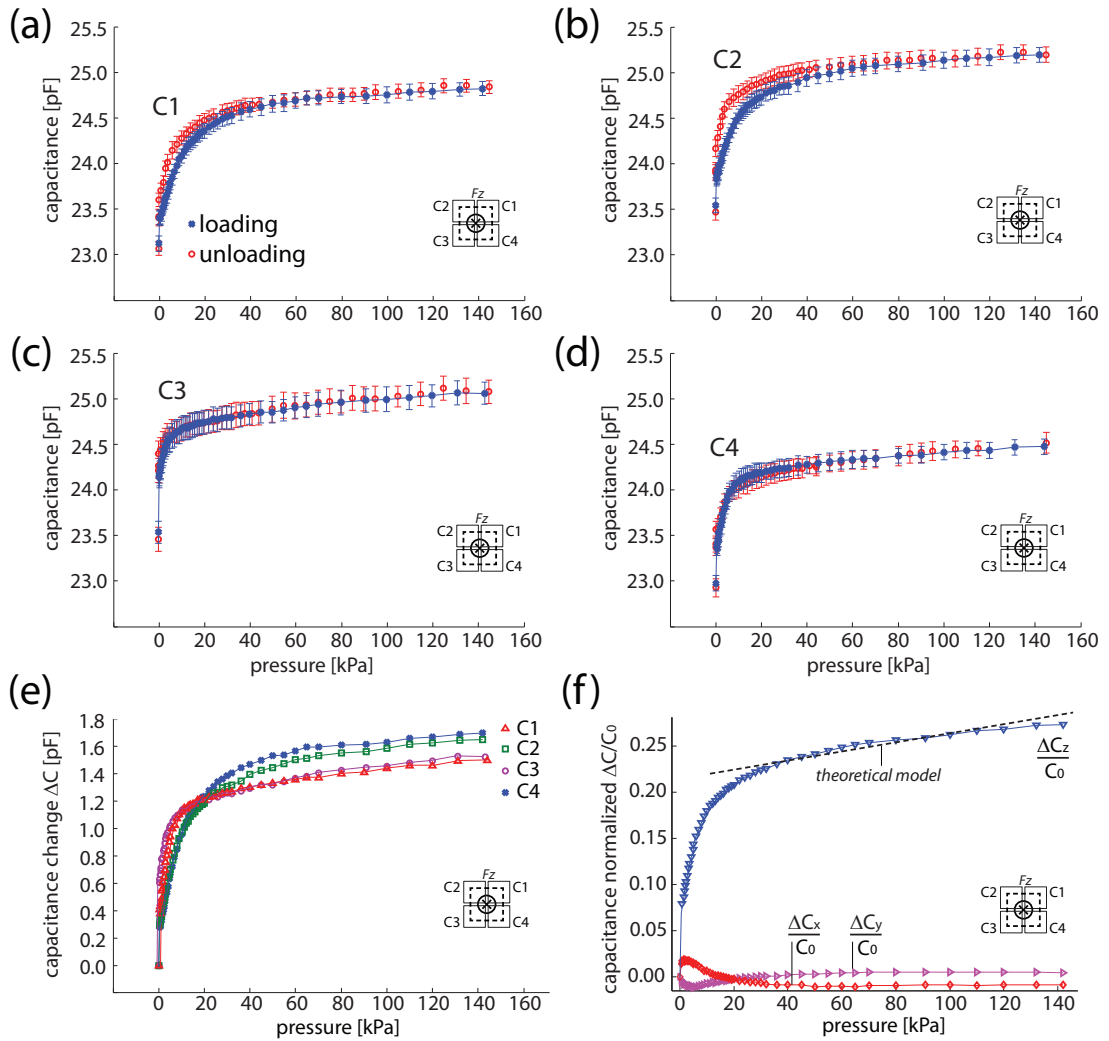


Figure 4.11: Measurement results upon compressive normal force  $F_z$  applied to the sensor. (a-d) Absolute capacitance *vs* applied compressive load for four capacitors (C1–C4) of the same sensor during loading and unloading cycles. (e) Variation in capacitance measured during loading experiments for the four capacitors. (f) The normalized capacitance differences  $\Delta C_x/C_0$ ,  $\Delta C_y/C_0$ ,  $\Delta C_z/C_0$  derived from the data in (e), and the theoretical prediction for  $\Delta C_z/C_0$ .  $C_0$ : initial load-free value for each capacitor.

## Chapter 4. Flexible capacitive sensor for three-axial force measurements

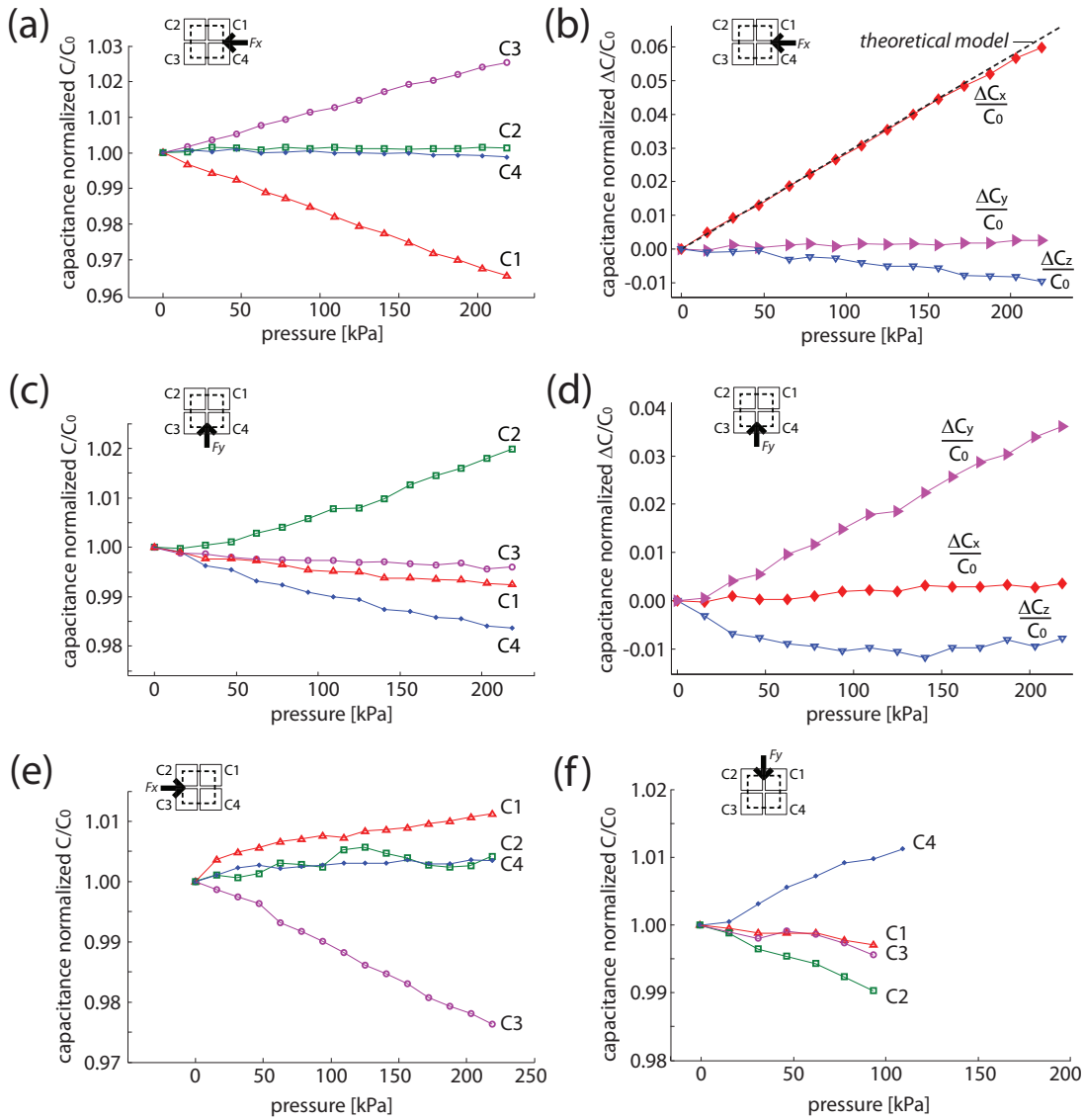


Figure 4.12: Measurement results obtained upon applying shear forces  $F_x$  and  $F_y$  to the sensor. (a) Normalized capacitance values of a sensor (C1-C4) and (b) the derived normalized capacitances  $\Delta C_x/C_0$ ,  $\Delta C_y/C_0$ ,  $\Delta C_z/C_0$ , as a function of applied shear pressure ( $\equiv$  shear force/sensor area) along the  $x$ -axis; in (b) with the theoretical prediction of  $\Delta C_x/C_0$ . (c) Normalized capacitance values of a sensor (C1-C4) and (d) the derived normalized capacitances  $\Delta C_x/C_0$ ,  $\Delta C_y/C_0$ ,  $\Delta C_z/C_0$ , as a function of applied shear pressure along the  $y$ -axis. (e, f) Measurement results obtained upon applying shear forces  $-F_x$  and  $-F_y$  to the sensor. Normalized capacitance values of a sensor (C1-C4) as a function of applied (e) shear pressure  $-F_x$  along the  $x$ -axis and (f) shear pressure  $-F_y$  along the  $y$ -axis.



### 4.3. Modeling and electro-mechanical characterization

the  $y$ -shear-sensitive capacitors (C2, C4) remain unresponsive.

The normalized  $x$ -,  $y$ -,  $z$ -sensing capacitances,  $\Delta C_x/C_0$ ,  $\Delta C_y/C_0$ , and  $\Delta C_z/C_0$ , corresponding to the results of figure 4.12a and derived from equations 4.1 and 4.2 are depicted in figure 4.12b. The normalized  $x$ -sensing capacitance  $\Delta C_x/C_0$  is in excellent agreement with the theoretical model. With shear force  $F_x$  applied to the sensor, the normalized  $x$ -sensing capacitance  $\Delta C_x/C_0$  increases, and in the absence of shear  $F_y$ , the normalized  $y$ -sensing capacitance  $\Delta C_y/C_0$  equals zero.

Figure 4.12c shows the measured capacitance of the four unit capacitors of the same sensor (type 7, see figure 4.2c) *versus* an applied shear force  $F_y$ . The  $y$ -shear-sensitive capacitors (C2, C4) respond to the applied pressure by decreasing (C4) and increasing (C2) the value of the capacitance. Simultaneously, in the absence of  $F_x$  shear, the  $x$ -shear-sensitive capacitors (C1, C3) remain unresponsive. The normalized  $x$ -,  $y$ -,  $z$ -sensing capacitances,  $\Delta C_x/C_0$ ,  $\Delta C_y/C_0$ , and  $\Delta C_z/C_0$ , corresponding to the results of figure 4.12c and derived from equations 4.1 and 4.2 are depicted in figure 4.12d. The results suggest that the sensor's response is quantitatively distinct in the two orthogonal shear directions. However, my analysis does not account for measurement setup misalignments, which would cause errors in the effective value and orientation of the applied load. In reality, application of a load that is perfectly parallel to the surface, without normal component, is experimentally very difficult, as may be clear from figure 4.12d. Therefore, figures 4.12c, d illustrate in fact the results of a case where a resultant force  $\vec{F} = \vec{F}_x + \vec{F}_y + \vec{F}_z$  is applied, consisting of a dominant  $y$ -shear ( $F_y \gg 0$ ) and a minor normal vector ( $F_z > 0$ ,  $F_x \approx 0$ ). Figures 4.12e, f show the measurement results when shear forces  $F_x$  (figure 4.12e) and  $F_y$  (figure 4.12f) are applied in an opposite direction (namely, the forces applied on the sensors are:  $-F_x$  and  $-F_y$ ), and for the sensors of type 8 and 7 (see figure 4.2c), respectively.

Finally, figure 4.13a shows the output value of capacitor C3 of a sensor (type 6, see figure 4.2c), measured during three consecutive loading cycles in the  $x$ -direction. The overlapping curves indicate that the operation in 0-220 kPa range is in the polymer's elastic regime, without occurrence of plastic deformation and memory effects. The figure 4.13a presents also the absolute capacitance *versus* applied shear load  $F_x$  for capacitors C1, C2 and C4 of the sensor in a single loading cycle. Figure 4.13b shows the capacitance change for the two  $x$ -axis-sensitive capacitors C1 and C3 of the same sensor *versus* applied shear load  $F_x$ , during a loading and unloading cycle, disclosing no appreciable hysteresis effects.

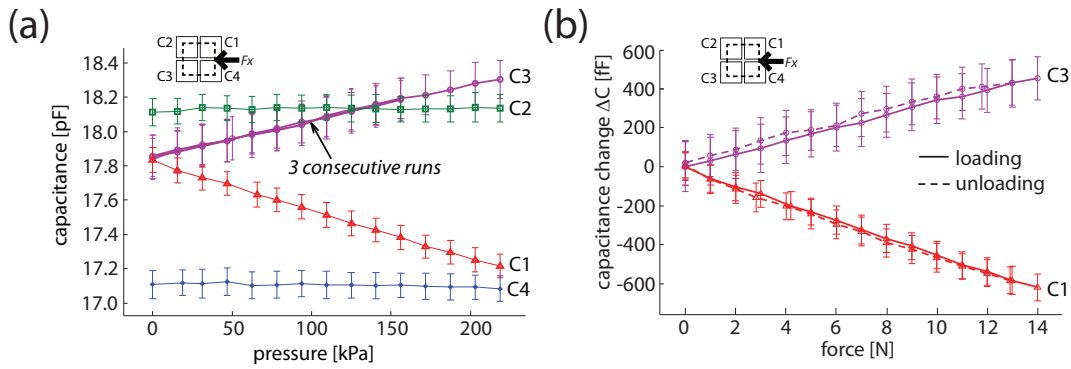


Figure 4.13: (a) The effect of three consecutive loading cycles of the sensor; the capacitance of the four capacitors is plotted *vs* the applied shear pressure. The overlapping curves indicate the repeatability of the sensor’s response. (b) Capacitance change *vs* applied shear load  $F_x$ , for two  $x$ -axis-sensitive capacitors (C3, C1) of the same sensor, during loading and unloading cycles.

#### 4.4 Comparison between the sensitivity of the force sensor and the touch sense of human skin

In figure 4.14 the sensitivity values of typical sensors, obtained by applying normal and shear force, respectively, are compared with the usual values of 3-axial forces, existing when a human hand or foot is in contact with an object.

In the *normal*  $z$ -direction, the sensor’s sensitivity  $S_z$  is pressure-range dependent (see discussion of figure 4.11f): a region of increased sensitivity ( $S_z = 2.4\% \text{ kPa}^{-1} \equiv 563 \text{ fF/kPa}$ ) is observed for loads of 0-1 N (0-10 kPa), and a region of decreased sensitivity ( $S_z = 0.066\% \text{ kPa}^{-1} \equiv 15.4 \text{ fF/kPa}$ ) for loads of 1-14 N (10-140 kPa).

On human hand skin, normal pressures of 2.5-150 kPa correspond to a range from gentle touch [33] to a strong grasp [28, 34], while typical normal pressures on the foot are 15-200 kPa [38–40], placing the sensitivity of our sensors exactly in the range of interest, as indicated in figure 4.14a.

Moreover, the increased sensitivity observed at pressures  $<10$  kPa is majorly desirable in real-world applications, especially for tactile sensing, *e.g.* by fingertips. That is, high sensitivity is required at soft touch, to reflect the ability of fine touch perception by human skin and provided with Merkel and Meissner’s mechanoreceptors, which are located near the surface of the skin (see section 2.1). On the other hand, such sensitivity is not demanded at higher loads, instead, a wide range of forces should be detectable, to reflect the ability of pressure perception on human skin by Pacinian and Ruffini mechanoreceptors, buried deep inside the skin tissue [19–21].

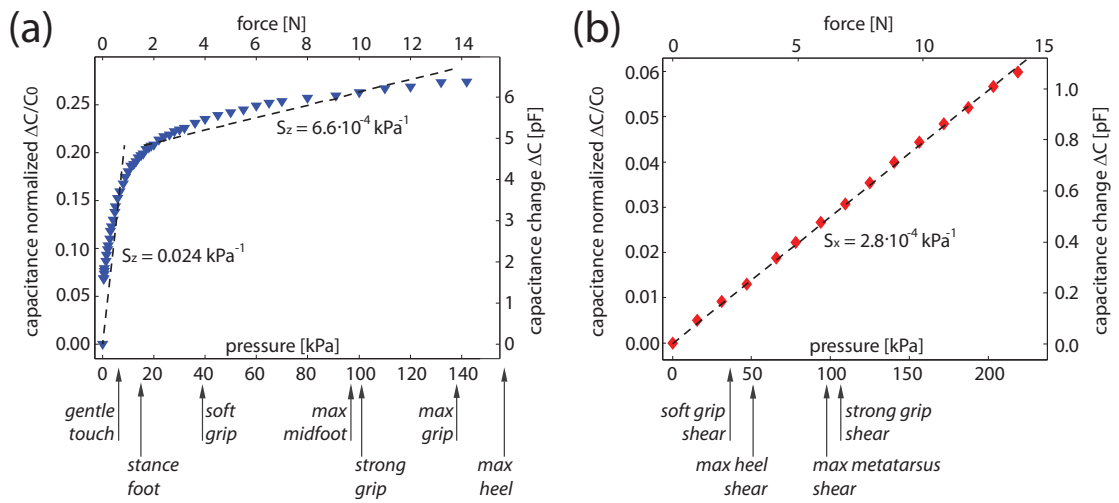


Figure 4.14: (Normalized) capacitance-force/pressure response curves. (a) Normal force sensing data taken from the  $\Delta C_z \setminus C_0$  data of figure 4.11f, (b) Shear force sensing data taken from the  $\Delta C_x \setminus C_0$  data of figure 4.12b. For each curve, the sensitivity slope is presented. Also literature-reported pressure ranges for typical normal and shear forces applied during hand and foot skin contact are indicated [28, 33, 34, 38–40].

For *shear* force detection, the  $x$ -sensing capacitance defines a sensor sensitivity  $S_x = 0.028\% \text{ kPa}^{-1}$  ( $\equiv 5 \text{ fF/kPa}$ ). Typical hand grip shear forces are in the range of 40-100 kPa [28], while the maximum shear force under the foot can reach 50-90 kPa [39, 40], placing the sensitivity of our sensors exactly in the range of interest, as indicated in figure 4.14b.

Hence, the 3-axial sensitivity of my sensor resembles that of human skin in the hand and feet areas, and I anticipate that such a sensor has promise for artificial skin applications.

## 4.5 Summary and discussion

A fully flexible, capacitive force sensor for 3-axial force measurements has been developed, by integrating microfabrication technology of three polymers, PI, Parylene-C, and PDMS, with standard metallization processes. The sensor's capacitance and its 3-axial force sensitivity was theoretically modelled. The experimental capacitive values were in agreement with theoretical predictions. The electrical characterization of the capacitors demonstrated static capacitances in the range of 20 pF. The sensor exhibited linearity and absence of hysteresis, when operated in the range of 0-14 N for 3-axial loads. The electro-mechanical characterization of the capacitors revealed in the normal direction a sensitivity  $S_z = 0.024 \text{ kPa}^{-1}$  for pressures <10 kPa, whereas for

## Chapter 4. Flexible capacitive sensor for three-axial force measurements

---

higher pressures the measured sensitivity  $S_z = 6.6 \cdot 10^{-4} \text{ kPa}^{-1}$ . Typical measured shear force sensitivity  $S_x = 2.8 \cdot 10^{-4} \text{ kPa}^{-1}$ . The sensor was flexible, pliable and capable of being shaped to adapt to non-planar surface conditions.

In the measurements, a settling time was allowed between the application of the stress and measurement of the sensor response, to mitigate the effect of PDMS creep and stress relaxation and thus minimize the problems associated with polymer's visco-elastic behaviour. For future dynamic sensing, these nonlinear time-dependent effects would need to be studied in detail. Microstructuring the thin PDMS films could provide one solution to reversibly store and release the energy, diminishing visco-elastic creep [77]. For long-term use, when repeated loading and unloading cycles are projected, fatigue tests of the sensors should be conducted, considering the foreseen stress levels, frequencies and impulse time lengths of an applied load [162].

## 5 Flexible films with custom-designed microporosity

---

This chapter describes a microfabrication process for the realization of foam-like polyimide films with custom-designed microporosity. The mechanical stress-strain properties of the microcavities were modeled. Furthermore, nanoindentation and microcompression experiments of the foam-like layers are presented.

---



Adapted from the journal article [203]:

*Polyimide foam-like microstructures: technology and mechanical properties*  
(2011) **Dobrzynska J A**, Joris P, Jiguet S, Renaud P, and Gijs M A M,  
Journal of Micromechanics and Microengineering **21**(10)105016  
DOI: 10.1088/0960-1317/21/10/105016

### 5.1 Introduction

Human sense of touch perceives stimuli through a large number of mechanoreceptors that are distributed on the skin [20]. Our halluces, soles, palm, calves and thighs provide less cutaneous feedback when compared with cheek, nose, forehead, lips or back [19], while foot heels have substantially no touch perception but are very sensitive to vibrations [37]. The tactile sensibility depends on the density of the receptive units responding to skin deformation. For instance, our fingertips are more sensitive than the palm, since they hold 241 mechanoreceptors per  $\text{cm}^2$ , in contrast to a palm with only 58 of them [32].

Mimicking human cutaneous sensors for robotic tactile sensing extends beyond hand- and feet-areas to the whole body covered with an artificial skin. Just as human skin has diverse sensitivity regions (see figure 5.1), in an artificial skin, the spatial resolution, the number of sensing elements, and the sensitivity of the tactile sensors should depend on the body site where they are intended to be placed [22]. The development of such large-area artificial skins with varied touch-sensitive regions faces the need for suitable fabrication technologies and *new flexible materials*.

A variety of *foams* is used on a daily basis as flexible materials. Foamy marine animals are used as soft bath sponges [204]. Neoprene dry suits, containing millions of tiny enclosed air bubbles, provide body-adaptable thermal insulation for water sports enthusiasts, while in plastic surgery, various polymeric foams have been used for first-generation breast implants [205]. In microelectronic devices, foamed polymers are used as materials with very low dielectric constants [206]. Indeed, solid foams form an important class of light-weight, low-density and compressible cellular engineering materials.

By controlling and tailoring the porosity of the solid foam, the compressive properties within the volume and on the surface of such a material can be adjusted (see figure 5.1), giving therefore rise to potential for new applications. Foamy layers with custom-designed porosity can find possible implementation in capacitive force sensing applications as a cellular dielectric [207], where one requires dielectric materials with adjustable elasticity<sup>a</sup> and thin flexible suspended dielectric layers [79, 165–167].

This chapter discourses the state of the art in fabrication technology of polymeric foams. Further, I introduce a fabrication technology of a novel polymeric foam-like material, and discuss its mechanical properties. I modelled the mechanical stress-strain properties of the microcavities using both an analytical model and the Finite Element Method (FEM). Finally, I compare the simulation data with the results of

---

<sup>a</sup>provided the overall sensor size is much larger than the typical cavity size

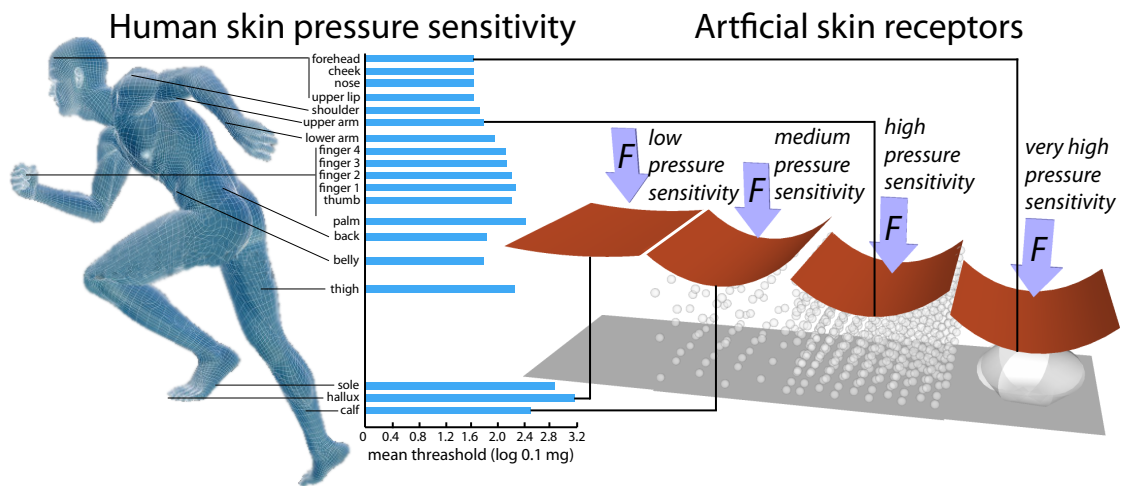


Figure 5.1: Concept of a foam-like material, in application to a pressure-sensitive sensor. Sensitivity to pressure at different sites on the body (left) can be artificially mimicked by incorporating into a pressure-sensitive sensor a variety of air-cavities (right). Air-bubble-filled polymer deforms more than the bulk, under the same applied load. The more/larger cavities inside the polymer volume, the more compressive the material. The body pressure-sensitivity diagram adapted from [19, 208].

nanoindentation and microcompression experiments.

## 5.2 Polymeric foams

Polyurethanes or silicones are typical materials used in artificial foams. However, only few polymers are compatible with microelectronic fabrication technology. Polyimides (PI) have emerged as a favoured class of microtechnology-compatible materials, due to their excellent processability, good planarization properties, low thermal expansion, chemical resistance, and desirable adhesion properties to many layers, including metals and PI itself. Moreover, they present high wear-resistance, high mechanical strength, and a low dielectric constant [209].

Polymeric foams have been produced by using advanced chemical processes, involving dissolution of foaming agents, bubble nucleation and growth, and stabilization [210]. Nanofoams from PI have been synthesized using copolymers with microphase separated morphologies, which have been selectively removed by thermal treatment leaving voids in the nanometer range [211]. PI macrofoams have been produced by reacting a derivative of a dianhydride with a diamine [212]. However, the reported chemical methods affect only the bulk material properties and do not allow local or selective control of porosity, *i.e.* one cannot define the size and shape of the

foam cells.

Microfabrication methods are more suitable in this regard, as microcavities and microchannels can be custom-built. One convenient physical approach to microchannel formation proposed by Hirai *et al.* relies on a SU-8 negative photoresist (PR) fabrication technique, using dissolution of the uncross-linked PR through a permeable membrane [213, 214]. Also, selective ion irradiation [181] can result in nanoporous PI membranes. Metz *et al.* proposed PI-based thin microfluidic channels, which were produced by the lamination technique [215], but PI adhesive bonding suffers from film non-uniformity and void generation problems [216]. Finally, physical techniques for manufacturing micro-air structures, including the use of sacrificial materials, have been extensively studied by the Kohl group [217–225]. Based on this concept, single-layer microchannels and micro-scaled sealed cavities in PI have been reported by several authors [217, 221, 226].

Fabrication of air-void filled PI, based on decomposition of sacrificial microstructures, requires the choice of the proper sacrificial material. Removal of material by solvents in wet etch processes is time-consuming [227] and does not allow for fabrication of closed-cell structures [162]. Hence, encapsulated decomposable microstructured materials are favoured, whose decomposition products easily permeate the PI. In particular, some heat-depolymerizable materials decompose at elevated temperatures into out-diffusing volatile small molecule compounds. Poly (propylene, ethylene, cyclohexane) carbonates [218, 221, 225, 226], dendritic hyperbranched polymers (HBP) [228], polynorborenes (PNB) [217, 220, 221, 223], and tetracyclododecenes (TCD) [223, 224] have been used for this approach. They can be structured by electron beam lithography [229], dry etch [225, 226] or conventional lithography methods [219, 223]. Most of those materials, however, are not compatible with PI-overcoat processes because of a high decomposition temperature, and a high solubility of the sacrificial material in the PI's solvent. Indeed, HBPs [228] require a temperature of 600°C to decompose completely, whereas PBN- and TCD-based materials [223] require temperatures reaching 450°C. The process of imidization of PI requires usually temperatures between 300-350°C, whereas extensive heating can result in the degradation of PI and thermal instability<sup>b</sup> [209, 230]. PI air cavities fabricated based on sacrificial PNB were reported [217], but the effect of high temperature film heating and the material's final mechanical properties were not addressed. In contrast, polycarbonates undergo thermal decomposition at lower temperatures, which is safer for the PI. In order to fully decompose, polypropylene carbonate (PPC) is known to require temperatures of 300°C [231], whereas polyethylene carbonate (PEC) decomposition requires heating up to 210°C [218].

---

<sup>b</sup>here stability is understood as the ability to retain weight at elevated temperature



### 5.3. Microfabrication process of foam-like PI films

---

Yet, polycarbonates exhibit very high solubility in the main component of the PI's precursor, N-Methyl-2-pyrrolidone (NMP), the latter representing up to 90% of the weight [178]. Although microfabrication of cavities in PI based on PPC sacrificial material was reported [226], it was a delicate process. A more universal approach, allowing to combine any sacrificial material with any polymer overcoat was proposed by Joseph *et al.* [221]. A barrier layer of silicon dioxide (SiO<sub>2</sub>) was incorporated in-between the two polymeric layers to prevent solvent-incompatibility problems. A silicon nitride (SiN) encapsulation layer [217] was used for a similar application.

In this thesis, a new approach for the controlled microfabrication of PI foam is introduced. The inclusion of microcavities in the PI layers allows reducing their elastic modulus while maintaining the advantageous properties of the material. I report the development of custom-designed foam-like microstructures composed of PI layers with air bubbles at predetermined positions, which are formed on silicon substrates by heat-depolymerization of PPC sacrificial microstructures. The PPC exhibits a relatively low decomposition temperature, which does not degrade PI, is commercially available, cheap, and easily processable.

### 5.3 Microfabrication process of foam-like PI films

The process flow for the fabrication of foam-like PI layers is illustrated in figure 5.2b. In my process, high void packing densities were realized. Namely, the whole surface of a 4-inch wafer was densely covered with  $5 \times 5 \text{ mm}^2$  void areas, which were completely filled with structures of the geometry and dimensions as presented in figure 5.2a. The main fabrication steps of the microcavities in PI were deposition and structuring of PPC as a sacrificial layer, deposition of an aluminium (Al) barrier layer, and deposition of PI on top of PPC, curing of the PI and depolymerization of the PPC.

#### 5.3.1 Sacrificial material coating

In my optimized process, PPC (Empower Materials) of molecular weight (MW) 265 000 was dissolved in NMP (Acros), resulting in 20 wt.% or 30 wt.% solutions. The material's MW (different tested MWs are listed in table 5.1), concentration of the solution and type of the solvent used were found to have influence on unwanted bubble formation during the spin-coating and soft-bake processes.

My process started by spin-coating a 20  $\mu\text{m}$  thin film of PPC onto a silicon wafer (figure 5.2b-i). Bubbles were removed from the film by putting the wafer into a vacuum chamber (300, PVA TePla) for 1 min before the hot plate bake. Soft-baking was

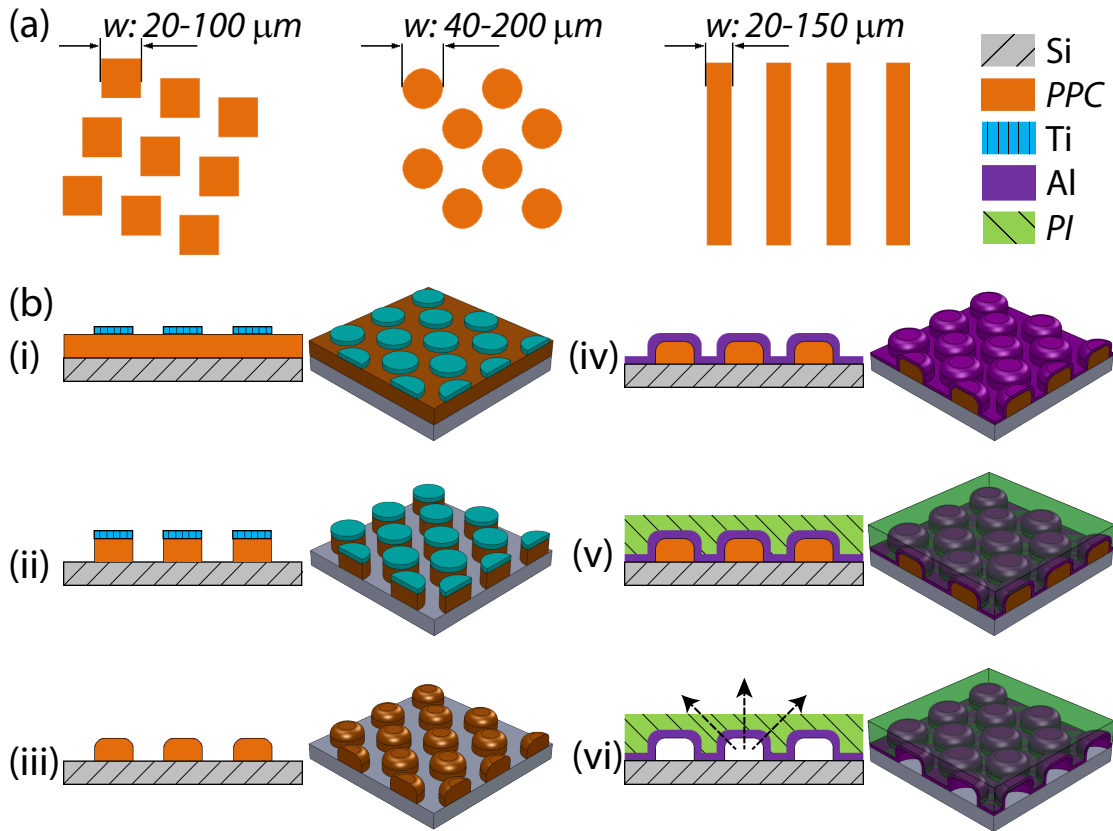


Figure 5.2: Fabrication of the microporous PI layer. (a) Square, circle and line-type mask patterns are employed to realize PPC structures, that later will form the micro-cavities. (b) Technological process flow: (i) spin-coating of sacrificial PPC, deposition and structuring of the Ti mask, (ii) PPC dry etching, (iii) PPC reflow, (iv) deposition of the Al barrier layer, (v) PI spin-coating, (vi) final bake to polymerize the PI and decompose the sacrificial PPC.

performed on a hot plate under a fume hood to remove the solvent from the film (RC8 THP, Karl Süss). The wafer was heated from  $50\text{ }^{\circ}\text{C}$  to  $150\text{ }^{\circ}\text{C}$  at a constant rate of  $2\text{ }^{\circ}\text{C}\cdot\text{min}^{-1}$ . The final temperature was kept for 1 h, after which the wafer was allowed to cool down to ambient temperature (LSM-200, Sawatec).

### 5.3.2 Mask deposition

A 50 nm Ti layer was deposited by physical vapour deposition (PVD) as the mask for the PPC etching (figure 5.2b-i). In this thesis, two distinct Ti deposition and structuring techniques were considered. The first one was room temperature (RT) sputtering (Spider 600, Pfeiffer), followed by conventional photolithography and wet etching of Ti in hydrofluoric acid (HF). The second one implied the use of a stencil shadow mask

### 5.3. Microfabrication process of foam-like PI films

Table 5.1: Test results for different sacrificial PPC and PI overcoat layers: dissolution<sup>a</sup>, and collapse<sup>b</sup>, can be avoided by using an Al barrier layer between the PPC and the PI.

PPC (MW)	No barrier layer between PPC and PI		Al barrier layer between PPC and PI	
	Dissolution <sup>a</sup>	Collapse <sup>b</sup>	Dissolution <sup>a</sup>	Collapse <sup>b</sup>
178–197 k	Y	Y		
222.9 k[226]	P	P	N	N
226–230 k	Y	Y	N	N
265 k	P	Y	N	N

<sup>a</sup> Premature dissolution of PPC in the PI.

<sup>b</sup> Collapse of the PI membrane over the to-be-formed air microcavity.

Y = yes; N = no; P = partial.

for the RT deposition of 50  $\mu\text{m}$  Ti by evaporation (LAB 600H, Leybold Optics). The latter neither required photolithography nor wet etching of the metal to obtain the Ti mask.

Silicon nitride membranes [232] were used for the fabrication of stencil chips with structural features in the nano- to micrometer-scale. For larger size microstructures ( $>40 \times 40 \mu\text{m}^2$ ) I used a stencil manufactured from a 380  $\mu\text{m}$  thick Si wafer, which had been etched anisotropically by deep reactive ion etching (DRIE) using the Bosch process (601E, Alcatel).

The combination of evaporation with stencil lithography led to excellent results, and the surface obtained using Ti evaporation was smooth (figure 5.3a). Since the stencil had directly provided a structured mask over the PPC, subsequent photolithography and related procedures were not necessary. The topography variation of the mask layer was in the range of 300 nm over a large area (figure 5.3b) (as measured by optical profiling system Wyko NT1100, Veeco). With this masking technique,  $5 \times 5 \mu\text{m}^2$  PPC microstructures were easily obtained (figure 5.3c). Thicker metal layers were found leading to cracks over the wafer surface.

#### 5.3.3 Sacrificial material etch

Next, the PPC was patterned *via* oxygen plasma etch in an inductively coupled plasma (ICP) system at 1000 W, with constant etch rate of  $2 \mu\text{m} \cdot \text{min}^{-1}$  (figure 5.2b-ii) (Multiplex ICP, STS). The remaining Ti mask was then removed in an HF bath for 40 s, resulting in matrices of structured channels and dots in PPC.

Figures 5.3d-f show scanning electron microscope (SEM, Carl Zeiss) images of the

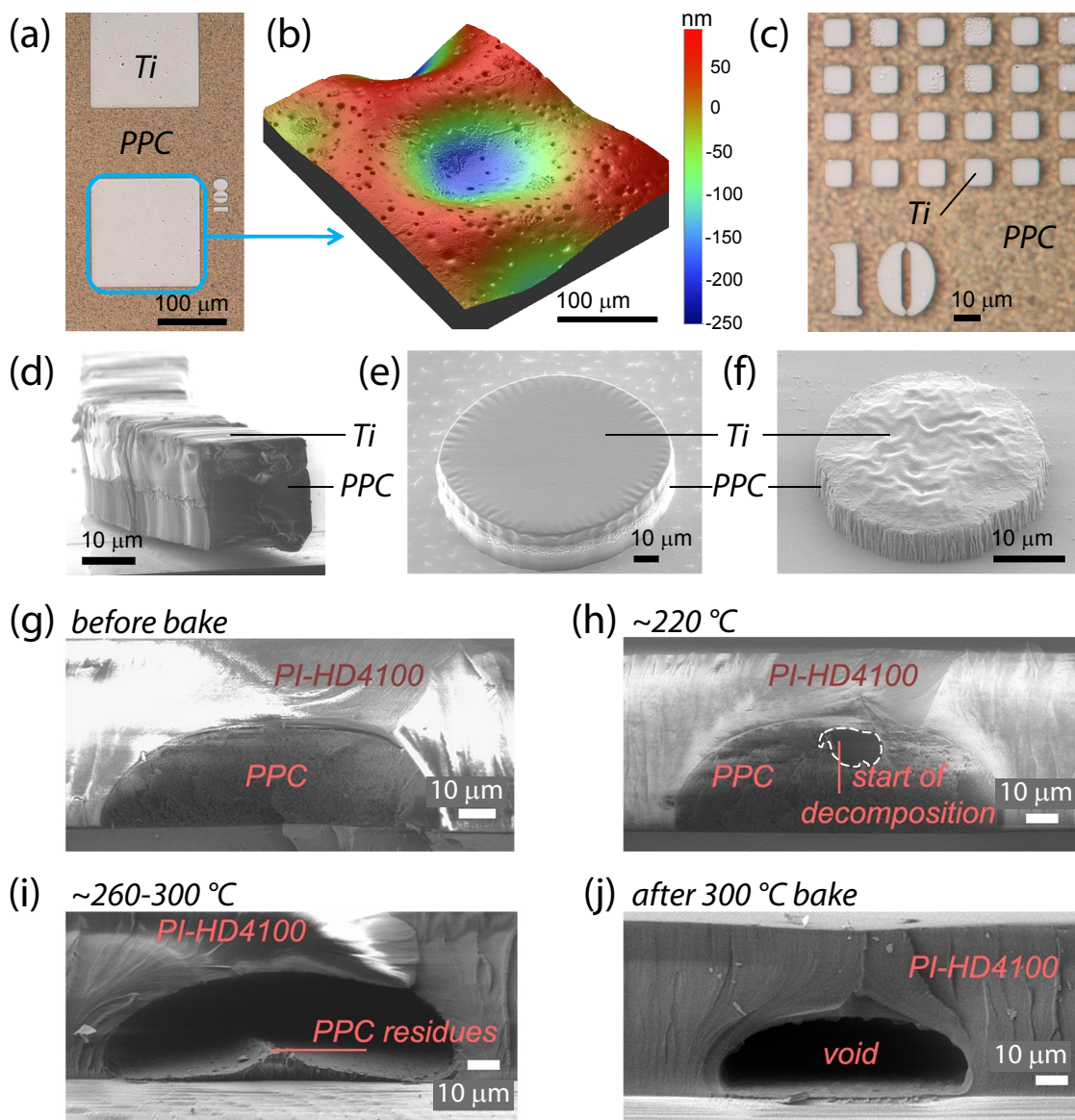


Figure 5.3: (a–c) Ti evaporated through a stencil mask on a PPC layer: (a) optical microscope photograph of smooth surfaces obtained with this technique; (b) optical profilometer image for part of the area of the Ti mask surface, revealing a thickness variation of less than 300 nm; (c) optical microscope photograph of smaller Ti mask structures. (d–f) SEM images of anisotropically etched PPC: (d) cross-section view showing the 1:1 aspect ratio; (e) flat PPC surface after etching using a stencil mask; (f) wrinkled surface and irregular edges of an etched PPC microstructure realized using a sputter-deposited Ti-mask and standard lithography. (g–j) Process of decomposition of sacrificial PPC: (g) as-made PPC encapsulated in a PI layer; (h) PPC starting to decompose at ~220 °C; (i) the PPC decomposed at ~260–300 °C leaves a cavity in the PI layer, some PPC residues remaining inside the void; (j) completely decomposed PPC creates a complete void in the PI, after a 300 °C bake.

### 5.3. Microfabrication process of foam-like PI films

---

PPC patterns obtained after the etching steps. The dry etch was highly anisotropic, allowing to obtain structures with vertical sidewalls and no mask undercut, with an aspect ratio of 1:1 (figure 5.3d). Figure 5.3e corresponds to a microstructure realized with an evaporation stencil-deposited Ti mask, which resulted in a flat and smooth surface of the PPC surface, and a precise circular pattern.

#### 5.3.4 Al barrier layer and PI overcoating

After the etch, the wafers were placed on a hot plate at 100 °C for 10 min to reflow the PPC (RC8 THP, Karl Süss), in such a way that smooth slopes were obtained (figure 5.2b-iii). Consequently, the tapered PPC slopes allowed conformal metallization by a 600 nm Al layer, deposited *via* PVD RT sputtering (figure 5.2b-iv) (Spider 600, Pfeiffer).

The advantage of using an Al layer in contrast to other inorganic barrier layers proposed [217, 221] is that it can be deposited at RT, which keeps the sacrificial material thermally stable. Moreover, Al exhibits a good adhesion to polymeric surfaces. At the same time, a thin and ductile Al layer did not influence the elasticity of the finally realized foam-like layers. In contrast, high-stress and brittle SiO<sub>2</sub> and SiN layers deposited at temperatures above 100 °C during plasma-enhanced chemical vapour deposition (PECVD) [233] seriously affect the meta-stable PPC material with a low glass transition temperature ( $T_g \sim 40$  °C), enhancing cracking of the barrier layer.

The process continued by the deposition of a 20 μm layer of PI (figure 5.2b-v). Since PPC exhibits very high solubility in the solvent of the deposited PI precursor, a low-NMP-content precursor was used, namely photosensitive HD-4100 (HD Microsystems) [178]. The PI spin-coating was done very rapidly, and using dynamic dispense, decreasing the contact time of the NMP solvent with the PPC.

PI was dynamically dispensed in the following way: the initial rotation speed of 500 rpm was accelerated with a 100 rpm·min<sup>-1</sup> rate to the final speed of 1300 rpm, at which it was spun for 13 s for PR thinning (LSM-200, Sawatec). The Al barrier layer served at this point of the process as a physical barrier for the penetration of the NMP solvent into the PPC microstructures.

Finally, the PI-coated wafer was placed on a hot plate at 110 °C and prebaked for 10 minutes for the evacuation of the solvent under a fume hood, and was subsequently cooled down to RT. In the next step, the sample was flood UV-exposed with a broad-band spectrum (300-440 nm), with a dose of 3 J·cm<sup>-2</sup> to initiate the cross-linking of the PI (MA6, Karl Süss).

## Chapter 5. Flexible films with custom-designed microporosity

Table 5.2: Furnace baking steps for PPC decomposition and PI polymerization.

Baking step	T <sub>start</sub>	Ramping	T <sub>stop</sub>	Time	Gas environment	Process
1	50 °C	0.25 °C·min <sup>-1</sup>	200 °C		O <sub>2</sub>	partial
2	200 °C	-	200 °C	1 h	N <sub>2</sub>	polymerization
3	200 °C	cool down <sup>a</sup>	RT		O <sub>2</sub>	of PI
4	50 °C	10 °C·min <sup>-1</sup>	300 °C		N <sub>2</sub> > 200 °C	decomposition
5	300 °C	-	300 °C	3 h	N <sub>2</sub>	of PPC and full
6	300 °C	cool down <sup>a</sup>	RT		N <sub>2</sub> > 200 °C	polymerization
						of PI

<sup>a</sup> Cool down by natural oven convection.

### 5.3.5 Baking steps for PPC decomposition and PI polymerization

Next, the wafer underwent several furnace-heating steps (figure 5.2b-vi and table 5.2). Figure 5.4a demonstrates the differential scanning calorimetry (DSC) results (Mettler-Toledo, DSC-25) of the PI HD-4100. Three peaks associated with polymerization are noticeable at temperatures around 130 °C (A), 170 °C (B), and 240 °C (C). To exploit this polymerization behaviour, the previously processed wafer was subjected to the following baking step. It was placed in a furnace at 50 °C, the temperature was ramped up with 0.25 °C·min<sup>-1</sup> and held at 200 °C for 1 h in O<sub>2</sub> environment (T6060, Heraeus). During this process, the PPC did not undergo thermal decomposition, but partial polymerization of the PI overcoat layer was obtained.

Indeed, figure 5.4b shows the thermal gravimetric analysis (TGA) results (Mettler-Toledo, TA-11) of PPC of MW=265 000, indicating the thermal decomposition at temperatures between 200 °C and 300 °C, in nitrogen and oxygen environments. During decomposition in nitrogen, the PPC binder decomposes by pyrolysis *via* a depolymerization mechanism into a propylene carbonate liquid [231] (figure 5.4c), a highly polar solvent, which evaporates without leaving residual carbon. During thermal decomposition in an oxygen atmosphere, the PPC binder produces carbon dioxide and water (figure 5.4d).

Therefore, for a subsequent baking step, I chose a temperature of 300 °C, at which there is simultaneous PPC decomposition and PI polymerization. The time of 3 h was needed for a final cure of the PI and complete decomposition of the PPC. Figure 5.4e gives the indication of the typical temperature profile adapted during our baking process and shows the corresponding TGA results of a PI layer.

The use of the thin Al layer was crucial: being deposited for forming a barrier between the solvent-containing PI and PPC layers during spin-coating, in the baking

### 5.3. Microfabrication process of foam-like PI films

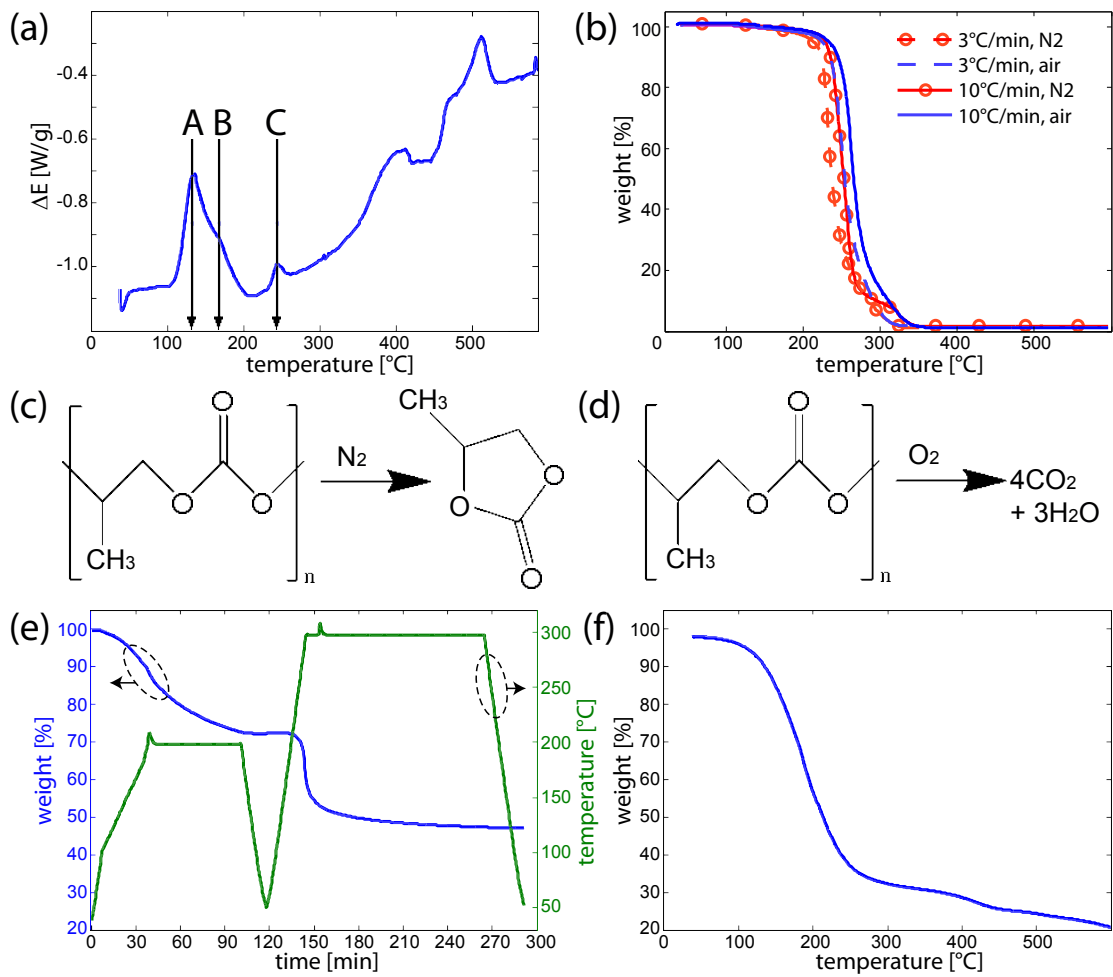


Figure 5.4: (a) DSC of UV-exposed PI-HD4100 heated at a rate of  $10\text{ }^{\circ}\text{C}\cdot\text{min}^{-1}$ , in nitrogen flow, showing three polymerization-associated peaks: (A) around  $130\text{ }^{\circ}\text{C}$ , (B) around  $170\text{ }^{\circ}\text{C}$  and (C) around  $240\text{ }^{\circ}\text{C}$ . (b) TGA curves of PPC 265 k, at two different heating rates of 3 and  $10\text{ }^{\circ}\text{C}\cdot\text{min}^{-1}$ , in air and under nitrogen flow. Mechanism of PPC's decomposition (c) by pyrolysis in nitrogen environment, (d) by combustion in oxygen environment. (e) TGA of UV-exposed PI-HD4100: a softbake at  $200\text{ }^{\circ}\text{C}$  is followed by temperature lowering for stress relaxation, which is subsequently followed by polymerization at  $300\text{ }^{\circ}\text{C}$ . (f) TGA of UV-exposed PI-HD4100: performed without softbake, at a heating rate  $10\text{ }^{\circ}\text{C}\cdot\text{min}^{-1}$ , under nitrogen flow. The analysis illustrates the removal of solvents ( $\sim 70\%$ ) in the polyimide mixture below  $300\text{ }^{\circ}\text{C}$ , and the degradation of the material above  $400\text{ }^{\circ}\text{C}$ .

process, it was permeable to the gaseous reaction products originating from the PPC decomposition. At the same time, the Al barrier layer provided a certain rigidity of the microporous PI, preventing collapse of the PI membranes after void formation.

Figures 5.3g-j illustrate the mechanism of void formation in the PI layer at various stages of furnace bakes. Only after the bake at a temperature of 300 °C, the completely decomposed PPC created a void in the PI film, which is cleared from residues (figure 5.3j). In my decomposition-cure process, I did not exceed a temperature of 300 °C, and therefore did not compromise the mechanical properties of the PI film [230]. The TGA of the PI HD-4100 suggests a beginning of the material's thermal degradation only above 400 °C indeed (figure 5.4f).

My optimized multiple-step baking process fully exploited the PI's curing properties and the PPC's decomposition behaviour, and released the stresses inside the PI overcoat layer.

### 5.3.6 Optical inspection of the fabrication process results

Figures 5.5a, b show SEM images of the manufactured arrays of microcavities of two different sizes in a PI film. The obtained void fraction with a single cavity layer corresponds to 20-30%.

Figure 5.5c is an example of a double-layer process. The different appearance between the first and second levels of voids may give the false impression that processing sequences were different. However, the second-layer microcavities can be simply obtained by repeating the fabrication steps (figure 5.5b-i to -vi) without modifications to the process. The reason for the difference in the sidewall profile of the cavities obtained in the second level is due to the PPC reflow step (figures 5.5b-iv). Before the deposition of the Al barrier layer, the PPC was reflowed to allow the conformal metallization of its surface. The contact angle of liquified PPC was bigger on silicon substrate (first level) than on PI (second level).

Figure 5.5d is a zoom into the rectangular area of figure 5.5c. The highest obtained aspect ratio for the microcavities without collapse was 15:1 (figure 5.5e).

### 5.3.7 Notes on the process

Although the process seems straightforward and simple, a lot of challenging issues had to be faced, in particular (i) masking and patterning of PPC, (ii) PPC dissolution during spin-coating and (iii) microcavity collapse during hardbake. Therefore, it is worth discussing in more detail these critical issues.



### 5.3. Microfabrication process of foam-like PI films

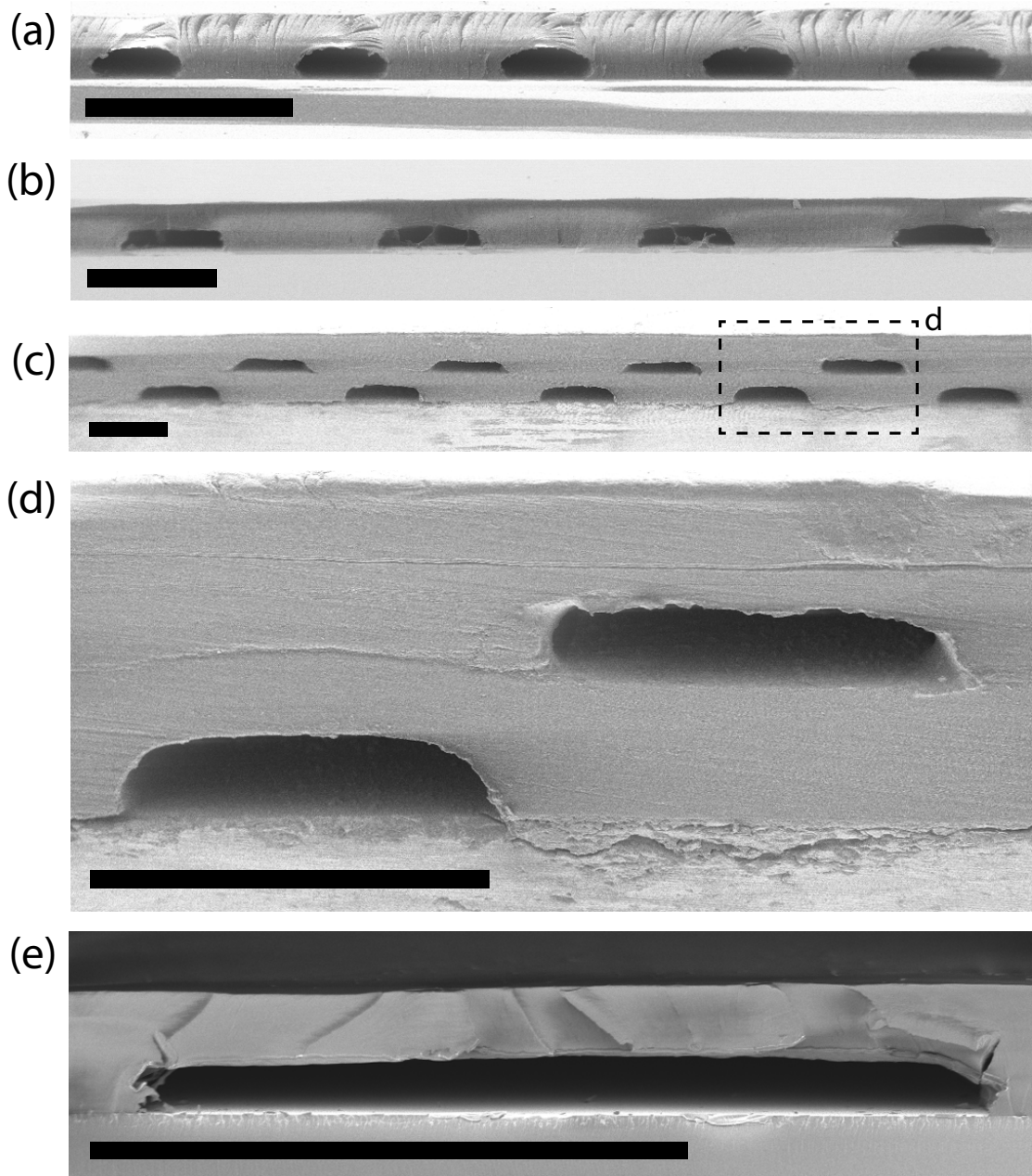


Figure 5.5: SEM cross-section views of fabricated arrays of microcavities in a PI layer: (a)  $30\ \mu\text{m}$  wide voids; (b)  $80\ \mu\text{m}$  wide voids; (c) PI layer stack encompassing two levels of cavities; (d) a zoom into the rectangular area of the image above; (e) a  $150\ \mu\text{m}$  wide channel with an aspect ratio of 15:1. All scale bars correspond to  $100\ \mu\text{m}$ .

**(i) Masking and patterning of PPC.** I found that sputter deposition of the Ti mask, followed by classical photolithography, is less convenient for the fabrication of high-resolution PPC structures than the use of the stencil mask.

Although the sputtering machine was the same for Ti and Al processes (Spider 600, Pfeiffer), reticulation was only observed in Ti films. When Ti was sputtered on PPC, this surface appeared cracked, rough and wrinkled (figure 5.6a), very often already after the metal deposition step. The depth of these cracks reached  $1.5\ \mu\text{m}$  (figure 5.6b) as measured with a profilometer (Wyko NT1100, Veeco). The main reason for the wrinkling effect was the sputtering environment, in which the surface of the PPC was easily heated above the  $T_g \approx 40\ ^\circ\text{C}$ , resulting in polymer reflow phenomena. On the contrary, the unintentional heating of the wafer during Al deposition was probably weaker, and also the Al deposition was performed after the heating step at  $100\ ^\circ\text{C}$  for PPC reflow, during which eventual thermally inducible stresses in the polymer may have decreased in importance.

The low  $T_g$  value of the PPC also posed a problem to the micropatterning of PPC using classical lithography, for which temperatures above  $100\ ^\circ\text{C}$  were needed in the PR baking, exposure and development steps, and which further raised the reticulation effect. A reticulated surface caused problems during PR exposure and development. Since the reflective properties of a wrinkled substrate were non-uniform, finding the right exposure dose was difficult. As a result, the structures were usually overexposed, degrading the resolution of the Ti mask. A reticulated surface of the Ti mask also caused problems during the development of PR, because the developer solution did not penetrate to the indentations in the surface, therefore leaving PR residues. In such a case, in order to obtain the desired level of development, the structures must have been overdeveloped, thus further degraded in resolution.

Figure 5.3f is an example of a PPC etched microstructure with a sputter-deposited Ti mask. The surface of the PPC material was cracked and wrinkled, while the edges of the structured pattern were irregular and contributed to the lack of resolution.

**(ii) PPC dissolution during spin-coating.** Since PPC exhibits a very high solubility in the NMP solvent of the spin-coated PI, a serious solvent-incompatibility problem arose. Figure 5.6c shows partially dissolved PPC structures after PI spin-coating. In order to overcome this challenge, in my process, a low-NMP-content PI was spun shortly using a dynamic dispense procedure.

**(iii) Microcavities collapse during hardbake.** Decomposition of PPC at high temperatures ( $200\text{-}300\ ^\circ\text{C}$ ), when the PI overcoat was softened and not yet fully polymerized, contributed to a common process-related problem – a collapse of the fabricated voids (see figures 5.6d, e). Joseph *et al.* [221] reported this problem as overcoat sagging

### 5.3. Microfabrication process of foam-like PI films

and explained it as follows. At the decomposition temperature, the overcoat material softened and sagged into the cavity, or permanently deformed from pressure built up inside the cavity. A void maintained the exact shape of the sacrificial material only if the overcoating layer kept its rigidity at the high process temperatures [217, 218]. Likewise, in my process, thermal stresses in the PI film promoted the collapse. Finally, since PPC decomposed into a liquid propylene carbonate, the capillary forces favoured sticking of the overcoat on the silicon substrate. Attraction forces appearing between the NMP and the liquefied sacrificial material also promoted the collapse of the voids. Figure 5.4e shows that the long bake at 200 °C did not suffice to completely

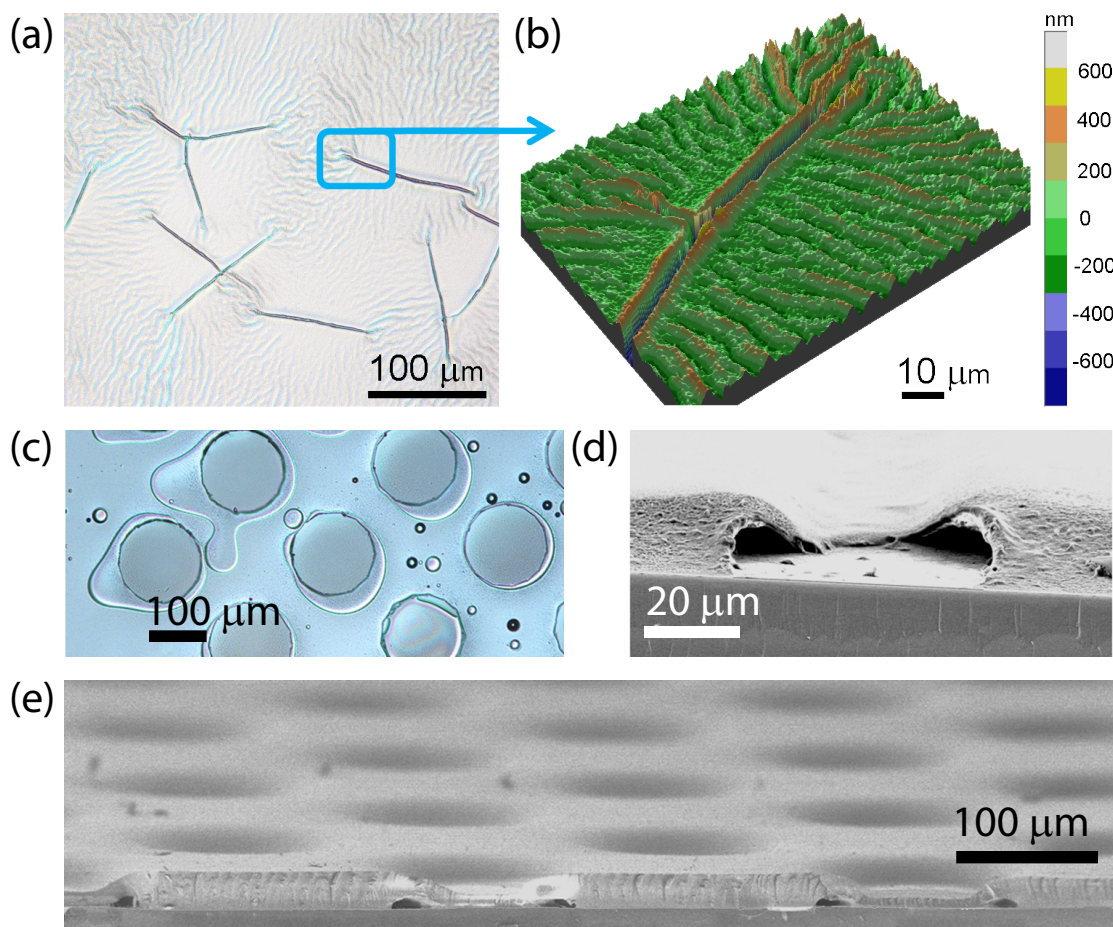


Figure 5.6: Main fabrication challenges: (a, b) wrinkled Ti sputtered mask on the PPC layer: (a) optical microscope photograph of the cracking and wrinkling effect; (b) optical profilometer image reconstruction for a magnified small area of the wrinkled Ti mask surface. (c) Problem of dissolution of PPC structures in the NMP solvent of PI's precursor, visible as bubbles and comets around the circular PPC shapes. (d, e) Collapse issue of the overcoat PI layer during PPC's decomposition: (d) a collapsed channel; (e) a matrix of collapsed voids.

evaporate the NMP solvent from the PI film, despite baking at the temperature close to the solvent's boiling point ( $T_b = 204\text{ }^\circ\text{C}$ ). In fact, the material required curing at  $300\text{ }^\circ\text{C}$  for an additional hour in order to vaporize the excessive 20% of the solvent.

The incorporation of an Al barrier layer was essential to overcome the spin-coating and void collapse problems.

Table 5.1 summarizes the fabrication results obtained for various MW of PPC, with and without the use of the Al barrier layer. PPC-PI combinations that were "not compatible" (solvent interference, destruction of sacrificial material, collapse or deformation of PI overcoat) are identified by "Y", while those that did not exhibit compatibility problems are labeled with "N" (no solvent or mechanical property issue). Since the MW quantifies the size of the polymer chain, shorter chains – thus PPCs with a lower MW – exhibited higher solubility in solvents. However, regardless the MW of PPC, fabrication of microcavities was limited both due to the solvent interference and the collapse of overcoat problems. The Al barrier layer was key for a high yield and reproducibility of the process.

### 5.4 Modelling of microcavity deformation under stress

For the two-dimensional (2D) mechanical modelling, I used a commercial FEM solver (COMSOL Multiphysics 3.5a), assuming the microstructure shown in figure 5.7a, with  $w$  being the width, and  $h$  the height, of the void,  $t$  the thickness of the overcoat layer and  $P$  the pressure uniformly applied on the top surface. The PI isotropic elastic material has a Young's modulus of  $E = 5.9\text{ GPa}$ , Poisson's ratio  $\nu = 0.33$  [178] and I applied a distributed load of  $P = 60\text{ MPa}$ . The bottom side of the microstructure had a fixed boundary condition, whereas the sides and top were free to move and deform following the applied compressive load.

The simulation results are shown in figures 5.7b-e. The colour gradient in the figure displays the calculated von Mises stress in the material, and the deformation of the structure reflects the displacement of the material under the applied load. The maximum vertical displacement of the cavity membrane occurred in the middle, and its corresponding value is marked on the graphs. Several void geometries were simulated: (c) rectangular, (d) ellipsoidal and (e) rounded voids, but the overall size of the models is equal. Figure 5.7b illustrates the simulation results for bulk PI. Under stress, the bulk material yielded the maximum displacement of  $0.4\text{ }\mu\text{m}$ , whereas the displacement of the overcoat layers in cases (c)-(e) corresponded to  $13.3\text{ }\mu\text{m}$ ,  $5.5\text{ }\mu\text{m}$  and  $10.3\text{ }\mu\text{m}$ , respectively. The shape of the cavity had a major influence on the response of the compressed material. The sharper the edges, the larger the deformation of the membrane, while round-edged cavities account for improved stress distribution over the PI.

## 5.4. Modelling of microcavity deformation under stress

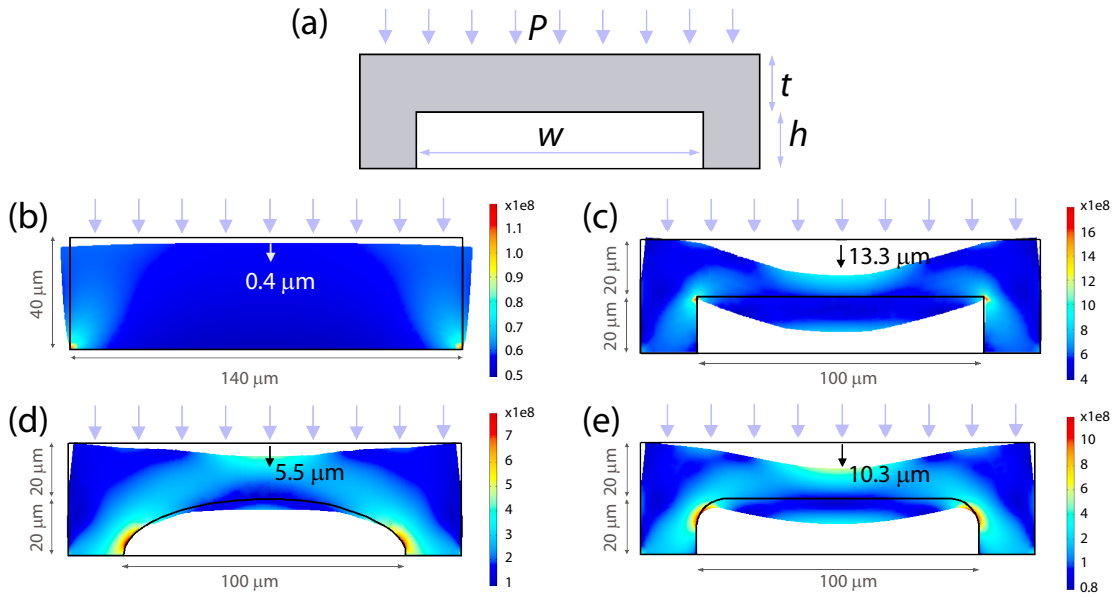


Figure 5.7: 2D modelling of stress and deformation with Comsol Multiphysics, for various void geometries in the PI: (a) schematic of a modelled microstructure, (b) bulk PI layer, (c)  $100\ \mu\text{m} \times 20\ \mu\text{m}$  rectangular cavity, (d) ellipsoidal cavity, (e) rounded cavity. The uniformly applied pressure  $P = 60\ \text{MPa}$ . The surface colours and legend bars correspond to the von Mises stress [Pa], and the deformation of the structure reflects the displacement of the material under the applied load.

I also used the analytical Roark's formula [234] for the deformation of a thin rectangular plate, with as boundary conditions its placement on a supporting post at two sides and clamping at the two other sides, while subjected to a uniform load  $P$ . The maximum deflection of the membrane is given by

$$z_{max} = \frac{-\beta P w^4}{E t^3} \quad (5.1)$$

where  $\beta$  is a coefficient depending on the plate geometry; in my case, I employed  $\beta = 0.021$  [234].

Figure 5.8a is the maximum deflection of a thin square plate, as derived from Roark's formula (5.1) as a function of the plate's width  $w$  with the thickness  $t$  as parameter. The figure indicates that the plate's deflection increases when the thickness  $t$  of the plate is decreased, or the plate width  $w$  becomes larger. In order to obtain large vertical displacements one can either make a thinner plate or a cavity with larger horizontal dimension.

Figure 5.8b is the maximum deflection of a thin square plate as a function of the

plate's thickness  $t$  with a plate width  $w$  as parameter. In figure 5.8b I compared the analytical result of (5.1) with the Comsol Multiphysics simulation of the rectangular cavity shown in figure 5.7c. The trend of the analytical result is close to that of the numerical model, apart from the value for  $\beta=0.06$  that has to be taken instead of the listed value ( $\beta=0.021$ ). This difference is most probably due to the slightly different boundary conditions used in the analytical and numerical models.

### 5.5 Compression experiments of microporous layers

Stress-strain behaviour of polymeric samples can be measured by instrumented presses, tension- and compression-testing machines, or specialized dynamical mechanical analyzers (DMAs) [235]. Yet, such universal testing machines require relatively large specimens. Moreover, they evaluate usually their elastic properties in tension. For instance, strain behaviour of thin PI nanofoam films in tension has been reported for specimens of  $10 \times 30 \text{ mm}^2$  [236], whereas porous polystyrene foams have been tested in compression for the specimens of  $30 \times 30 \times 10 \text{ mm}^3$  [237].

The major challenge in compression testing of micrometer-thin samples is the precise, nanometer-ranged measurement of the strain, which commercial mechanical analyzers and presses cannot provide. The second important issue is the question of critical horizontal alignment of the testing plates with the surface of the compressed material, again difficult to obtain for the above-mentioned types of equipment. Therefore, nanoindentation and microindentation with a custom-prepared flat needle have been

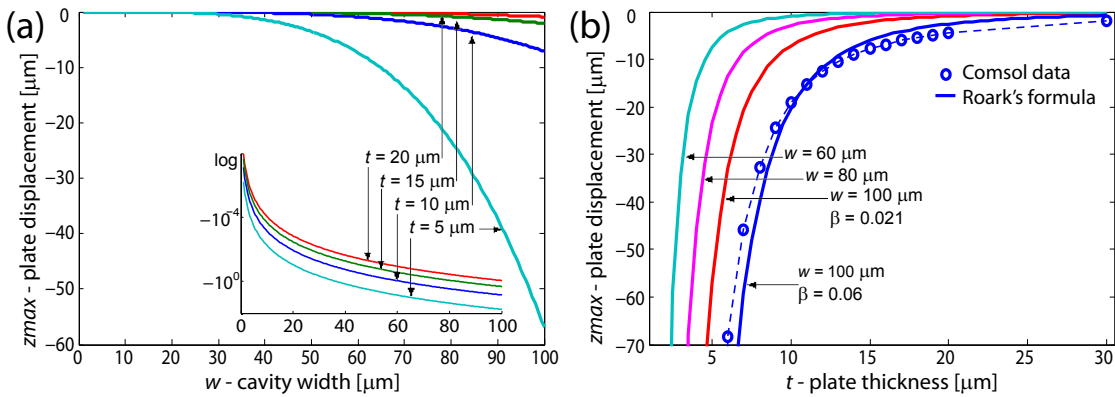


Figure 5.8: Maximum deflection of a thin square plate, as derived from Roark's formula (5.1): (a) dependence on the plate's width  $w$  with the thickness  $t$  as parameter; the inset shows the deflection results on a logarithmic scale; (b) dependence on the plate's thickness  $t$  with a plate width  $w$  as parameter. The circles represent the numerical simulation results (Comsol Multiphysics) obtained for a plate  $w = 100 \mu\text{m}$ , which well compares with Roark's formula for  $w = 100 \mu\text{m}$ , and  $\beta = 0.06$ .

## 5.5. Compression experiments of microporous layers

proposed to provide stress-strain data in compression for thin inorganic films such as copper, vanadium nitride, titanium nitride and tungsten [238].

In this thesis, I proposed two mechanical testing methods for the measurement of the elastic properties of the thin PI microporous layers: a conventional nanoindentation setup (Nano Indenter XP) (see section 5.5.1), and a home-built microcompressor tester (see section 5.5.2).

### 5.5.1 Conventional nanoindentation setup

For the nanoindentation tests, a sharp Berkovich tip was used, and figure 5.9 illustrates the force, hardness and effective Young's modulus as a function of the vertical displacement of the tip, taking eight tip loading and eight tip unloading curves at different positions within the same sample.

Figure 5.9a compares the applied force for bulk PI (T1) and for the microporous PI film with the tip applied above the centre of a void (T2), allowing for a maximum vertical displacement of  $3\ \mu\text{m}$  of the tip. The presence of the void evidently led to a reduced force due to the bending of the thin PI overcoat acting as a thin plate.

The measured hardness, defined as  $H = F/A_r$  where  $A_r$  is the residual nanoindentation area, and  $F$  is the load, is shown in figure 5.9b. Up to a vertical displacement of 1000 nm, the curves T1 and T2 overlap, which indicates that the thin plate over the void was behaving like the bulk material for the applied loads. In the case of the curve T2, for larger vertical displacements of the tip, the thin plate bent, lowering the force, resulting in an apparently reduced hardness. In the case of the curve T1, the observed increase in hardness for displacements above 1800 nm indicates the inhomogeneity of the PI film, *i.e.* the surface part was softer than the bulk.

Young's modulus is given by

$$E = (1 - \nu^2) \left( \frac{2\zeta}{\sqrt{\pi}} \frac{\sqrt{A_p(h)}}{S} - \frac{1 - \nu_i^2}{E_i} \right)^{-1} \quad (5.2)$$

where  $\zeta$  is a geometrical constant,  $A_p(h)$  is the projected area of the indentation at the  $h$  tip depth,  $S$  is the stiffness of the contact derived from continuous stiffness measurement,  $\nu$  is a specimen's Poisson's ratio and  $\nu_i$  and  $E_i$  are the diamond tip's Poisson's ratio and modulus, respectively.

The measured modulus (5.2) is shown in figure 5.9c. The modulus of bulk PI (T1) increased with the depth of the material, whereas the modulus of the thin plate over a

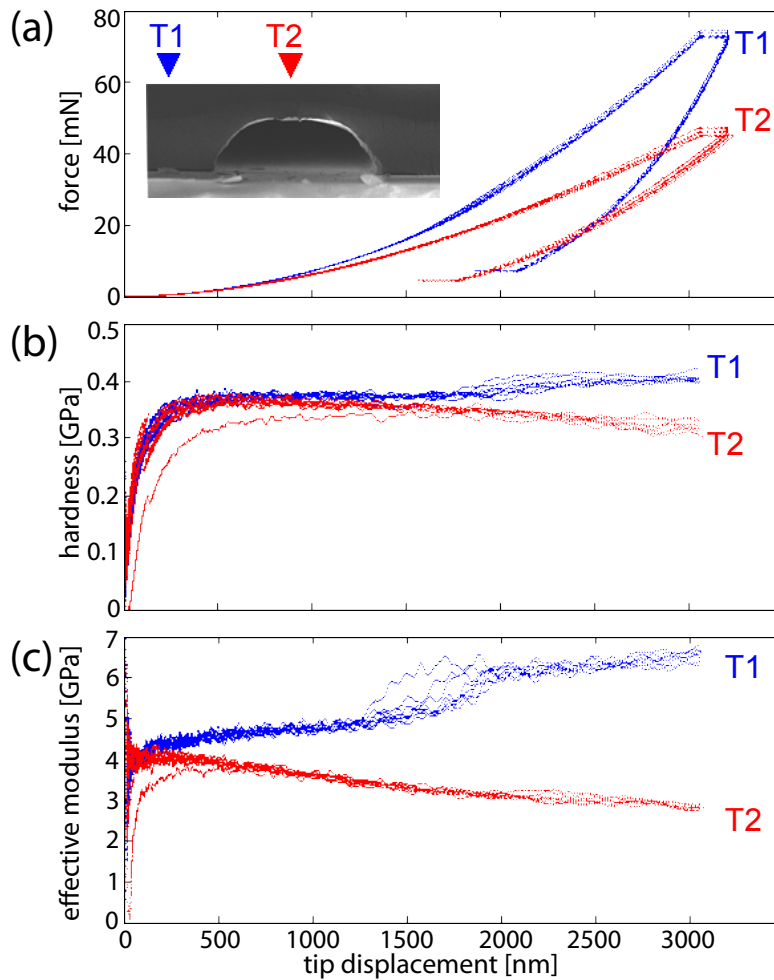


Figure 5.9: Nanoindentation results for a bulk PI film (T1), and a microporous PI film with the tip applied above the centre of a void (T2): (a) the force, (b) the hardness and (c) the effective Young's modulus as a function of the vertical displacement of the tip.

void (T2) was about a factor of two smaller, due to bending of the thin plate, resulting in an apparently reduced effective modulus. The mean value of the effective Young's modulus at the start of the tip unloading equaled  $5.77 \pm 0.06$  GPa for bulk PI, and  $2.51 \pm 0.03$  GPa for a thin plate over a void, confirming the increase of the effective elasticity of the microporous PI. The minor variation of the results gives the evidence of the good homogeneity between the voids within the sample.



## 5.5. Compression experiments of microporous layers

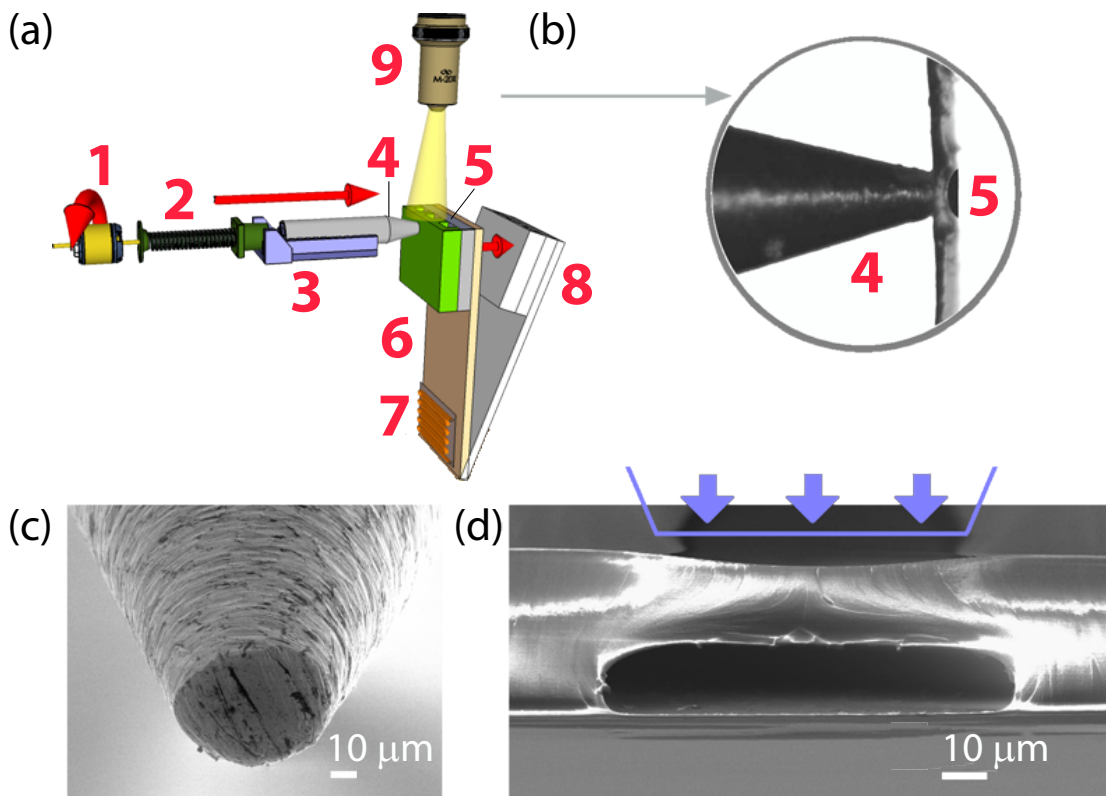


Figure 5.10: (a) Microcompressor setup: (1) rotating motor, (2) micrometric screw, (3) moving stage, (4) compression needle with a flat tip, (5) compressed specimen, (6) supporting beam, (7) force sensor, (8) deflected sample during compression testing, (9) optical microscope. (b) Magnified view of the sample area, as recorded with the microscope. (c) SEM picture of the flat needle used for compression tests. (d) SEM cross-section image of a void used for compression tests, with indication of the position of the flat needle.

### 5.5.2 Home-built microcompressor tester

For the microcompression tests, I used a home-built microtensile and microcompressor tester (EPFL-LMM Mechanical Metallurgy Laboratory), the experimental setup of which is illustrated in figure 5.10a. Compression tests were conducted by placing the test specimen between the flat needle, normal to the sample surface, and the supporting beam. The applied force was registered using a force sensor, while the needle displacement was recorded on a camera connected to an optical microscope (figure 5.10b). The displacement rate of the flat needle was set to  $1.5 \mu\text{m}\cdot\text{min}^{-1}$ , and the load was measured *via* deformation of the calibrated vertical beam with a resolution of 10 nN. The needle had been polished by tripod polisher on a grinding wheel with a diamond grain paper with a grain size of 500 nm (Allied High Tech Products) in order to obtain a flat tip surface (figure 5.10c). The tip was aligned for the measurements

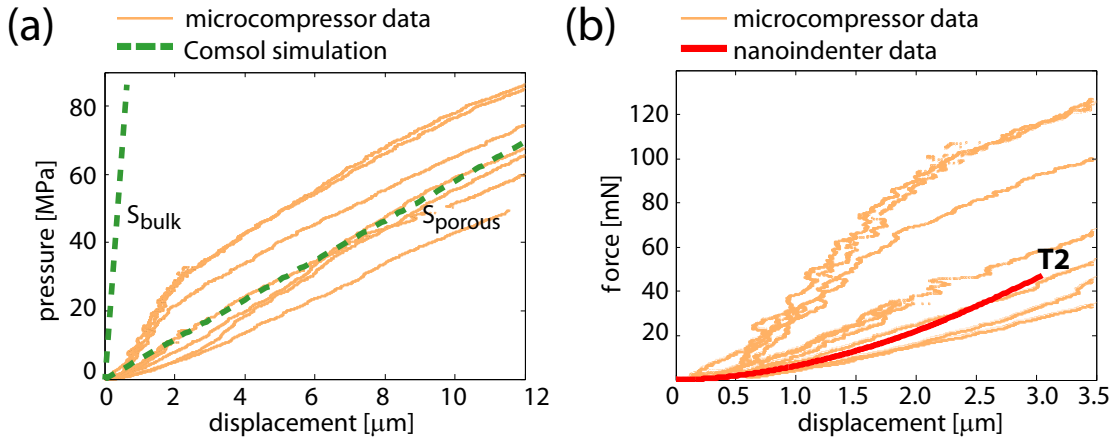


Figure 5.11: (a) Pressure data from ten different PI plates versus displacement normal to the film's surface, and the theoretical prediction, as calculated by Comsol Multiphysics. (b) Force data from ten different PI plates versus their displacement, in comparison with the nanoindentation data (T2).

above the void using the optical microscope (figures 5.10b, d).

The microcompressor measurement results are shown in figure 5.11. A set of ten compression tests has been performed placing the flat needle tip above the void. The pressure exerted on the sample was calculated from the force sensor, assuming a uniform compression under a perfectly flat needle tip of  $64 \mu\text{m}$  in diameter. A moving average filter has been used to reduce the noise from the raw measurement data. The setup had been calibrated using the bulk thin film PI sample and the pure sample holder only, proceeding 14 control tests and assuming a constant setup stiffness of  $-32.8 \text{ mN}/\mu\text{m}$ , when operated in the range of 0–300 mN.

The measurement results shown in figure 5.11a illustrate the displacement of the thin plate under compressive pressure normal to the film's surface for ten different samples. Variations are probably due to differences in needle-void alignment, contact surface and geometrical variability of the void.

The experimental curves are compared with the theoretical prediction modelled by Comsol Multiphysics, as shown in figure 5.11a. The void's compression measurement curves have nearly the same slope as the simulated curve. The stiffness of the thin PI plate above the void, defined as  $S = P/z$  where  $z$  is the vertical displacement of the plate produced by pressure  $P$ , was inferred from the slopes of the curves in figure 5.11a. The measured and the simulated<sup>c</sup> stiffness values are close ( $S_{\text{porous.meas}} = 4.62 \pm 1.87 \text{ MPa}/\mu\text{m}$ ,  $S_{\text{porous.sim}} = 5.82 \text{ MPa}/\mu\text{m}$ ). When compared with the simulated value for a bulk material ( $S_{\text{bulk}} = 150 \text{ MPa}/\mu\text{m}$ ), the stiffness of the porous film has

<sup>c</sup>simulated for a model as shown in figure 5.7e

been reduced by a factor of 30, which confirms the increase of vertical displacement of the material under applied pressure for the porous case. Figure 5.11b represents the same data as shown in figure 5.11a, plotted as force–displacement curves, to allow comparison with data obtained from the nanoindenter (T2). Variation in the experimental data is, like in figure 5.11a, due to needle-void alignment, contact surface and geometrical variability of the void.

## 5.6 Summary and discussion

A process for fabricating PI films with custom-designed microporosity has been developed, based on the heat-induced depolymerization of PI-embedded PPC microstructures. The fabricated foam-like microstructures were up to 40  $\mu\text{m}$  thick and incorporated air cavities with a width ranging from 20 to 200  $\mu\text{m}$ , a length up to 5 mm, and a height of 20  $\mu\text{m}$ . The mechanical stress–strain properties of the microcavities were modeled using both analytical and numerical methods. The simulation data were in good agreement with the results of nanoindentation and microcompression experiments, which showed the reduction of the effective Young's modulus from  $5.77 \pm 0.06$  GPa for bulk PI to  $2.51 \pm 0.03$  GPa for a foam-like layer, and the reduction of stiffness from 150 MPa/ $\mu\text{m}$  for bulk PI to  $4.62 \pm 1.87$  MPa/ $\mu\text{m}$  for a foam-like layer.

The microfabrication method yielded high reproducibility *via* the introduction of an intermediate Al barrier layer. The Al barrier layer was easily deposited at RT, and did not deteriorate the elasticity of the thin PI plate above the void. It prevented PPC from dissolution by the NMP solvent, and stopped microcavities from collapsing. Additionally, the problem of collapse was avoided by applying an appropriate heating process, in which the PI overcoat was partially polymerized before decomposition of the sacrificial PPC material. Moreover, by using stencil lithography, an improved resolution of the void structures was obtained.



## 6 Conclusions and outlook

This thesis presented new designs of micromachined flexible capacitive sensors for uni-axial and three-axial force measurements. Furthermore, an innovative flexible porous polymeric film structure was introduced, which has the potential for integration into these sensors as a cellular dielectric.

Depending upon their design, capacitive sensors can measure uni-axial or three-axial forces. Elastic polymeric materials and packagings are robust and ideal supports for large-area sensor arrays adapting to an arbitrary shape. Micromachined capacitive sensors in such polymeric packages are sensitive to the applied force, protected against overloads, conformable and expandable to large areas. Moreover, polymer-based capacitive sensors can be adjusted to offer application-specific sensitivity and range of operation. Taken together, these properties result in a sensitive and robust skin-like device, exhibiting vast potential for application in artificial skins of robotic bodies or prosthetic limbs.

### 6.1 Flexible capacitive sensor for uni-axial large force measurements

In chapter 3, a uni-axial flexible force sensor was developed, the operation of which was based on the measurement of a load-induced capacitance change. The use of polyimide (PI), both as a substrate and elastic dielectric between the electrodes, assured flexibility of the structure. The polymer technologies allowed also realization of two-level PI microstructures with gentle slopes, which facilitated producing overlapping, displaceable electrodes with contact pads on the same level. The golden-stud technique provided a robust bonding to the sensor. An analytical formula and finite element analyses modelled the sensor's capacitance. The electrical characterization of the capacitors revealed capacitances in the range of 130 pF and a typical force

sensitivity of 0.5-1 fF/N, in excellent agreement with the model. The sensor showed high strength and durability, when operated in the 1 kN force range. It exhibited linearity and absence of hysteresis, and a lower detection limit of 100 N. The sensor could continually withstand higher loads, in excess of 3 kN, without damage.

Application-specific sensitivity and range are envisaged for touch-sensing systems. By changing physical parameters of my sensor (*i.e.* the thickness of the dielectric, the polymer's elasticity, the plate size) the sensor's characteristics can be tailored to the application. Since industrial robots operate in the kN range of contact forces when gripping and manipulating objects, the developed flexible and durable force sensor can find possible implementation in grippers of industrial robots. Moreover, currently, a large number of industrial robots have no sensory abilities, therefore providing them with touch sensing would allow expanding their performance and operating capabilities. The robust PI packaging would permit withstanding heavy workload and harsh industrial conditions (temperature, humidity, chemical stresses, or sudden force).

Elasticity, flexibility, and conformability are the required features of an ideal distributed tactile sensor. The developed sensor was flexible and functioned well on surfaces having curvatures consistent with robotic grippers. Therefore, it could measure manipulator's contact forces, conforming to arbitrary shapes of industrial robots' gripper jaws. When placed or distributed inside the robotic gripper, the thin sensors would not significantly increase the thickness of a robotic part, and could be simply attached to the body using adhesives. For such robotic applications, in case grippers are metallic, or if metallic pieces need to be gripped, the susceptibility of the sensor to conductive surfaces resulting in parasitic stray capacitance could be handled by surrounding the sensor with appropriate guard or shield electrodes [150].

## 6.2 Flexible capacitive sensor for three-axial force measurements

Chapter 4 reported on the development of a three-axial force sensor composed of flexible polymeric films. The finger-shaped electrode design rendered a capacitive sensor for the measurement of 3D load with high sensitivity in all axes. Integration of three polymers in the sensor's technology process, namely PI, Parylene-C, and polydimethylsiloxane (PDMS), provided an overall flexibility of the sensor and elasticity of the capacitor's dielectric. Theoretical models permitted the estimation of the sensor's capacitance and its 3-axial force sensitivity. The electrical characterization of the capacitors showed static capacitances in the range of 20 pF, in excellent agreement

### 6.3. Flexible films with custom-designed microporosity

---

with the model. The electromechanical characterization of the capacitors revealed in the normal direction a sensitivity  $S_z = 0.024 \text{ kPa}^{-1}$  for pressures  $<10 \text{ kPa}$ , whereas for higher pressures  $>10 \text{ kPa}$  the measured sensitivity  $S_z = 6.6 \cdot 10^{-4} \text{ kPa}^{-1}$ . Typical measured shear force sensitivity  $S_x = 2.8 \cdot 10^{-4} \text{ kPa}^{-1}$ .

A critical ability required from a single tactile pixel is the measurement of not only the magnitude, but also the direction of load. The combination of the capacitive finger-like electrode design with polymer technologies allowed obtaining a sensor that was capable of measuring three-axial forces with high sensitivity. Human skin experiences continuously 3-axial force changes, whose aspects should be considered when designing artificial skins for prosthetic applications. The developed 3-axial capacitive force sensor is of major interest for touch sensors in prosthetic and symbiotic robot's artificial skins, where the measurement of 3D force is crucial, mainly for hand-skin applications for proper object manipulation, and foot-skin applications for gait stabilization or analysis.

A specific sensitivity and range are envisaged for prosthetic tactile sensors. The observed range of measurable forces and 3-axial sensitivities of my sensor placed it exactly in the region of interest for human hand- and foot-artificial skin applications. Thanks to the specific design of the top electrode, the sensor's sensitivity was comparable with the tactile sensation of human skin, which relies on four types of mechanoreceptors. The sensor exhibited an increased sensitivity at low pressures, which is primarily desirable in real-world applications, especially for tactile sensing by fingertips. That is, the high sensitivity of the sensor at soft touch reflected the ability of fine tactile sensation of human skin provided with superficially-located Merkel and Meissner's mechanoreceptors. For higher loads, the sensor reflected the ability of high-pressure perception on human skin by deep-buried Pacinian and Ruffini mechanoreceptors, and provided a wide range of detectable forces with a lower sensitivity.

The polymer technologies allowed for fabrication of a flexible and conformable tactile sensor, which, in future application of determining forces on human body parts, would efficiently cover the involved body area surface and be conformal to its shape.

### 6.3 Flexible films with custom-designed microporosity

A new method for fabrication of microporous PI layers with high reproducibility and yield has been covered in chapter 5. The realization of PI films with custom-designed microporosity was possible by using polypropylene carbonate (PPC) as a sacrificial material. The process, based on the heat-induced depolymerization of PI-embedded PPC microstructures, allowed obtaining foam-like microstructures with the thickness of up to  $40 \mu\text{m}$ , which incorporated air cavities with a width ranging from  $20$  to  $200 \mu\text{m}$ ,

a length up to 5 mm, and a height of 20  $\mu\text{m}$ . Analytical and numerical methods permitted modelling the mechanical stress–strain properties of the microcavities. The simulation data were in good agreement with the results of nanoindentation and microcompression experiments. The tests proved that a reduction of the effective Young's modulus  $E$  and stiffness  $S$  was obtained for a foam-like layer when compared to bulk PI ( $E_{\text{porous}} = 2.51$  GPa,  $E_{\text{bulk}} = 5.77$  GPa,  $S_{\text{porous}} = 4.62$  MPa/ $\mu\text{m}$ ,  $S_{\text{bulk}} = 150$  MPa/ $\mu\text{m}$ ).

The human cutaneous sensors cover the whole body. Further, the tactile sensitivity of human skin is body site-dependent. In analogy, an artificial touch system should be a distributed large-area sensory organ, with a spatial resolution and sensitivity modulated according to the body site where it is to be placed. The method presented in this thesis could allow development of such large-area artificial skins with variable touch-sensitive regions, by introducing a new type of flexible material.

By custom-designing the local porosity, my flexible layers can therefore find possible implementation in capacitive force sensing applications of large-area tactile surfaces and artificial skins, where they could be tailored to cutaneous sensitivity characteristics of various body sites. In capacitive force sensors, one requires an elastic dielectric between the electrodes, hence a cellular polymeric material could perform excellently given its superior dielectric and mechanical properties. Provided the overall sensor size is much larger than the typical cavity size, one can tailor the mechanical properties of a dielectric by varying the number, shape and spacing of the voids, hence obtaining in-between the capacitive plates a foam-like dielectric with varying elasticity. By increasing thoroughly the size of the void, one can also obtain thin flexible suspended membranes, acting as a support for capacitive electrodes spaced by an air-cavity dielectric. To conclude, the elasticity of the dielectric between the capacitive electrodes could be tuned by forming microporous layers or suspended insulation membranes. The microporosity can be easily and precisely varied, by modifying the number, volume, shape and distribution of the voids. Since the manufactured microporous PI has the structure of a closed cell, it should also have improved moisture resistance and shock-absorption compared with open-cell foams.

### 6.4 Towards artificial skin

The microfabrication processes of the PI microporous layers and those of the flexible capacitive force sensors are compatible with respect to each other, bringing promise in the integration of the different technologies and expansion into large-area tactile surfaces of custom-designed sensitivity. In particular, by combining the PI-based flexible capacitive force sensors, and microporous PI as its dielectric, with the PI-Parylene-



Table 6.1: Characteristics of the artificial sensors and porous films developed in this thesis, in comparison with the features of a human skin.

Feature	human skin	uni-axial force sensor (chapter 3)	3-axial force sensor (chapter 4)	porous films (chapter 5)
covering large area	✓	✓	✓	✓
site-specific spatial resolution	✓	✓	✓	✓
site-specific sensitivity	✓	✗	✗	✓
activity-specific sensitivity	✓	✓	✓	n/a
activity-specific range	✓	✓	✓	n/a
detection of 1D forces	✓	✓	✓	n/a
detection of 3D forces	✓	✗	✓	n/a
flexible	✓	✓	✓	✓
conformable	✓	✓	✓	✓

C-PDMS-based flexible 3-axial force sensors, one can obtain an expanded sensory organ, with location-dependent cutaneous sensitivity characteristics. By processing all in a single batch, one can define the areas of specified touch sensitivity, variable spatial resolution, particular range of detectable forces, and sensitivity to three-axial or uni-axial force only. Table 6.1 summarizes, and compares with the features of a human skin, the characteristics of the artificial sensors and the microporous films developed in this thesis, which, combined, can be used for artificial mimicking of human tactile sensing.

To conclude the outlook, the integration of miniaturised 1D and 3D force sensors in large-area flexible substrates with custom-designed elasticity could provide the basis for artificial skin and mimicking of human tactile sensing. Such a large-area organ, with distributed tactile cells, detecting both 1D and 3D contact forces, with body site-dependent tactile sensibility, site-specific spatial resolution and dynamic range, would remain elastic, flexible and conformal to arbitrarily-shaped body surfaces. Finally, the tactile sensation provided with this sensory organ would resemble that of human skin, which is based on the four types of mechanoreceptors, distributed all over the body, with variable density and embedded at different depths, always working together to provide both sensitivity to fine touch and to high pressure.



# A Appendix A

When several lines are placed next to each other, the total capacitance of one line includes the coupling capacitance between the lines and ground capacitance between the line and the ground. In case of three parallel strip lines, of width  $w$ , thickness  $t$ , length  $L$ , spaced by  $s$ , and separated by  $h$  from the infinite ground substrate (figure A.1), the total capacitance is known as Sakurai's formula [186], given by:

$$C = \varepsilon_0 \varepsilon \left\{ 1.15 \left( \frac{w}{h} \right) + 2.8 \left( \frac{t}{h} \right)^{0.222} + \dots \right. \\ \left. + 2 \left[ 0.03 \left( \frac{w}{h} \right) + 0.83 \left( \frac{t}{h} \right) + 0.07 \left( \frac{t}{h} \right)^{0.222} \right] \cdot \left( \frac{h}{s} \right)^{1.34} \right\} \cdot L \quad (\text{A.1})$$

where  $C_1 = \varepsilon_0 \varepsilon L \left\{ 1.15 \left( \frac{w}{h} \right) + 2.8 \left( \frac{t}{h} \right)^{0.222} \right\}$  is the capacitance of a single line placed on a bulk, and  $C_2 = C_3 = \varepsilon_0 \varepsilon L \left[ 0.03 \left( \frac{w}{h} \right) + 0.83 \left( \frac{t}{h} \right) + 0.07 \left( \frac{t}{h} \right)^{0.222} \right] \cdot \left( \frac{h}{s} \right)^{1.34}$  are the capacitances of the couplings between the lines.

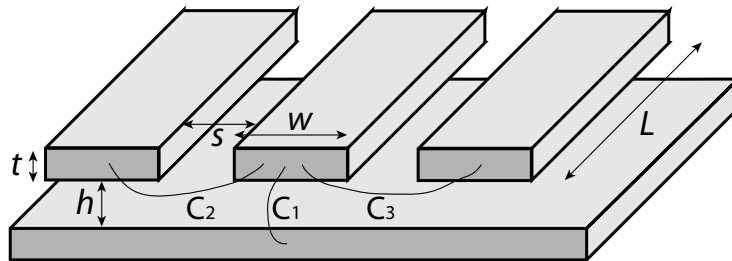


Figure A.1: Capacitance of three strip lines and a plane.



## B Appendix B

In chapter 3.3.1 the force sensitivity of the sensor is calculated by a Taylor series (TS) expansion (B.1) of equation 3.1 and given with the formula B.2.

$$TS[f(x)] = \sum_{n=0}^{\infty} \frac{f^{(n)}(a)}{n!} (x-a)^n \quad (\text{B.1})$$

$$\begin{aligned} \frac{\Delta C}{\Delta F} = & \frac{b_1}{\Delta F} \sum_{k=0}^{\infty} \frac{(-1)^{k+1} (\Delta h)^k}{h_0^{k+1}} + \dots \\ & + \frac{0.222b_2}{\Delta F} \sum_{k=0}^{\infty} \frac{(-1)^{k+1} (\Delta h)^k \cdot \Gamma(1.222 + k)}{(k+1)! \cdot h_0^{k+0.222} \cdot \Gamma(1.222)} + \dots \\ & + \frac{0.34b_3}{\Delta F} \sum_{k=0}^{\infty} \frac{(-1)^k (\Delta h)^k \cdot \Gamma(0.66 + k)}{(k+1)! \cdot h_0^{k-0.34} \cdot \Gamma(0.66)} + \dots \\ & + \frac{1.118b_4}{\Delta F} \sum_{k=0}^{\infty} \frac{(-1)^k (\Delta h)^k \cdot \Gamma(-0.118 + k)}{(k+1)! \cdot h_0^{k-1.118} \cdot \Gamma(-0.118)} \end{aligned} \quad (\text{B.2})$$

where the gamma function  $\Gamma$  is expressed as:

$$\Gamma(n) = (n-1)! \quad (\text{B.3})$$



## Bibliography

- [1] Isaac Asimov. *Robbie (Strange Playfellow)*. Super Science Stories. Popular Publications, New York, 1940.
- [2] T. Morita, H. Iwata, and S. Sugano. Development of human symbiotic robot: Wendy. In *International Conference on Robotics and Automation (ICRA)*, volume 1-4, pages 3183–8, New York, 1999. IEEE.
- [3] Leigh R. Hochberg, Daniel Bacher, Beata Jarosiewicz, Nicolas Y. Masse, John D. Simeral, Joern Vogel, Sami Haddadin, Jie Liu, Sydney S. Cash, Patrick van der Smagt, and John P. Donoghue. Reach and grasp by people with tetraplegia using a neurally controlled robotic arm. *Nature*, 485(7398):372–375, 2012.
- [4] K. Wada and T. Shibata. Living with seal robots - its sociopsychological and physiological influences on the elderly at a care house. *IEEE Transactions on Robotics*, 23(5):972–80, 2007.
- [5] Bio-mimetic control research center RIKEN. Soft human interactive robot ri-man. [http://rtc.nagoya.riken.jp/RI-MAN/index\\_us.html](http://rtc.nagoya.riken.jp/RI-MAN/index_us.html), 2012.
- [6] Jaeho Lee and Byulsaim Kwak. A task management architecture for control of intelligent robots. In Zhong-Zhi Shi and Ramakoti Sadananda, editors, *Lecture Notes in Computer Science. Agent Computing and Multi-Agent Systems*, volume 4088 of *Lecture Notes in Computer Science*, pages 59–70. Springer Berlin, Heidelberg, 2006.
- [7] ABB. Dual-arm concept robot. <http://www.abb.com/cawp/abbzh254/8657f5e05ede6ac5c1257861002c8ed2.aspx>, 2012.
- [8] Institute of Robotics DLR and Mechatronics. Light-weight robot (lwr). <http://www.dlr.de/rm/en/>, 2012.
- [9] BBC. Olympic torch: Hyde park crowd cheer flame’s arrival. <http://www.bbc.co.uk/news/uk-18982374>, 2012.

## Bibliography

---

- [10] TouchBionics. The i-limb ultra prosthetic hand. <http://www.touchbionics.com/>, 2012.
- [11] Isaac Asimov. *Les robots*. J'ai lu: 453. J'ai lu, Paris, 1986.
- [12] TWENDY team WASEDA University, Sugano Laboratory. human symbiotic robot twendy-one. <http://www.twendyone.com>, 2012.
- [13] F. M. Wilcox. *Forbidden planet*, 1956.
- [14] R. Andrew Russell. *Robot tactile sensing*. Prentice Hall, New York, 1990.
- [15] A. Albu-Schaffer, O. Eiberger, M. Grebenstein, S. Haddadin, C. Ott, T. Wimbock, S. Wolf, and G. Hirzinger. Soft robotics. *Robotics and Automation Magazine, IEEE*, 15(3):20–30, 2008.
- [16] Deepak Trivedi, Christopher D. Rahn, William M. Kier, and Ian D. Walker. Soft robotics: Biological inspiration, state of the art, and future research. *Applied Bionics and Biomechanics*, 5(3):99–117, 2008.
- [17] Marc J. Madou. *Fundamentals of microfabrication the science of miniaturization*. CRC Press, Boca Raton, FL, 2nd edition, 2002.
- [18] S. P. Lacour, J. Jones, S. Wagner, T. Li, and Z. G. Suo. Stretchable interconnects for elastic electronic surfaces. *Proceedings of the IEEE*, 93(8):1459–1467, 2005.
- [19] Jeremy M. Wolfe, Keith R. Kluender, Dennis M. Levi, Linda M. Bartoshuk, Rachel S. Herz, Roberta L. Klatzky, and Susan J. Lederman. *Sensation & perception*. Sinauer Associates, Inc., Sunderland, 2006.
- [20] Sylvia S. Mader. *Human biology*. Wm. C. Brown Publishers, College Division, Dubuque, 1988.
- [21] Sylvia S. Mader. *Inquiry into life, twelfth edition*. McGraw-Hill, Boston, 12th edition, 2008.
- [22] Ravinder S. Dahiya, G. Metta, M. Valle, and G. Sandini. Tactile sensing - from humans to humanoids. *IEEE Transactions on Robotics*, 26(1):1–20, 2010.
- [23] Eye of Science and Science Photo Library. Skin layers, sem, p710/0438. <http://www.sciencephoto.com/media/315871/view>.
- [24] Kenneth Johnson. Neural basis of haptic perception. In *Stevens' Handbook of Experimental Psychology*. John Wiley & Sons, Inc., 2002.



- [25] Qiang Tao Guo, Yuan Li Jun, and Feng Jiang Xian. Research on virtual testing of hand pressure distribution for handle grasp. In *2011 International Conference on Mechatronic Science, Electric Engineering and Computer (MEC)*, pages 1610–1613. IEEE, 2011.
- [26] E. Turner, Deborah and James Woodburn. Characterising the clinical and biomechanical features of severely deformed feet in rheumatoid arthritis. *Gait & Posture*, 28(4):574–580, 2008.
- [27] Wesley P. Chan, Chris A.C. Parker, H.F. Machiel Van der Loos, and Elizabeth A. Croft. Grip forces and load forces in handovers: implications for designing human-robot handover controllers. In *Proceedings of ACM/IEEE conference on Human-Robot Interaction*, pages 2157692, 9–16, Boston, Massachusetts, USA, 2012. ACM.
- [28] R. S. Johansson and G. Westling. Roles of glabrous skin receptors and sensorimotor memory in automatic control of precision grip when lifting rougher or more slippery objects. *Experimental Brain Research*, 56(3):550–564, 1984.
- [29] T. Sugaiwa, H. Iwata, and S. Sugano. Shock absorbing skin design for human-symbiotic robot at the worst case collision. In *IEEE-RAS International Conference on Humanoid Robots*, pages 496–501, 2008.
- [30] S. Phan, Quek Zhan Fan, P. Shah, Shin Dongjun, Z. Ahmed, O. Khatib, and M. Cutkosky. Capacitive skin sensors for robot impact monitoring. In *Conference on Intelligent Robots and Systems (IROS)*, pages 2992–7. IEEE, 2011.
- [31] J. Monzee, Y. Lamarre, and A. M. Smith. The effects of digital anesthesia on force control using a precision grip. *Journal of Neurophysiology*, 89(2):672–683, 2003.
- [32] R S Johansson and A B Vallbo. Tactile sensibility in the human hand: relative and absolute densities of four types of mechanoreceptive units in glabrous skin. *The Journal of Physiology*, 286(1):283–300, 1979.
- [33] E. S. Dellon, R. Mourey, and A. L. Dellon. Human pressure perception values for constant and moving one-point and 2-point discrimination. *Plastic and Reconstructive Surgery*, 90(1):112–117, 1992.
- [34] William P. Hanten, Wen-Yin Chen, Alicia Ann Austin, Rebecca E. Brooks, Harlan Clay Carter, Carol Ann Law, Melanie Kay Morgan, Donna Jean Sanders, Christe Ann Swan, and Amy Lorraine Vanderslice. Maximum grip strength in normal subjects from 20 to 64 years of age. *Journal of Hand Therapy*, 12(3):193–200, 1999.

## Bibliography

---

- [35] H. B. Menz, M. E. Morris, and S. R. Lord. Foot and ankle characteristics associated with impaired balance and functional ability in older people. *Journals of Gerontology Series a-Biological Sciences and Medical Sciences*, 60(12):1546–1552, 2005.
- [36] H Rouhani, J Favre, X Crevoisier, BM Jolles, O Zobeiri, and K Aminian. Outcome evaluation of ankle osteoarthritis treatments using spatio-temporal gait parameters and plantar pressure during unconstrained long distance walking. In *19th Conference International Society for Posture and Gait Research*, pages 110–111, 2009.
- [37] E. M. Hennig and T. Sterzing. Sensitivity mapping of the human foot: thresholds at 30 skin locations. *Foot and Ankle International*, 30(10):986–91, 2009.
- [38] Scott Cameron Wearing, Stephen Urry, James E. Smeathers, and Diana Battistutta. A comparison of gait initiation and termination methods for obtaining plantar foot pressures. *Gait & Posture*, 10(3):255–263, 1999.
- [39] R. Hosein and M. Lord. A study of in-shoe plantar shear in normals. *Clinical Biomechanics*, 15(1):46–53, 2000.
- [40] H. Rouhani, J. Favre, X. Crevoisier, and K. Aminian. Ambulatory assessment of 3d ground reaction force using plantar pressure distribution. *Gait & Posture*, 32(3):311–6, 2010.
- [41] Hanna Yousef, Mehdi Boukallel, and Kaspar Althoefer. Tactile sensing for dexterous in-hand manipulation in robotics—a review. *Sensors and Actuators A: Physical*, 167(2):171–187, 2011.
- [42] J. Dargahi and S. Najarian. Human tactile perception as a standard for artificial tactile sensing - a review. *International Journal of Medical Robotics and Computer Assisted Surgery*, 1(1):23–35, 2004.
- [43] R. S. Fearing and T. O. Binford. Using a cylindrical tactile sensor for determining curvature. In *International Conference on Robotics and Automation*, pages 765–771 vol.2. IEEE, 1988.
- [44] V. Maheshwari and R. E. Saraf. High-resolution thin-film device to sense texture by touch. *Science*, 312(5779):1501–4, 2006.
- [45] Richard Crowder. Toward robots that can sense texture by touch. *Science*, 312(5779):1478–1479, 2006.

- [46] S. Kim, M. Spenko, S. Trujillo, B. Heyneman, D. Santos, and M. R. Cutkosky. Smooth vertical surface climbing with directional adhesion. *IEEE Transactions on Robotics*, 24(1):65–74, 2008.
- [47] K. Hirai, M. Hirose, Y. Haikawa, and T. Takenaka. The development of honda humanoid robot. In *Conference on Robotics and Automation*, volume 2, pages 1321–1326 vol.2. IEEE, 1998.
- [48] Y. Takahashi, K. Nishiwaki, S. Kagami, H. Mizoguchi, and H. Inoue. High-speed pressure sensor grid for humanoid robot foot. In *International Conference on Intelligent Robots and Systems (IROS)*, pages 3909–3914. IEEE, 2005.
- [49] Eun-Soo Hwang, Jung-Hoon Seo, and Yong-Jun Kim. A polymer-based flexible tactile sensor for both normal and shear load detections and its application for robotics. *Journal of microelectromechanical systems*, 16(3):556–63, 2007.
- [50] G. J. Monkman, R. Steinmann, and H. Schunk. *Robot Grippers*. Wiley-VCH, 2006.
- [51] P. E. Crago, H. J. Chizeck, M. R. Neuman, and F. T. Hambrecht. Sensors for use with functional neuromuscular stimulation. *IEEE Transactions on Biomedical Engineering*, 33(2):256–268, 1986.
- [52] Mark R. Cutkosky. *Robotic grasping and fine manipulation*. Kluwer Academic Publishers, Boston, 1985.
- [53] Mark Cutkosky, Robert Howe, and William Provancher. Part c: Sensing and perception, force and tactile sensors. In *Springer handbook of robotics*, Siciliano, Bruno and Khatib, Oussama (eds.), page 1611 S. Springer, Berlin, 2008.
- [54] Shadow Robot Company. The shadow dexterous hand. <http://www.shadowrobot.com/hand/>, 2012.
- [55] Festo. Bionic handling assistant. [www.festo.com](http://www.festo.com), 2012.
- [56] ATI Industrial Automation. Six-axis force/torque sensors. <http://www.ati-ia.com/products/ft/sensors.aspx>, 2012.
- [57] BL Autotec Ltd. Multi-axis force torque sensor. <https://www.bl-autotec.co.jp/english/index.html>, 2012.
- [58] Johan Tegin and Jan Wikander. Tactile sensing in intelligent robotic manipulation - a review. *Industrial Robot: An International Journal*, 32(1):64–70, 2005.

## Bibliography

---

- [59] H. Iwata, S. Sugano, and Ieee. Design of human symbiotic robot twenty-one. In *International Conference on Robotics and Automation (ICRA)*, volume 1-7, pages 3294–3300. IEEE, 2009.
- [60] Institute of Robotics DLR and Mechatronics. Miniature force-torque sensor. [http://www.dlr.de/rm/en/desktopdefault.aspx/tabid-3806/6231\\_read-8995/](http://www.dlr.de/rm/en/desktopdefault.aspx/tabid-3806/6231_read-8995/), 2012.
- [61] T. Wimboeck, C. Ott, and G. Hirzinger. Passivity-based object-level impedance control for a multifingered hand. In *International Conference on Intelligent Robots and Systems (IROS)*, volume 1-12, pages 4621–4627. IEEE, 2006.
- [62] A. Albu-Schäffer, S. Haddadin, Ch. Ott, A. Stemmer, T. Wimböck, and G. Hirzinger. The dlr lightweight robot: design and control concepts for robots in human environments. *Industrial Robot: An International Journal*, 34(5):376–385, 2007.
- [63] Pascale Ehrenfreund. *Laboratory astrophysics and space research*. Kluwer, Dordrecht, 1999.
- [64] Interlink Electronics. Fsr: Force-sensing resistor technology. <http://www.interlinkelectronics.com>, 2012.
- [65] TEKSCAN. Pressure mapping systems and force sensors. <http://www.tekscan.com/>, 2012.
- [66] J. A. Fishel, V. J. Santos, and G. E. Loeb. A robust micro-vibration sensor for biomimetic fingertips. In *2nd International Conference on Biomedical Robotics and Biomechanics (BioRob)*, pages 659–663, IEEE, 2008.
- [67] SynTouch. Syntouch and biotac tactile sensor technologies. <http://www.syntouchllc.com>, 2012.
- [68] Jeremy A. Fishel and Gerald E. Loeb. Bayesian exploration for intelligent identification of textures. *Frontiers in Neurorobotics*, 6, 2012.
- [69] I. Lee and H. I. Sung. Development of an array of pressure sensors with pvdf film. *Experiments in Fluids*, 26(1-2):27–35, 1999.
- [70] P. P. L. Regtien. Tactile imaging. *Sensors and Actuators A: Physical*, 31(1-3):83–89, 1992.
- [71] P. Dario. Tactile sensing: Technology and applications. *Sensors and Actuators A: Physical*, 26(1-3):251–256, 1991.

- [72] John J. Boland. Flexible electronics: Within touch of artificial skin. *Nature Materials*, 9(10):790–792, 2010.
- [73] M. H. Lee and H. R. Nicholls. Tactile sensing for mechatronics - a state of the art survey. *Mechatronics*, 9:1–31, 1999.
- [74] V. J. Lumelsky, M. S. Shur, and S. Wagner. Sensitive skin. *Sensors Journal, IEEE*, 1(1):41–51, 2001.
- [75] T. Someya, T. Sekitani, S. Iba, Y. Kato, H. Kawaguchi, and T. Sakurai. A large-area, flexible pressure sensor matrix with organic field-effect transistors for artificial skin applications. *Proceedings of the National Academy of Sciences of the United States of America*, 101(27):9966–9970, 2004.
- [76] T. Someya, Y. Kato, T. Sekitani, S. Iba, Y. Noguchi, Y. Murase, H. Kawaguchi, and T. Sakurai. Conformable, flexible, large-area networks of pressure and thermal sensors with organic transistor active matrixes. *Proceedings of the National Academy of Sciences of the United States of America*, 102(35):12321–12325, 2005.
- [77] Stefan C. B. Mannsfeld, Benjamin C. K. Tee, Randall M. Stoltenberg, Christopher V. H. H. Chen, Soumendra Barman, Beinn V. O. Muir, Anatoliy N. Sokolov, Colin Reese, and Zhenan Bao. Highly sensitive flexible pressure sensors with microstructured rubber dielectric layers. *Nature Materials*, 9(10):859–64, 2010.
- [78] Kuniharu Takei, Toshitake Takahashi, Johnny C. Ho, Hyunhyub Ko, Andrew G. Gillies, Paul W. Leu, Ronald S. Fearing, and Ali Javey. Nanowire active-matrix circuitry for low-voltage macroscale artificial skin. *Nature Materials*, 9(10):821–6, 2010.
- [79] Hyung-Kew Lee, Jaehoon Chung, Sun-Il Chang, and Euisik Yoon. Real-time measurement of the three-axis contact force distribution using a flexible capacitive polymer tactile sensor. *Journal of Micromechanics and Microengineering*, 21(3):035010, 2011.
- [80] T. R. Jensen, R. G. Radwin, and J. G. Webster. A conductive polymer sensor for measuring external finger forces. *Journal of Biomechanics*, 24(9):851–8, 1991.
- [81] D. J. Beebe, A. S. Hsieh, D. D. Denton, and R. G. Radwin. A silicon force sensor for robotics and medicine. *Sensors and Actuators A: Physical*, A50(1-2):55–65, 1995.
- [82] D. J. Beebe, D. D. Denton, R. G. Radwin, and J. G. Webster. A silicon-based tactile sensor for finger-mounted applications. *IEEE Transactions on Biomedical Engineering*, 45(2):151–9, 1998.

## Bibliography

---

- [83] J. Engel, J. Chen, and Liu Chang. Development of polyimide flexible tactile sensor skin. *Journal of Micromechanics and Microengineering*, 13(3):359–66, 2003.
- [84] N. Futai, K. Matsumoto, and I. Shimoyama. A flexible micromachined planar spiral inductor for use as an artificial tactile mechanoreceptor. *Sensors and Actuators A: Physical*, A111(2-3):293–303, 2004.
- [85] D. Cotton, I. M. Graz, and S. P. Lacour. A multifunctional capacitive sensor for stretchable electronic skins. *Sensors Journal, IEEE*, 9(12):2008–2009, 2009.
- [86] Fan-Gang Tseng, Chih-Sheng Yang, and Li-Chern Pan. An elastomeric tactile sensor employing dielectric constant variation and applicable to orthodontia. In *17th International Conference on Micro Electro Mechanical Systems*, pages 564–7. IEEE, 2004.
- [87] J. Bartholomeyczik, J. Haefner, B. Lapatki, P. Ruther, T. Schelb, and O. Paul. Integrated six-degree-of-freedom sensing for orthodontic smart brackets. In *19th International Conference on Micro Electro Mechanical Systems (MEMS)*, pages 690–693. IEEE, 2006.
- [88] Mohsin I. Tiwana, Arridh Shashank, Stephen J. Redmond, and Nigel H. Lovell. Characterization of a capacitive tactile shear sensor for application in robotic and upper limb prostheses. *Sensors and Actuators A: Physical*, 165(2):164–172, 2011.
- [89] K. Sundara-Rajan, G. I. Rowe, A. J. Simon, G. K. Klute, W. R. Ledoux, and A. V. Mamishev. Shear sensor for lower limb prosthetic applications. In *Biomedical Science Engineering Conference (BSEC)*, page 4 pp. IEEE, 2009.
- [90] K. Sundara-Rajan, G. I. Rowe, A. Bestick, A. V. Mamishev, G. K. Klute, and W. R. Ledoux. Capacitive sensing of interfacial forces in prosthesis. In *International Workshop on Medical Measurements and Applications (MeMeA)*, page 4 pp. IEEE, 2010.
- [91] K. Sundara-Rajan, A. Bestick, G. I. Rowe, G. K. Klute, W. R. Ledoux, H. C. Wang, and A. V. Mamishev. An interfacial stress sensor for biomechanical applications. *Measurement Science & Technology*, 23(8):085701 (10 pp.), 2012.
- [92] Y. Hu, R. B. Katragadda, H. Tu, Q. Zheng, Y. Li, and Y. Xu. Bioinspired 3-d tactile sensor for minimally invasive surgery. *Journal of Microelectromechanical Systems*, 19(6):1400–08, 2010.

- [93] P. Puangmali, K. Althoefer, L. D. Seneviratne, D. Murphy, and P. Dasgupta. State-of-the-art in force and tactile sensing for minimally invasive surgery. *IEEE Sensors Journal*, 8(4):371–81, 2008.
- [94] M. E. H. Eltaib and J. R. Hewit. Tactile sensing technology for minimal access surgery - a review. *Mechatronics*, 13(10):1163–77, 2003.
- [95] Miao Lu, Jijun Xiong, and Tianhong Cui. A flexible tri-axis contact force sensor for tubular medical device applications. *Journal of Micromechanics and Microengineering*, 21(3), 2011.
- [96] P. Peng, A. S. Sezen, R. Rajamani, and A. G. Erdman. Novel mems stiffness sensor for in-vivo tissue characterization measurement. In *31st Annual International Conference of the IEEE Engineering in Medicine and Biology Society (EMBC)*, pages 6640–3. IEEE, 2009.
- [97] P. Peng and R. Rajamani. Handheld microtactile sensor for elasticity measurement. *Sensors Journal, IEEE*, 11(9):1935–1942, 2011.
- [98] Chang Liu. *Foundations of MEMS*. Pearson/Prentice Hall, Upper Saddle River, 2006.
- [99] M. Sohgewa, T. Mima, H. Onishi, T. Kanashima, M. Okuyama, K. Yamashita, M. Noda, M. Higuchi, and H. Noma. Tactile array sensor with inclined chromium/silicon piezoresistive cantilevers embedded in elastomer. In *International Solid-State Sensors, Actuators and Microsystems Conference (Transducers)*, pages 284–287. IEEE, 2009.
- [100] K. Noda, Y. Hashimoto, Y. Tanaka, and I. Shimoyama. Memes on robot applications. In *International Solid-State Sensors, Actuators and Microsystems Conference (Transducers)*, pages 2176–2181. IEEE, 2009.
- [101] Kunnyun Kim, Kang Ryeol Lee, Dae Sung Lee, Nam-Kyu Cho, Won Hyo Kim, Kwang-Bum Park, Hyo-Derk Park, Yong Kook Kim, Yon-Kyu Park, and Jong-Ho Kim. A silicon-based flexible tactile sensor for ubiquitous robot companion applications. *Journal of Physics. Conference Series*, 34(1):399–403, 2006.
- [102] B. J. Kane, M. R. Cutkosky, and G. T. A. Kovacs. A traction stress sensor array for use in high-resolution robotic tactile imaging. *Journal of microelectromechanical systems*, 9(4):425–34, 2000.
- [103] P. Ruther, J. Bartholomeyczik, A. Trautmann, M. Wandt, O. Paul, W. Dominicus, R. Roth, K. Seitz, and W. Strauss. Novel 3d piezoresistive silicon force sensor for

## Bibliography

---

- dimensional metrology of micro components. *IEEE Sensors*, pages 1006–1009, 2005.
- [104] Lucia Beccai, Stefano Roccella, Alberto Arena, Francesco Valvo, Pietro Valdastri, Arianna Menciassi, Maria Chiara Carrozza, and Paolo Dario. Design and fabrication of a hybrid silicon three-axial force sensor for biomechanical applications. *Sensors and Actuators A: Physical*, 120(2):370–382, 2005.
- [105] Kentaro Noda, Kazunori Hoshino, Kiyoshi Matsumoto, and Isao Shimoyama. A shear stress sensor for tactile sensing with the piezoresistive cantilever standing in elastic material. *Sensors and Actuators A: Physical*, 127(2):295–301, 2006.
- [106] M. S. Bartsch, W. Federle, R. J. Full, and T. W. Kenny. A multiaxis force sensor for the study of insect biomechanics. *Journal of microelectromechanical systems*, 16(3):709–718, 2007.
- [107] D. Benfield, E. Lou, and W. A. Moussa. Parametric evaluation of shear sensitivity in piezoresistive interfacial force sensors. *Journal of Micromechanics and Microengineering*, 21(4):10, 2011.
- [108] L. Beccai, S. Roccella, L. Ascari, P. Valdastri, A. Sieber, M. C. Carrozza, and P. Dario. Development and experimental analysis of a soft compliant tactile microsensor for anthropomorphic artificial hand. *IEEE/ASME Transactions on Mechatronics*, 13(2):158–168, 2008.
- [109] Chang-Sin Park, Jongsung Park, and Dong-Weon Lee. A piezoresistive tactile sensor based on carbon fibers and polymer substrates. *Microelectronic Engineering*, 86(4-6):1250–1253, 2009.
- [110] J. Engel, J. Chen, Z. F. Fan, and L. Chang. Polymer micromachined multimodal tactile sensors. *Sensors and Actuators A: Physical*, 117(1):50–61, 2005.
- [111] Woo-Chang Choi. Polymer micromachined flexible tactile sensor for three-axial loads detection. *Transactions on electrical and electronic materials*, 11(3):130–3, 2010.
- [112] H. J. Kwon, J. H. Kim, and W. C. Choi. Development of a flexible three-axial tactile sensor array for a robotic finger. *Microsystem Technologies-Micro-and Nanosystems-Information Storage and Processing Systems*, 17(12):1721–1726, 2011.
- [113] Yong-Lae Park, Carmel Majidi, Rebecca Kramer, Phillipe Bérard, Robert J Wood, and et al. Hyperelastic pressure sensing with a liquid-embedded elastomer. *Journal of Micromechanics and Microengineering*, 20(12):125029, 2010.



- 
- [114] W. S. Su, C. F. Hu, C. M. Lin, and W. L. Fang. Development of a 3d distributed carbon nanotubes on flexible polymer for normal and shear forces measurement. In *23rd International Conference on Micro Electro Mechanical Systems (MEMS)*, pages 615–618. IEEE, 2010.
- [115] Claudia Steinem. *Piezoelectric Sensors*. Springer, Berlin, 2007.
- [116] E. S. Kolesar and C. S. Dyson. Object imaging with a piezoelectric robotic tactile sensor. *Journal of microelectromechanical systems*, 4(2):87–96, 1995.
- [117] W. Y. Chang, T. H. Fang, C. I. Weng, and S. S. Yang. Flexible piezoelectric harvesting based on epitaxial growth of zno. *Applied Physics a-Materials Science & Processing*, 102(3):705–711, 2011.
- [118] R. S. Dahiya, G. Metta, and M. Valle. Piezoelectric polymer oxide semiconductor field effect transistor (posfet) devices for touch sensing. In *2nd International Workshop on Electron Devices and Semiconductor Technology*, pages 1–5, 2009.
- [119] C. Y. Li, P. M. Wu, S. Lee, A. Gorton, M. J. Schulz, and C. H. Ahn. Flexible dome and bump shape piezoelectric tactile sensors using pvdf-trfe copolymer. *Journal of microelectromechanical systems*, 17(2):334–341, 2008.
- [120] Koh Hosoda, Yasunori Tada, and Minoru Asada. Anthropomorphic robotic soft fingertip with randomly distributed receptors. *Robotics and Autonomous Systems*, 53(2):104–109, 2006.
- [121] Tai-Ran Hsu. *MEMS and microsystems design, manufacture and nanoscale engineering*. Wiley, Hoboken, N.J., 2nd edition, 2008.
- [122] Jin Wang, Hiroshi Sato, Chunye Xu, and Minoru Taya. Bioinspired design of tactile sensors based on flemion. *Journal of applied physics*, 105(8):083515, 2009.
- [123] M. Y. Cheng, C. M. Tsao, Y. T. Lai, and Y. J. Yang. A novel highly-twistable tactile sensing array using extendable spiral electrodes. In *22nd International Conference on Micro Electro Mechanical Systems (MEMS)*, pages 92–95. IEEE, 2009.
- [124] L. H. Chen, S. Jin, and T. H. Tiefel. Tactile shear sensing using anisotropically conductive polymer. *Applied Physics Letters*, 62(19):2440–2442, 1993.
- [125] S. L. Yu, D. R. Chang, L. C. Tsao, W. P. Shih, and P. Z. Chang. Porous nylon with electro-active dopants as flexible sensors and actuators. In *21st International Conference on Micro Electro Mechanical Systems (MEMS)*, pages 908–911. IEEE, 2008.

## Bibliography

---

- [126] B. Levey, P. Gieschke, M. Doelle, S. Spinner, A. Trautmann, P. Ruther, and O. Paul. Cmos-integrated silicon 3d force sensor system for micro component coordinate measurement machines. In *20th International Conference on Micro Electro Mechanical Systems*, Proceedings: IEEE Micro Electro Mechanical Systems, pages 486–489. IEEE, 2007.
- [127] I. Manunza, A. Sulis, and A. Bonfiglio. Pressure sensing by flexible, organic, field effect transistors. *Applied Physics Letters*, 89(14), 2006.
- [128] I. Manunza and A. Bonfiglio. Pressure sensing using a completely flexible organic transistor. *Biosensors & Bioelectronics*, 22(12):2775–2779, 2007.
- [129] T. Sekitani. A rubberlike stretchable active matrix using elastic conductors. *Science*, 321(5895):1468–72, 2008.
- [130] Ingrid Graz, Martin Kaltenbrunner, Christoph Keplinger, Reinhard Schwodiauer, Siegfried Bauer, Stephanie P. Lacour, and Sigurd Wagner. Flexible ferroelectret field-effect transistor for large-area sensor skins and microphones. *Applied Physics Letters*, 89(7):073501–3, 2006.
- [131] S. P. Lacour, C. Tsay, and S. Wagner. An elastically stretchable tft circuit. *IEEE electron device letters*, 25(12):792–794, 2004.
- [132] I. M. Graz and S. P. Lacour. Flexible pentacene organic thin film transistor circuits fabricated directly onto elastic silicone membranes. *Applied Physics Letters*, 95(24), 2009.
- [133] Ravinder S. Dahiya, Maurizio Valle, Giorgio Metta, and Leandro Lorenzelli. Posfet based tactile sensor arrays. In *14th International Conference on Electronics, Circuits and Systems*, pages 1075–1078. IEEE, 2007.
- [134] Ravinder S. Dahiya, Leandro Lorenzelli, Giorgio Metta, and Maurizio Valle. Posfet devices based tactile sensing arrays. In *International Symposium on Circuits and Systems*, IEEE International Symposium on Circuits and Systems, pages 893–896. IEEE, 2010.
- [135] I. Graz, M. Krause, S. Bauer-Gogonea, S. Bauer, S. P. Lacour, B. Ploss, M. Zirkl, B. Stadlober, and S. Wagner. Flexible active-matrix cells with selectively poled bifunctional polymer-ceramic nanocomposite for pressure and temperature sensing skin. *Journal of applied physics*, 106(3), 2009.
- [136] J. Zubia and J. Arrue. Plastic optical fibers: An introduction to their technological processes and applications. *Optical Fiber Technology*, 7(2):101–140, 2001.

- [137] J. S. Heo, J. Y. Kim, and J. J. Lee. Tactile sensors using the distributed optical fiber sensors. In S. C. Mukhopadhyay, G. S. Gupta, and R. Y. M. Huang, editors, *3rd International Conference on Sensing Technology*, pages 486–490. IEEE, 2008.
- [138] M. Rothmaier, M. P. Luong, and F. Clemens. Textile pressure sensor made of flexible plastic optical fibers. *Sensors*, 8(7):4318–4329, 2008.
- [139] Y. Kim, S. Park, S. K. Park, S. Yun, K. U. Kyung, and K. Sun. Transparent and flexible force sensor array based on optical waveguide. *Optics Express*, 20(13):14486–14493, 2012.
- [140] J. Missinne, E. Bosman, B. Van Hoe, G. Van Steenberge, S. Kalathimekkad, P. Van Daele, and J. Vanfleteren. Flexible shear sensor based on embedded optoelectronic components. *IEEE Photonics Technology Letters*, 23(12):771–773, 2011.
- [141] J. Streque, A. Talbi, P. Pernod, and V. Preobrazhensky. New magnetic microactuator design based on pdms elastomer and mems technologies for tactile display. *IEEE Transactions on Haptics*, 3(2):88–97, 2010.
- [142] Mohamed Benali-Khoudja, Moustapha Hafez, and Abderrahmane Kheddar. Vital: An electromagnetic integrated tactile display. *Displays*, 28(3):133–144, 2007.
- [143] P. A. Passeraub, P. A. Besse, S. Hediger, C. de Raad, and R. S. Popovic. High-resolution miniaturized inductive proximity sensor: characterization and application for step-motor control. *Sensors and Actuators A: Physical*, 68(1-3):257–262, 1998.
- [144] P. A. Passeraub, P. A. Besse, C. de Raad, O. Dezuari, F. Quinet, and R. S. Popovic. Metallic profile and coin imaging using an inductive proximity sensor microsystem. *Sensors and Actuators A: Physical*, 66(1-3):225–230, 1998.
- [145] T. J. Nelson, R. B. Vandover, S. Jin, S. Hackwood, and G. Beni. Shear-sensitive magnetorestrictive robotic tactile sensor. *IEEE Transactions on magnetics*, 22(5):394–396, 1986.
- [146] Menouer Saidani. *Miniaturized hybrid inductors and transformers, thesis no 3209*. Thèse sciences, epf lausanne, no 3209 (2005), faculté sciences et techniques de l'ingénieur sti, section de microtechnique (institut de microélectronique et microsystèmes) directeur: M gijis ; rapporteurs: J -ph ansermet et al, EPFL, 2005.

## Bibliography

---

- [147] P. A. Passeraub, G. Rey Mermet, P. A. Besse, H. Lorenz, and R. S. Popovic. Inductive proximity sensor with a flat coil and a new differential relaxation oscillator. *Sensors and Actuators A: Physical*, 60(1-3):122–126, 1997.
- [148] M. Woytasik, J. P. Grandchamp, E. Dufour-Gergam, E. Martincic, J. P. Gilles, S. Megherbi, V. Lavalley, and V. Mathet. Fabrication of planar and three-dimensional microcoils on flexible substrates. *Microsystem Technologies-Micro-and Nanosystems-Information Storage and Processing Systems*, 12(10-11):973–978, 2006.
- [149] M. Woytasik, J. P. Grandchamp, E. Dufour-Gergam, J. P. Gilles, S. Megherbi, E. Martincic, H. Mathias, and P. Crozat. Two- and three-dimensional microcoil fabrication process for three-axis magnetic sensors on flexible substrates. *Sensors and Actuators A: Physical*, 132(1):2–7, 2006.
- [150] Larry K. Baxter. *Capacitive sensors design and applications*. IEEE Press, New York, 1997.
- [151] Robert Puers. Capacitive sensors: When and how to use them. *Sensors and Actuators A: Physical*, 37-38:93–105, 1993.
- [152] Xuanhe Zhao and Zhigang Suo. Electrostriction in elastic dielectrics undergoing large deformation. *Journal of applied physics*, 104(12):123530–7, 2008.
- [153] R. A. Boie. Capacitive impedance readout tactile image sensor. In *International Conference on Robotics and Automation*, volume 1, pages 370–378. IEEE, 1984.
- [154] K. J. Chun and K. D. Wise. A high-performance silicon tactile imager based on a capacitive cell. In *First World Conference on Robotics Research, Robotics Research. The Next Five Years and Beyond.*, pages 84–494. Robotics Int. SME, 1984.
- [155] F. Zhu and J. W. Spronck. A capacitive tactile sensor for shear and normal force measurements. *Sensors and Actuators A: Physical*, 31(1-3):115–120, 1992.
- [156] Z. Chu, P. M. Sarro, and S. Middelhoek. Silicon three-axial tactile sensor. *Sensors and Actuators A: Physical*, 54(1-3):505–510, 1996.
- [157] T. A. Chase and C. L. Ren. A thin-film flexible capacitive tactile normal/shear force array sensor. In *21st Annual Conference on Industrial Electronics*, pages 1196–201. IEEE, 1995.
- [158] R. A. Brookhuis, T. S. J. Lammerink, R. J. Wiegerink, M. J. de Boer, and M. C. Elwenspoek. 3d force sensor for biomechanical applications. *Sensors and Actuators, A: Physical*, 182:28–33, 2012.

- [159] M. Makihata, S. Tanaka, M. Muroyama, S. Matsuzaki, H. Yamada, T. Nakayama, U. Yamaguchi, K. Mima, Y. Nonomura, M. Fujiyoshi, and M. Esashi. Integration and packaging technology of mems-on-cmos capacitive tactile sensor for robot application using thick bcb isolation layer and backside-grooved electrical connection. *Sensors and Actuators A: Physical*, 2012.
- [160] Hong-Ki Kim, Seung-Gun Lee, Ji-Eun Han, Tae-Rim Kim, Sung-Up Hwang, Ahn Seong Deok, In-Kyu You, Kyoung-Ik Cho, Tai-Kyong Song, and Kwang-Seok Yun. Transparent and flexible tactile sensor for multi touch screen application with force sensing. In *International Conference on Solid-State Sensors, Actuators and Microsystems (Transducers)*, pages 1146–9. IEEE, 2009.
- [161] Kim Baek-Chul, S. H. Shin, Y. Lee, J. D. Nam, H. R. Choi, H. P. Moon, and J. C. Koo. Multi-axis flexible force sensor for tactile display. In *IEEE Sensors Conference*, page 4 pp. IEEE, 2011.
- [162] William F. Hosford. *Mechanical behavior of materials*. Cambridge University Press, New York, 2005.
- [163] Ruben D. Ponce Wong, Jonathan D. Posner, and Veronica J. Santos. Flexible microfluidic normal force sensor skin for tactile feedback. *Sensors and Actuators a-Physical*, 179:62–69, 2012.
- [164] Y. Hasegawa, Shikida M., Ogura D., Suzuki Y., and Sato K. Fabrication of a wearable fabric tactile sensor produced by artificial hollow fiber. *Journal of Micromechanics and Microengineering*, 18(8):085014, 2008.
- [165] Hyung-Kew Lee, Jaehoon Chung, Chih-Hang Chang, and Euisik Yoon. Normal and shear force measurement using a flexible polymer tactile sensor with embedded multiple capacitors. *Journal of microelectromechanical systems*, 17(4):934–42, 2008.
- [166] Hyung-Kew Lee, Sun-Il Chang, and Euisik Yoon. A flexible polymer tactile sensor: fabrication and modular expandability for large area deployment. *Journal of microelectromechanical systems*, 15(6):1681–6, 2006.
- [167] Hyung-Kew Lee, Jaehoon Chung, Sun-Il Chang, and Euisik Yoon. Polymer tactile sensing array with a unit cell of multiple capacitors for three-axis contact force image construction. In *20th International Conference on Micro Electro Mechanical Systems (MEMS)*, pages 623–6. IEEE, 2007.
- [168] M. Y. Cheng, X-H Huang, C-W Ma, and Y-J Yang. A flexible capacitive tactile sensing array with floating electrodes. *Journal of Micromechanics and Microengineering*, 19(11):115001, 2009.

## Bibliography

---

- [169] Ming-Yuan Cheng, Chun-Liang Lin, Yu-Tse Lai, and Yao-Joe Yang. A polymer-based capacitive sensing array for normal and shear force measurement. *Sensors*, 10(11):10211–10225, 2010.
- [170] Rajesh Surapaneni, K. Park, M. A. Suster, D. J. Young, and C. H. Mastrangelo. A highly sensitive flexible pressure and shear sensor array for measurement of ground reactions in pedestrian navigation. In *International Conference on Solid-State Sensors, Actuators and Microsystems (Transducers)*, pages 906–9. IEEE, 2011.
- [171] Rajesh Surapaneni, Yan Xie, Kyungjin Park, and Carlos Mastrangelo. Micro-fabrication of flexible self-repairing ground reaction sensor with liquid metal electrodes. In *Euroensors Conference*, volume 25 of *Procedia Engineering*, pages 124–127, 2011.
- [172] G. Kita, Y. Suzuki, M. Shikida, and K. Sato. Development of fabric force sensor for detecting normal and lateral force by applying umbonal fiber. In *15th International Conference on Solid-State Sensors, Actuators and Microsystems (Transducers)*, pages 1746–1749. IEEE, 2009.
- [173] D. McHerron, E. Perfecto, and T. Redmond. Mcm-d polyimide applications at ibm. In *National Electronic Packaging and Production Conference NEPCON East '94*, pages 166–75, Stamford, CT, USA, 1994. Reed Exhibition Companies.
- [174] David J. Beebe and Denice D. Denton. Flexible polyimide-based package for silicon sensors. *Sensors and Actuators A: Physical*, 44(1):57–64, 1994.
- [175] J. A. Dobrzynska and M. A. M. Gijs. Flexible polyimide-based force sensor. *Sensors and Actuators A: Physical*, 173(1):127–135, 2012.
- [176] J. A. Dobrzynska and M. A. M. Gijs. Capacitive flexible force sensor. In B. Jakoby and M. J. Vellekoop, editors, *XXIV Euroensors Conference*, volume 5 of *Procedia Engineering*, pages 404–407, 2010.
- [177] Eric Brown, Nicholas Rodenberg, John Amend, Annan Mozeika, Erik Steltz, Mitchell R. Zakin, Hod Lipson, and Heinrich M. Jaeger. Universal robotic gripper based on the jamming of granular material. *Proceedings of the National Academy of Sciences*, 107(44):18809–14, 2010.
- [178] HDMicrosystems. Liquid polyimides and pbo precursors. <http://hdmicrosystems.com>, 2012.

- [179] Hsiharng Yang, Ching-Kong Chao, Che-Ping Lin, and Sheng-Chih Shen. Micro-ball lens array modeling and fabrication using thermal reflow in two polymer layers. *Journal of Micromechanics and Microengineering*, 14(2):277–82, 2004.
- [180] Shimul Chandra Saha, Håkon Sagberg, Erik Poppe, Geir Uri Jensen, Tor A. Fjeldly, and Trond Sæther. Tuning of resist slope with hard-baking parameters and release methods of extra hard photoresist for rf mems switches. *Sensors and Actuators A: Physical*, 143(2):452–461, 2008.
- [181] S. Metz, C. Trautmann, A. Bertsch, and P. Renaud. Flexible microchannels with integrated nanoporous membranes for filtration and separation of molecules and particles. In *15th International Conference on Micro Electro Mechanical Systems (MEMS)*, pages 81–84. IEEE, 2002.
- [182] T. A. Carlson and G. E. McGuire. Study of the x-ray photoelectron spectrum of tungsten-tungsten oxide as a function of thickness of the surface oxide layer. *Journal of Electron Spectroscopy and Related Phenomena*, 1(2):161–168, 1972.
- [183] B. R. Strohmeier. An esca method for determining the oxide thickness on aluminum alloys. *Surface and Interface Analysis*, 15:51–56, 1990.
- [184] M C Biesinger. Aluminum oxide/hydroxide thickness calculator using the strohmeier equation, surface science western. <http://sprocket.ssw.uwo.ca/xpsfiles/Aluminum%20Oxide-Hydroxide%20Thickness%20Calculator%20small%20version.xls>, 2008.
- [185] Y. Moser. Miniaturized flexible temperature sensor. *Journal of microelectromechanical systems*, 16(6):1349–54, 2007.
- [186] T. Sakurai and K. Tamaru. Simple formulas for two- and three-dimensional capacitances. *IEEE Transactions on electron devices*, ED-30(2):183–5, 1983.
- [187] E. Belloy, A. Sayah, and M. A. M. Gijs. Micromachining of glass inertial sensors. *Journal of Microelectromechanical Systems*, 11(1):85–90, 2002.
- [188] M. Kothari, J. G. Webster, W. J. Tompkins, J. J. Wertsch, and P. Bach-y Rita. Capacitive sensors for measuring the pressure between the foot and shoe. In *International Conference of the Engineering in Medicine and Biology Society*, pages 805–6. IEEE, 1988.
- [189] Yuan-Jen Chang, Kamran Mohseni, and Victor M. Bright. Fabrication of tapered su-8 structure and effect of sidewall angle for a variable focus microlens using ewod. *Sensors and Actuators A: Physical*, 136(2):546–553, 2007.

## Bibliography

---

- [190] J. A. Dobrzynska and M. A. M. Gijs. Polymer-based flexible capacitive sensor for three-axial force measurements. *Journal of Micromechanics and Microengineering*, 23(1):015009, 2013.
- [191] James Cameron. *The terminator*, 1984.
- [192] Irvin Kershner. *Star wars. episode v: The empire strikes back*, 1980.
- [193] M. G. Benedetti, F. Catani, A. Leardini, E. Pignotti, and S. Giannini. Data management in gait analysis for clinical applications. *Clinical Biomechanics*, 13(3):204–215, 1998.
- [194] Harold B. Kitaoka, Xavier M. Crevoisier, Kimberly Harbst, Diana Hansen, Brian Kotajarvi, and Kenton Kaufman. The effect of custom-made braces for the ankle and hindfoot on ankle and foot kinematics and ground reaction forces. *Archives of Physical Medicine and Rehabilitation*, 87(1):130–135, 2006.
- [195] C. Beyaert, F. Sirveaux, J. Paysant, D. Molé, and J. M. André. The effect of tibio-talar arthrodesis on foot kinematics and ground reaction force progression during walking. *Gait & Posture*, 20(1):84–91, 2004.
- [196] D. Szmigiel, C. Hibert, Arnaud Bertsch, E. Pamula, K. Domanski, P. Grabiec, P. Prokaryn, A. Scislowska-Czarnecka, and B. Plytycz. Fluorine based plasma treatment of biocompatible silicone elastomer. effect of temperature on etch rate and surface properties. *Plasma Processes and Polymers*, 5(3):246–255, 2008.
- [197] S. Metz, A. Bertsch, and P. Renaud. Partial release and detachment of microfabricated metal and polymer structures by anodic metal dissolution. *Journal of microelectromechanical systems*, 14(2):383–391, 2005.
- [198] S. Wagner, S. P. Lacour, J. Jones, P. I. Hsu, J. C. Sturm, T. Li, and Z. Suo. Electronic skin: architecture and components. *Physica E: Low-dimensional Systems and Nanostructures*, 25(2):326–334, 2004.
- [199] Theodore A. Harder, Tze-Jung Yao, Qing He, Chi-Yuan Shih, and Yu-Chong Tai. Residual stress in thin-film parylene-c. In *Micro Electro Mechanical Systems Conference (MEMS)*, pages 435–438. IEEE, 2002.
- [200] S. Dabral, J. Van Etten, X. Zhang, C. Apblett, G. Yang, P. Ficalora, and J. McDonald. Stress in thermally annealed parylene films. *Journal of Electronic Materials*, 21(10):989–994, 1992.
- [201] Manas Chanda and Salil K. Roy. *Plastics fundamentals, properties, and testing*. CRC Press, Boca Raton, FL, 2009.



- [202] D. Fuard, T. Tzvetkova-Chevolleau, S. Decossas, P. Tracqui, and P. Schiavone. Optimization of poly-di-methyl-siloxane (pdms) substrates for studying cellular adhesion and motility. *Microelectronic Engineering*, 85(5–6):1289–1293, 2008.
- [203] J. A. Dobrzynska, P. Joris, S. Jiguet, P. Renaud, and M. A. M. Gijs. Polyimide foam-like microstructures: technology and mechanical properties. *Journal of Micromechanics and Microengineering*, 21(10):105016, 2011.
- [204] Food Nations and Agriculture Organization of the United. Sponges: world production and markets. <http://www.fao.org/docrep/field/003/AC286E/AC286E01.htm>, 2012.
- [205] Nora Jacobson. *Cleavage technology, controversy, and the ironies of the man-made breast*. Rutgers, New Brunswick, NJ, 2000.
- [206] J. L. Hedrick, K. Carter, J. Labadie, R. Miller, W. Volksen, C. Hawker, D. Yoon, T. Russell, J. McGrath, and R. Briber. Nanoporous polyimides. *Progress in Polyimide Chemistry II*, 141:1–43, 1999.
- [207] C. Metzger, E. Fleisch, J. Meyer, M. Dansachmuller, I. Graz, M. Kaltenbrunner, C. Keplinger, R. Schwodiauer, and S. Bauer. Flexible-foam-based capacitive sensor arrays for object detection at low cost. *Applied Physics Letters*, 92(1):3, 2008.
- [208] S. Weinstein. Intensive and extensive aspects of tactile sensitivity as a function of body part, sex, and laterality, in: The skin senses. In Daniel Ralph Kenshalo, editor, *First International Symposium on the skin senses*, page 636 S., Springfield, Ill., 1968. Thomas.
- [209] Malay K. Ghosh. *Polyimides fundamentals and applications*. Dekker, New York Basel, 1996.
- [210] S. T. Lee and Natarajan S. Ramesh. *Polymeric foams mechanisms and materials*. CRC Press, Boca Raton, 2004.
- [211] J.G. Hilborn, C.J.G. Plummer, Y. Leterrier, and J.L. Hedrick. Synthesis and dynamics of nanoporous polymers. *Materials Research Society Symposium Proceedings*, 371:481–486, 1995.
- [212] C. Resewski and W. Buchgraber. Properties of new polyimide foams and polyimide foam filled honeycomb composites. *Materialwissenschaft und Werkstofftechnik*, 34(4):365–369, 2003.

## Bibliography

---

- [213] Y. Hirai, K. Sugano, T. Tsuchiya, and O. Tabata. Embedded microstructure fabrication using developer-permeability of semi-cross-linked negative resist. *Journal of microelectromechanical systems*, 19(5):1058–69, 2010.
- [214] Y. Hirai, Y. Nakai, K. Sugano, T. Tsuchiya, and O. Tabata. Embedded double-layered microchannel fabrication for microfluidic devices using developer permeability of negative thick-film resists. In *XXIV Eurosensors Conference*, volume 5 of *Procedia Engineering*, pages 854–857. Elsevier, 2010.
- [215] Stefan Metz, Raphael Holzer, and Philippe Renaud. Polyimide-based microfluidic devices. *Lab on a Chip*, 1(1):29–34, 2001.
- [216] A. T. Ciftlik and M. A. M. Gijs. A low-temperature parylene-to-silicon dioxide bonding technique for high-pressure microfluidics. *Journal of Micromechanics and Microengineering*, 21(3):035011, 2011.
- [217] D. Bhusari, H. A. Reed, M. Wedlake, A. M. Padovani, S. A. B. Allen, and P. A. Kohl. Fabrication of air-channel structures for microfluidic, microelectromechanical, and microelectronic applications. *Journal of Microelectromechanical Systems*, 10(3):400–408, 2001.
- [218] H. A. Reed, C. E. White, V. Rao, S. A. B. Allen, C. L. Henderson, and P. A. Kohl. Fabrication of microchannels using polycarbonates as sacrificial materials. *Journal of Micromechanics and Microengineering*, 11(6):733–737, 2001.
- [219] Joseph Paul Jayachandran, Hollie A. Reed, Hongshi Zhen, Larry F. Rhodes, Clifford L. Henderson, Sue Ann Bidstrup, and Paul A. Kohl. Air-channel fabrication for microelectromechanical systems via sacrificial photosensitive polycarbonates. *Journal of microelectromechanical systems*, 12(2):147–159, 2003.
- [220] Xiaoqun Wu, Hollie A. Reed, Yong Wang, Larry F. Rhodes, Ed Elce, R. Ravikiran, Robert A. Shick, Clifford L. Henderson, Sue Ann Bidstrup Allen, and Paul A. Kohl. Fabrication of microchannels using polynorbornene photosensitive sacrificial materials. *Journal of The Electrochemical Society*, 150(9):205–213, 2003.
- [221] Paul Jayachandran Joseph, Hollie A. Kelleher, Sue Ann Bidstrup Allen, and Paul A. Kohl. Improved fabrication of micro air-channels by incorporation of a structural barrier. *Journal of Micromechanics and Microengineering*, 15(1):35, 2005.
- [222] P. Monajemi, P. J. Joseph, P. A. Kohl, and F. Ayazi. Characterization of a polymer-based mems packaging technique. In *11th International Symposium on Advanced Packaging Materials: Processes, Properties and Interface*, pages 139–144, 2006.

- 
- [223] S. Park, S. A. B. Allen, and P. A. Kohl. Air-gaps for high-performance on-chip interconnect part i: Improvement in thermally decomposable template. *Journal of Electronic Materials*, 37(10):1524–1533, 2008.
- [224] Seongho Park, S. Allen, and P. Kohl. Air-gaps for high-performance on-chip interconnect part ii: modeling, fabrication, and characterization. *Journal of Electronic Materials*, 37(10):1534–46, 2008.
- [225] Nathan Fritz, Rajarshi Saha, Sue Allen, and Paul Kohl. Photodefinable epoxy-cyclohexyl polyhedral oligomeric silsesquioxane. *Journal of Electronic Materials*, 39(2):149–156, 2010.
- [226] S. Metz, S. Jiguet, A. Bertsch, and P. Renaud. Polyimide and su-8 microfluidic devices manufactured by heat-depolymerizable sacrificial material technique. *Lab on a Chip*, 4(2):114–20, 2004.
- [227] K. Walsh, J. Norville, and Tai Yu-Chong. Photoresist as a sacrificial layer by dissolution in acetone. In *14th International Conference on Micro Electro Mechanical Systems*, pages 114–17. IEEE, 2001.
- [228] Suh Hyuk-Jeen, P. Bharathi, D. J. Beebe, and J. S. Moore. Dendritic material as a dry-release sacrificial layer. *Journal of Microelectromechanical Systems*, 9(2):198–205, 2000.
- [229] C. K. Harnett, G. W. Coates, and H. G. Craighead. Heat-depolymerizable polycarbonates as electron beam patternable sacrificial layers for nanofluidics. In *45th international conference on electron, ion, and photon beam technology and nanofabrication*, volume 19, pages 2842–2845. AVS, 2001.
- [230] James A. Cella. Degradation and stability of polyimides. *Polymer Degradation and Stability*, 36(2):99–110, 1992.
- [231] Hongwen Yan, W. Roger Cannon, and Daniel J. Shanefield. Thermal decomposition behaviour of poly(propylene carbonate). *Ceramics International*, 24(6):433–439, 1998.
- [232] Oscar Vazquez-Mena, Katrin Sidler, Veronica Savu, Chan Woo Park, Luis Guillermo Villanueva, and Juergen Brugger. Reliable and improved nanoscale stencil lithography by membrane stabilization, blurring, and clogging corrections. *IEEE Transactions on Nanotechnology*, 10(2):352–357, 2011.
- [233] Stanley Wolf and Richard N. Tauber. *Process technology*. Lattice Press, 1986.

## Bibliography

---

- [234] Warren C. Young and Richard G. Budynas. *Roark's formulas for stress and strain*. McGraw-Hill, New York, 7th edition, 2002.
- [235] Ian Macmillan Ward and John Sweeney. *An introduction to the mechanical properties of solid polymers*. Wiley, Chichester, 2nd edition, 2004.
- [236] Y. Leterrier, J.A.E. Manson, J.G. Hilborn, C.J.G. Plummer, and J.L. Hedrick. Small strain behavior of polyimide nanofoams. *Materials Research Society Symposium Proceedings*, 371:487–493, 1995.
- [237] Masato Watanabe, Atsushi Sakuma, Mitsuo Kawashima, Kenichiro Abe, and Shigeru Nagaki. Strain-rate dependency of plateau region of low-density porous materials in compression process and its constitutive representation. *Journal of Solid Mechanics and Materials Engineering*, 4(8):1289–1295, 2010.
- [238] G. Dehm, H. P. Worgotter, S. Cazottes, J. M. Purswani, D. Gall, C. Mitterer, and D. Kiener. Can micro-compression testing provide stress-strain data for thin films? a comparative study using cu, vn, tin and w coatings. *Thin Solid Films*, 518(5):1517–1521, 2009.

## C Publications

### Journal articles

---

*Polyimide foam-like microstructures: technology and mechanical properties* (2011) **Dobrzynska J A**, Joris P, Jiguet S, Renaud P, and Gijs M A M, Journal of Micromechanics and Microengineering **21**(10)105016, DOI: 10.1088/0960-1317/21/10/105016

*Flexible polyimide-based force sensor* (2012) **Dobrzynska J A** and Gijs M A M, Sensors and Actuators A: Physical **173**(1)127-135, DOI: 10.1016/j.sna.2011.11.006

*Polymer-based flexible capacitive sensor for three-axial force measurements* (2013) **Dobrzynska J A** and Gijs M A M, Journal of Micromechanics and Microengineering **23**(1)015009, DOI: 10.1088/0960-1317/23/1/015009

### Conference proceedings

---

*Capacitive flexible force sensor* (2010) **Dobrzynska J A** and Gijs M A M, Procedia Engineering **5**404-407, DOI: 10.1016/j.proeng.2010.09.132

### Conference and workshop contributions

---

*Capacitive Flexible Force Sensor* (2010) **Dobrzynska J A** and Gijs M A M, Eurosensors XXIV Conference, 5-8 September 2010, Linz, Austria, *oral presentation*

*Flexible 3D force sensor for gait analysis* (2010) **Dobrzynska J A** and Gijs M A M, Nano and Microsystems International Autumn School (NAMIS), 17-23 October 2010, Tokyo, Japan, *poster + Best Poster Award: Silver Prize*

*Towards Artificial Skin* (2012) **Dobrzynska J A** and Gijs M A M, MicroNanoFabrication Annual Review Meeting, 8 May 2012, Lausanne, Switzerland, *invited lecture*



# Jagoda Anna DOBRZYNSKA

Av. du Tir-Fédéral 36  
1024 Ecublens  
Switzerland

+41 76 711 84 66  
jagoda.dobrzynska@gmail.com  
nationality : Polish  
born 06.02.1981  
married, 1 child



## Education

---

**PhD** Microsystems and Microelectronics, *EPFL*, Switzerland, 2009 – 2012.

**MSc Eng** Automation and Industrial Robotics, with honors, *Warsaw University of Technology*, Poland, 2001–2006, *Chalmers University of Technology*, Sweden (*Erasmus exchange*).

## Work experience

---

**2009 – 2012: Doctoral assistant**, Microsystems Laboratory 2, EPFL, Switzerland

- Design, manufacturing, and characterization of a flexible artificial skin sensor.
- Process development and introduction of novel materials in a MEMS manufacturing site.
- Process optimization for polymers as flexible substrates in MEMS.

**2007 – 2009: Researcher**, University Politehnica of Bucharest, Romania

- Development of semiconductor electronics simulation software (*Marie Curie* fellowship, European Commission).

**2006 – 2007: Project Engineer**, Sener Ingeniería y Sistemas SA, Spain

- Design of electrical installations in railways, airports, buildings, shipyards, power plants.
- Implementation of 6x \$2 million power transformers in 5 km of *Algiers Metro* (Algeria).
- Planning 50 km power supply cabling in a ship dock of *José de San Martín* (Argentina) power plant, within \$1 billion project.
- Design of installation for uninterruptible power supply for the *Málaga Airport* (Spain), providing the capacity of 9'000 passengers per hour in the newly constructed Terminal 3.
- Feasibility study of new seaport (Guinea-Bissau), offering safe workplace to 500 African workmen.

## Language skills

---

<b>Polish</b>	native	
<b>English</b>	excellent	<i>First Certificate in English</i> (B2), <i>TOEFL</i> (C1)
<b>German</b>	fluent	<i>Zentrale Mittelstufenprüfung</i> (C1), <i>Deutsches Sprachdiplom</i> (B2)
<b>Spanish</b>	proficient	<i>Diploma de Español como Lengua Extranjera</i> (B2)
<b>French</b>	proficient	EPFL Language Center course (B2)

## Other activities

---

Climbing, coaching other climbers. Worked 4 years as a rock climbing instructor.

**Awards:** 1<sup>st</sup> champion, *Polish National Academic Sports Climbing Championships* 2004.